Mineralogical, fluid inclusion, and stable isotope constraints on the origin of footwall-style "high sulfide" and "low sulfide" Cu-Ni-PGE mineralization at the Coleman Mine, Sudbury Igneous Complex (SIC), Sudbury, Ontario, Canada

By

Matthew Angus MacMillan

A thesis submitted to Saint Mary's University, Halifax, Nova Scotia in partial fulfillment of the requirements for the degree of Master of Science in Applied Science

April 29th, 2014

© Matthew Angus MacMillan, 2014

Approved: Dr. Jacob Hanley
              Supervisor
              Department of Geology
              Saint Mary's University

Approved: Dr. Doreen Ames
              Supervisory Committee
              Geological Survey of Canada

Approved: Dr. Brendan Murphy
              Supervisory Committee
              Department of Earth Sciences
              St. Francis Xavier University

Approved: Dr. Jason Clyburne
              Supervisory Committee
              Department of Chemistry
              Saint Mary's University

Approved: Dr. David Lentz
              External Examiner
              Department of Earth Sciences
              University of New Brunswick

Approved: Dr. Diane Crocker
              Faculty of Graduate Studies Representative
              Saint Mary's University

Abstract

Mineralogical, fluid inclusion, and stable isotope constraints on the origin of footwall-style "high sulfide" and "low sulfide" Cu-Ni-PGE mineralization at the Coleman Mine, Sudbury Igneous Complex (SIC), Sudbury, Ontario, Canada

By: Matthew Angus MacMillan

The Sudbury Igneous Complex, Ontario, Canada, is associated with polymetallic ore bodies that have achieved world-class status due to their high concentrations of nickel, copper, and platinum group elements. Relatively small-volume footwall deposits along the North and East ranges represent <10% of the historical metal resource at Sudbury but have garnered progressive exploration interest in recent years due to their marked enrichments in copper and precious metals. Within the last decade footwall systems have been subdivided into "high sulfide" and "low sulfide" members (sulfide content, alteration mineralogy, bulk rock characteristics) and the relationship between them can be oversimplified in the literature. The Coleman Mine (Onaping-Levack embayment, North Range) contains both high sulfide and low sulfide mineralization and mineralogical, bulk rock, fluid inclusion, and stable isotope results on rocks sampled here suggest that these two mineralization styles constitute independent geochemical systems that deposited Cu-Ni-PGE mineralization after evolving in opposite redox directions.

April 29th, 2014

Acknowledgments

Table of Contents

List of Figures

List of Tables

Chapter 1: Introduction

1.0 Structure of thesis

This thesis consists of four chapters. Chapter 1 contains a brief outline of the thesis structure and highlights its main objectives. Chapter 2 provides an in-depth mineralogical comparison between "high sulfide" (sharp-walled vein) and "low sulfide" (high-PGE) footwall Cu-Ni-PGE mineralization associated with the Sudbury Igneous Complex (SIC) in the 153 and 170 ore bodies at Vale's Coleman Mine. This chapter represents a stand-alone manuscript for submission to *Mineralium Deposita*. Chapter 3 focuses on a unique hydrothermal-garnet bearing assemblage associated with low sulfide mineralization in the Coleman 153 ore body to constrain the fluid conditions associated with this high-PGE style of footwall mineralization at Sudbury and also represents a stand-alone manuscript for submission to *Mineralium Deposita*. Chapter 4 suggests future studies that would support or refute conclusions made in this thesis.

1.1 Primary objectives of thesis

The primary objectives were set out at the onset of research in January, 2012. Focus would be on providing a comprehensive characterization (a predictive mineralogical model) and comparison of "high sulfide" (sharp-walled vein) and "low sulfide" (high-PGE) footwall Cu-Ni-PGE mineralization (and the relationship of these mineralization styles to associated wallrock alteration) in the Coleman 153 and 170 ore bodies through examining drill core and hand samples. Included in this

characterization would be identifying mineralogical controls (abundances, associations) and spatial distribution of the precious metals (Au, Ag, platinum group elements); as well as identifying key paragenetic relationships between sulfides, precious metal minerals, and alteration phases. The conclusions from this thesis would address whether any genetic relationship exists between the two mineralization styles and how these conclusions may be helpful in mine-scale exploration.

1.2 Secondary objectives of thesis

Underground sample collection in March, 2012 resulted in the sampling of hydrothermal garnet-bearing "low sulfide" assemblages. This is the first report of garnet in coeval gangue assemblages surrounding low sulfide footwall mineralization at Sudbury. Since garnet is such a robust mineral that records the geochemical evolution of geological systems through its growth zoning patterns, an ideal opportunity arose to quantitatively characterize many of the conditions associated with the formation of low sulfide mineralization.

1.3 List of abbreviations

The following table summarizes abbreviations that are commonly used in this thesis (following page):

Table 1.1: List of abbreviations used throughout thesis (majority of mineral abbreviations taken from Kretz, 1983)

Abbreviation	Meaning	Formula	Abbreviation	Meaning	Formula
SIC	Sudbury Igneous Complex		Gn	Galena	PbS
MSS	Monosulfide solid solution		Cst	Cassiterite	SnO_2
ISS	Intermediate solid solution		Aca	Acanthite	Ag_2S
BMS	Base metal sulfide		Fr	Froodite	$PdBi_2$
PGE	Platinum group element		El	Electrum	(Au,Ag)
PGM	Platinum group mineral		Geff	Geffroyite	$(Cu,Fe,Ag)_9(Se,S)_8$
PMM	Precious metal mineral		Ag	Native silver	Ag
REE	Rare earth element		Kot	Kotulskite	$Pd(Te,Bi)$
SIMS	Secondary ion mass spectrometry		Meren	Merenskyite	$(Pd,Pt)(Te,Bi)_2$
LA-ICPMS	Laser ablation - inductively coupled		Spy	Sperrylite	$PtAs_2$
	plasma mass spectrometry		Pao	Paolovite	Pd_2Sn
SEM-EDS	Scanning electron microscope - energy		Naum	Naumannite	Ag_2Se
	dispersive X-ray spectroscopy		Crn	Corundum	Al_2O_3
EMP	Electron microprobe		Prk	Parkerite	$Ni_3Bi_2S_2$
BSE	Backscattered electron		Cgy	Chlorargyrite	$AgCl$
HS	High sulfide		Cott	Cotunnite	$PbCl_2$
LS	Low sulfide		Nigg	Niggliite	$PtSn$
Eu*	Europium anomaly		Brt	Barite	$BaSO_4$
FIA	Fluid inclusion assemblage		Kur	Kurilite	$(Ag,Au)_2(Te,Se,S)$
T_h	Temperature of homogenization		Bis	Bismite	Bi_2O_3
T_m^{ice}	Temperature of last ice melting		Prt	Paratellurite	TeO_2
T_e^{ice}	Temperature of first ice melting		Witt	Wittichenite	Cu_3BiS_3
L	Liquid		Aik	Aikinite	$PbCuBiS_3$
V	Vapor		Tsu	Tsumoite	$BiTe$
S_1	Daughter mineral 1		Insiz	Insizwaite	$Pt(Bi,Sb)_2$
S_2	Daughter mineral 2		Sob	Sobolevskite	$PdBi$
wt% eq. NaCl	weight percent equivalent NaCl		Cre	Crerarite	$Pt_{2-x}(Bi,Pb)_{11}(S,Se)_{11}$
wt%	weight percent		Qtz	Quartz	SiO_2
at%	atomic percent		Cal	Calcite	$CaCO_3$
vol%	volume percent		Ep	Epidote	$Ca_2Al_2(Al,Fe)OOH[Si_2O_7][SiO_4]$
ρ	Density		Grt	Chlorite	$(Mg,Fe,Al)_3(Si,Al)_4O_{10}(OH)_2(Mg,Fe,Al)_3(OH)_6$
P	Pressure		Chl	Actinolite	$Ca_2(Mg,Fe)_5Si_8O_{22}(OH)_2$
T	Temperature		Act	Rutile	TiO_2
UN	Unnamed		Rut	Plagioclase	$NaAlSi_3O_8-CaAl_2Si_2O_8$
Sil	Silicates		Pl	K-feldspar	$KAlSi_3O_8$
Ccp	Chalcopyrite	$CuFeS_2$	Kfs	Biotite	$K(Fe,Mg)_3AlSi_3O_{10}(OH)_2$
Mil	Millerite	NiS	Bt	Stilpnomelane	$[(K,Ca,Na)(Fe,Mg,Al)_8(Si,Al)_{12}(O,OH)_{36}*nH_2O]$
Bn	Bornite	Cu_5FeS_4	Stp	Titanite	$CaTiSiO_5$
Pn	Pentlandite	$(Fe,Ni)_9S_8$	Ttn	Hornblende	$Ca_2(Mg,Fe,Al)_5(Al,Si)_8O_{22}(OH)_2$
Mt	Magnetite	Fe_3O_4	Hbl	Augite	$(Ca,Na)(Mg,Fe,Al,Ti)(Si,Al)_2O_6$
Sph	Sphalerite	ZnS	Aug	Apatite	$Ca_5(PO_4)_3(OH,F,Cl)$
Po	Pyrrhotite	$Fe_{1-x}S$	Ap	Garnet	$X_3Y_2(SiO_4)_3$
Cub	Cubanite	$CuFe_2S_3$	Adr	Andradite	$Ca_3Fe_2(SiO_4)_3$
Py	Pyrite	FeS_2	Grs	Grossular	$Ca_3Al_2(SiO_4)_3$
Hess	Hessite	Ag_2Te	Sps	Spessartine	$Mn_3Al_2(SiO_4)_3$
Mon	Moncheite	$(Pt,Pd)(Te,Bi)_2$	Alm	Almandine	$Fe_3Al_2(SiO_4)_3$
Mich	Michenerite	$(Pd,Pt)BiTe$	Prp	Pyrope	$Mg_3Al_2(SiO_4)_3$

Chapter 2: Mineralogical comparison between "high sulfide" and "low sulfide" styles of Cu-Ni-PGE mineralization within the footwall to the Sudbury Igneous Complex (SIC) in the Coleman 153 & 170 ore bodies, Coleman Mine, Sudbury, Canada

Matthew MacMillan*[1], Jacob Hanley[1], Doreen Ames[2], Simon Jackson[2], Zhaoping Yang[2]
[1]*Department of Geology, Saint Mary's University, Halifax, NS, Canada*
[2] *Geological Survey of Canada, Ottawa, ON, Canada*
*corresponding author e-mail address: macmillanmatt41@gmail.com

Abstract

Footwall-hosted occurrences of "high sulfide" (sharp-walled vein) and "low sulfide" (PGE-rich) Cu-Ni-PGE mineralization along the North Range of the Sudbury Igneous Complex (SIC) are commonly (but not exclusively) spatially associated with one another. In the 153 and 170 ore bodies at the Coleman Mine, sharp-walled veins contain >90% total sulfide minerals consisting of chalcopyrite, with lesser and variable Cu-, Ni-, and Fe- sulfides and oxides. These veins can be further divided into *Ni-rich* (chalcopyrite+pentlandite+millerite+magnetite+sphalerite±pyrrhotite), *Fe-rich* (chalcopyrite+cubanite+pyrite+magnetite+sphalerite+pyrrhotite±pentlandite), and *bornite-bearing* (bornite+chalcopyrite+millerite) subgroups on the basis of their respective mineralogies. Bornite-bearing high sulfide mineralization constitutes the terminations of sharp-walled vein systems. High precious metal tenors intrinsic to

the veins are controlled by the presence of composite grains of moncheite (Pt,Pd)(Te,Bi)$_2$ and hessite Ag$_2$Te, but many additional precious metal minerals are present within different sections of the mine and the PGM exhibit considerable solid solution between Pt-Pd and Te-Bi. Mineralogically- and chemically-different low sulfide high-PGE occurrences are also present in the Coleman 153 and 170 environments; and consist of blebs, disseminations, and stringers containing <5% total sulfide minerals (bornite, chalcopyrite, and millerite). Low sulfide samples exhibit PGE/S ratios that can be up to an order of magnitude higher than those in sharp-walled veins and the low sulfide samples can be further divided into 3 subgroups on the basis of their associated alteration assemblages: (1) *calcite-free* (quartz, epidote, chlorite, actinolite, titanite, apatite), (2) *calcite-bearing* (quartz, epidote, calcite, chlorite, titanite, Na-Cl silicate), (3) *garnet-bearing* (quartz, epidote, calcite, garnet, actinolite, calcic amphibole). Precious metal minerals exhibiting no solid solution (i.e. between Pt-Pd, Te-Bi, etc.) account for the high precious metal tenors of low sulfide mineralization.

Mass balance calculations were completed for 7 elements (Ni, Pb, Pt, Pd, Ag, Au, Sn) from high sulfide samples and the results provide the dominant mineral residence sites for each respective element: Ni (pentlandite, millerite), Pb (galena, chalcopyrite, millerite, pentlandite, bornite), Pt (moncheite, michenerite, merenskyite, sperrylite, nigglite), Pd (kotulskite, froodite, paolovite, merenskyite, michenerite, moncheite, pentlandite), Ag (hessite, native silver, electrum, geffroyite, bornite, pentlandite, chalcopyrite), Au (electrum, chalcopyrite, pentlandite, millerite,

bornite, magnetite), and Sn (paolovite, cassiterite, niggliite, chalcopyrite, pentlandite, millerite, magnetite, bornite). Bornite in high sulfide samples at vein extremities is notably rich in Ag (1120 ppm). Mass balances for the same 7 elements in low sulfide samples are as follows: Ni (millerite, parkerite, chalcopyrite), Pb (galena), Pt (moncheite, sperrylite, insizwaite, maslovite, crerarite, unnamed $(Pd,Pt)(Bi,Te)_2$ mineral, millerite, chalcopyrite), Pd (kotulskite, froodite, michenerite, unnamed $(Pd,Pt)(Bi,Te)_2$ mineral, moncheite, chalcopyrite, millerite, bornite), Ag (hessite, native silver, electrum, bornite, chalcopyrite), Au (electrum, chalcopyrite, bornite, millerite), and Sn (chalcopyrite, bornite, millerite). Consistent with previous work on footwall ores along the North Range, the PGE (Pt, Pd) in both mineralization styles are indubitably shown to be controlled by discrete PGM with small to negligible contributions from solid solution in base metal sulfides.

Alteration mineralogy in low sulfide mineralization affects bulk rock precious metal grades. Calcite-bearing alteration contains the highest Pt grades (17.0 g/t), followed by calcite-free alteration (6.67 g/t); with garnet-bearing alteration containing the lowest bulk rock Pt (0.01 g/t). Bulk rock Pd grades exhibit the same relative distribution (calcite-bearing alteration 4.66 g/t, calcite-free alteration 2.40 g/t, garnet-bearing alteration 0.22 g/t). Gold displays the opposite pattern to that of Pt and Pd. Garnet-bearing alteration grades the highest Au (18.7 g/t); whereas calcite-free alteration and calcite-bearing alteration exhibit strikingly lower Au grades of 0.94 g/t and 2.03 g/t, respectively.

An additional suite of mass balance calculations completed from samples taken at 1-meter intervals along 10-meters of a sharp-walled vein in the 170 ore body address stope-scale ore metal variability. Nickel budgets are limited to pentlandite and millerite along the entire 10 meters with the exception of one pentlandite/millerite-poor sample where chalcopyrite contributes significant Ni. Lead is entirely covered by galena in every sample taken along the vein. Platinum and Pd are both accounted for nearly entirely by the PGM moncheite and michenerite in every sample. Most of the Ag is contained in hessite and native silver whereas Au occurs dissolved in chalcopyrite unless any electrum is present. Tin is distributed between cassiterite, chalcopyrite, and sometimes magnetite. These results suggest that, at the scale of an individual stope, there is no significant lateral variation in the main carriers of Ni, Pb, Pt, Pd, Ag, and Sn. Variation in Au-carriers may represent the "nugget effect" of electrum in the veins.

High sulfide sharp-walled veins in the Coleman environment constitute the residual sulfide melt that separated from earlier-forming monosulfide solid solution (MSS) assemblages at the base of the SIC and descended into meteorite impact-induced openings in the footwall. This residual melt began stabilizing PGE-arsenides, PGE-stannides, and magnetite at high temperatures (>1000°C) followed by the crystallization of intermediate solid solution (ISS) as the temperature dropped below 1000°C (later exsolution of ISS below 650°C would produce the dominant vein phases chalcopyrite, pentlandite, millerite, and cubanite). Contemporaneous to or immediately following crystallization of ISS at 950-800°C,

an immiscible Pt-Pd-Ag-Bi-Te melt separated from the Cu-rich residue and began forming composite grains of moncheite and hessite. Other precious metal minerals later exsolved directly from ISS or crystallized from immiscible semimetal melt in areas where Pt, Pd, Ag, Bi, and Te availabilities were variable in the veins. As the Cu-rich residue evolved and moved away from the SIC contact, it progressively oxidized and began forming selenides (naumannite, geffroyite, clausthalite). Oxidation caused galena to incorporate substantial Se (replacing S) because the bulk metal/S ratio increased (resulting in less S^{2-} availability for metal cations) and would also cause Cu/Fe ratios to become high enough (because of the preferential conversion of Fe-S compounds into Fe-O compounds and the resistance of Cu-S compounds to being converted into oxide components) that the melt could fractionate past the ISS stability field and solidify at a thermal minimum (i.e. the most Cu-rich compositions in the Cu-Fe-S system have the lowest liquidus and solidus temperatures for that system) where bornite and millerite could crystallize together in equilibrium with carbonate – representing vein terminations. Low temperature exsolution of Cl-rich fluid from the veins resulted in the precipitation of secondary metal chlorides (cotunnite, chlorargyrite) within voids in the veins and produced alteration haloes in wallrocks surrounding entire vein systems.

Low sulfide high-PGE mineralization in the Coleman environment derives from metal-loaded aqueous fluids that were derived from an unknown source and became hydrocarbon-enriched (Hanley et al. 2005; Kerr 2013) over the course of their evolution. This fluid entered the footwall utilizing many of the same structural

pathways as the sharp-walled veins. As it descended into the footwall and the temperature dropped, end-member PGE-arsenides, PGE-bismides, PGE-tellurides, and PGE-bismuthotellurides (i.e. end-members exhibiting no solid solution between Pt-Pd, Bi-Te, etc.) were the first phases to crystallize. With progressive cooling, the aqueous fluid became increasingly reducing (in stark contrast to the progressively oxidizing conditions recorded in the late stages of crystallization in the sharp-walled vein systems) upon reacting with deep $CaCl_2$-rich ground water. Reduction is recorded in the ore mineralogy of low sulfide samples by the primary equilibrium presence of phases from the sulfbismuthite mineral group (parkerite, aikinite, wittichenite, crerarite, As-bearing argentocuprocosalite). Progressive dilution of the hydrocarbon-enriched aqueous fluids by $CaCl_2$-rich groundwater resulted in the precipitation of calcic silicates and carbonates which triggered the paragenetically-late precipitation of bornite, chalcopyrite, and millerite to round-out the low sulfide assemblages.

2.0 Introduction

Footwall Cu-Ni-PGE mineral deposits mined along the outskirts of the North Range of the Sudbury Igneous Complex (SIC) have seen progressive interest from an exploration standpoint since the new millenium due to their anomalously high base metal (Cu, Ni) contents and precious metal tenors. The division of footwall deposits at Sudbury into "high sulfide" (sharp-walled vein) and "low sulfide" (PGE-rich) systems was identified within the last decade using large geochemical mine databases (Farrow et al. 2005) which formed the foundation for more focused research to be undertaken in recent years. An enormous source of literature produced over the last century characterized the base metal-, precious metal- and alteration-mineralogy of numerous different footwall deposits within the North Range area (i.e. Naldrett and Kullerud 1967; Cabri and Laflamme 1976; Naldrett 1984; Li et al. 1992; Li and Naldrett 1993; Money 1993; Farrow 1994; Kormos 1999; Hanley and Mungall 2003; Ames et al. 2007; Péntek et al. 2008, Ames and Kjarsgaard 2013 etc.). Footwall mineralization at Vale's Coleman Mine (Figure 2.1, Figure 2.2 a) provides a unique opportunity to study very deep and contrasting styles of Cu-Ni-PGE mineralization. While one might anticipate the overall characteristics of these deposits to be akin, the precious metal mineralogy of individual deposits is often very specific, the alteration mineralogy variable, and individual zone grades can vary substantially.

Genetic models of formation for high sulfide- and low sulfide-styles of footwall mineralization have been addressed from many angles in the literature.

There is a general consensus that high sulfide mineralization was formed predominantly through magmatic/magmatic-hydrothermal processes (Li et al. 1992; Naldrett et al. 1999; Péntek et al. 2008) and that low sulfide mineralization formed solely through the circulation of metal-bearing hydrothermal fluids (Péntek et al. 2008; Tuba et al. 2010; Nelles et al. 2010; Hanley et al. 2011). Additionally, Farrow et al. (2005) have illustrated that (at least in this area) the formation of low sulfide mineralization pre-dates the formation of high sulfide mineralization on the basis of cross-cutting relationships on a large stripped outcrop within the North Zone at the Podolsky deposit (Figure 2.1 a). However, the conditions associated with the formation of low sulfide mineralization (fluid sources, transport mechanisms, fO_2 of fluids, etc.) and the extent to which these two physically and chemically different styles of mineralization are related, have remained enigmatic.

The purpose of this paper is to provide a comprehensive mineralogical/ metallogenic characterization and comparison of high sulfide (sharp-walled vein) and low sulfide (disseminated, blebby, stringer) Cu-Ni-PGE footwall mineralization in the area of the deep 153 & 170 ore bodies at the Coleman Mine (Onaping-Levack area, Sudbury) and to address stope-scale mineralogical/metallogenic variability along an individual sharp-walled vein ("Vein 1") within the 170 ore body (Figure 2.2 b, c). The signature styles of hydrothermal alteration associated with each mineralization style are also presented; along with how these alteration styles relate to ore metal grades. A general consensus regarding the relationship (or lack thereof) between high sulfide and low sulfide footwall Cu-Ni-PGE mineralization does not

exist at present and this research addresses this issue. The results of this study complement other mineralogical work that has been completed in the area (e.g., Li et al. 1992; Li and Naldrett 1993; Money 1993; Kormos 1999; Nelles 2012; Dare 2014 etc.) and together these studies provide insight into the homogeneity of Cu-, Ni-, and PGE-rich ore systems within the North Range footwall.

2.1 Geological setting

The Sudbury Igneous Complex (SIC) is a large (~ 60 km x 30 km), folded, elliptical remnant of igneous rock located geographically around the area of Sudbury, Ontario and overprints the contact between the Superior and Southern Provinces within the Canadian Shield (Figure 2.1 a). The SIC is an originally flat-lying layered mass of igneous rock composed (from base upwards) of noritic, quartz gabbroic, and granophyric segments (Ames et al. 2008); and is widely accepted to have been produced through flash melting of the crust immediately following meteorite impact at ~1850 Ma (Krogh et al. 1984; Mungall et al. 2004). Lithologies overlying the SIC are comprised of crater-fill breccias grading into deep marine sediments - collectively termed the Whitewater Group (Rousell, 1984; Ames et al. 2002; Mungall et al. 2004). Support for the SIC impact hypothesis (Dietz 1964) includes: iridium anomalies in lithologies overlying the SIC (Mungall et al. 2004), shatter cones in country rocks surrounding the SIC (Dietz 1964), shock metamorphosed minerals in lithologies immediately surrounding the SIC (below and above: Grieve et al. 2012; French et al. 2005) and in distal ejecta identified in the Lake Superior region 650-875 km away (Addison et al. 2005; Ames et al. 2008),

Superior Province (Archean; 2.70-2.75 Ga)

- Granitoids, migmatites
- Levack Gneiss Complex

Southern Province (Early Proterozoic; 2.10-2.46 Ga)

- Huronian Supergroup
- Nipissing diabase
- Granitoid bodies

Sudbury Igneous Complex (Early Proterozoic; 1.85 Ga)

- Main Mass (Lower zone norite, Middle zone quartz gabbro, Upper zone granophyre)
- Contact sublayer

Whitewater Group (Early Proterozoic; 1.85-1.90 Ga)

- Onaping Formation
- Onwatin Formation
- Chelmsford Formation

- Cu-Ni-PGE "footwall" deposits & occurrences
- – – – Fault

Podolsky

Nickel Rim
Nickel Rim Depth
Nickel Rim South

Broken Hammer Zone
South Zone

Barnet
Coleman
Strathcona
Fraser
McCreedy East
Levack
McCreedy West

Onaping
Chelmsford
Onwatin

Sudbury

Québec
Ontario
Sudbury
Toronto
USA

500 km

10 km

N

22

Figure 2.1 (previous page): Geological map of the Sudbury Igneous Complex (SIC) and location of Vale's Coleman Mine. The position of the Coleman Mine is highlighted by a star symbol and the locations of all other known footwall-style deposits and occurrences are indicated as well (Ames and Farrow 2007).

strongly brecciated rocks underlying the SIC (Rousell et al. 2003), and systematic decreases in brecciation intensity within host rocks moving away from the SIC (Ames 2007).

Nickel, Cu, and PGE mineral deposits have long been recognized to occur along the base of, and within the footwall to the SIC; and have since been divided into 3 distinct ore groups based on both their geological settings and metal contents. *Contact deposits (Ni-Cu-Co)* represent >50% of the historical resource for deposit styles associated with the SIC (Lightfoot et al. 2001), and are located within embayments along the basal contact of the SIC with its footwall. These relatively large massive to semi-massive deposits are enriched in Ni, Ir, and Rh (compared to the other SIC-associated deposits), which is manifested by an ore mineral assemblage consisting of massive pyrrhotite, with lesser and variable pentlandite, chalcopyrite, magnetite, and pyrite (Naldrett 1984). The next most abundant (Ni-Cu-PGE) resource at Sudbury reside as *offset dyke deposits* (Ames and Farrow 2007). These Ni-, Cu-, and precious metal-containing mineral deposits are hosted in radial or concentric offset dykes with multiple magmatic pulses of quartz diorite composition that emanate from the SIC into its country rock – representing early quenched impact melt and an approximation of the SIC's bulk composition (Lightfoot et al. 2001). *Footwall deposits* comprise less than 10% of Sudbury's historical metal resource (Farrow and Lightfoot 2002), but have become increasingly attractive exploration targets over the past 30 years (Ames 2007) due to their marked enrichments in Cu, Pt, Pd, Ag, and Au compared to contact- and

offset dyke-style deposits (Morrison et al. 1994). Footwall deposits are most prevalent along the North and East ranges at Sudbury, are completely contained within the SIC footwall, and are subdivided into "high sulfide" sharp-walled vein and "low sulfide" high-PGE members. Sharp-walled veins, which are characterized by >90% sulfide minerals by volume - dominantly chalcopyrite away from contact deposits (Farrow et al. 2005) - may reach widths >1 m, and are composed of massive chalcopyrite with lesser amounts of cubanite, pentlandite, millerite, magnetite, sphalerite, pyrrhotite, and pyrite; as well as a large suite of discrete, heavy metal-bearing mineral phases (i.e. the precious metal minerals moncheite, michenerite, froodite, hessite, etc.). Low sulfide-mineralized samples contain <5% sulfide minerals by volume (Farrow et al. 2005), and are characterized by blebs, disseminations, and stringers of bornite, chalcopyrite, and millerite; along with numerous discrete precious metal mineral phases. Mineralogical and textural differences aside, low sulfide samples can be differentiated from high sulfide samples on the basis of their bulk rock chemistries – PGE/S values in low sulfide mineralization can reach up to an order of magnitude higher than those in high sulfide mineralization (Farrow et al. 2005).

The North Range of the SIC hosts a large set of Ni, Cu, and PGE mineral deposits that are most commonly spatially associated with embayment structures (Morrison 1984). Embayments are complex depressions of the basal contact of the SIC (involving both SIC- and basement rock-elements) that have been interpreted as slump features where meterorite impact processes created *in-situ* areas of

structurally weakened basement rock (Fedorowich et al. 1999). The Strathcona Embayment is a multi km-scale structure with an average plunge of 21° SSW (McCormick et al. 2002) that is located around many well-developed Ni, Cu, and PGE mineral deposits along the North Range including the Coleman, Strathcona, McCreedy East, and Fraser mines. To the west lies another North Range embayment structure, "The Levack Embayment," that hosts the Hardy, McCreedy West, Levack, Morrison, and Craig contact deposits (Morrison 1984). Basement rocks around this area of the SIC are dominated by (migmatitic) tonalitic to granodioritic gneisses of the Archean Levack Gneiss Complex with minor mafic lithologies (Card 1994). Impact-related cataclastic to pseudotachylitic breccia termed *Sudbury Breccia* are distributed around the SIC (Ames et al. 2005, 2008) in zones reaching as far away as 80 km into the footwall country rocks (Thompson and Spray, 1994) and are the main host of the footwall-type Cu-Ni-PGE mineral deposits; which are generally positioned ≤2 km from the SIC contact. Sudbury Breccia occurs as (mm- to km-scale) irregular shaped bodies, veins, and veinlets that are composed of cm- to m-scale clasts and blocks (of fragmented country rock) set in an aphanitic matrix (Legault et al. 2003; Rousell et al. 2003). These syn-impact pseudotachylite breccia zones extend into the footwall away from the SIC contact, and, early on during differentiation and crystallization of the SIC, likely served as structural pathways for dense sulfide liquids that would have ultimately crystallized to form the footwall packages of ore that are sought after today (Rousell et al. 2003; Péntek et al. 2008). The Coleman deposit within the Strathcona Embayment hosts both contact Ni-rich ore bodies and deep high/low sulfide mineralization distal (3370-5440 levels) from

the basal SIC contact within the 153 and 170 ore bodies, respectively (Figure 2.2 a). Coleman 153, is the most westerly-positioned ore body in the Strathcona Embayment of the SIC footwall and is separated from known ore bodies in the east by the late Bob's Lake fault. It is also cut by an olivine diabase dyke of the 1238 ± 4 Ma "Sudbury dike swarm" (U-Pb baddeleyite, Krogh et al. 1987). Along the eastern side of the downward-extension of the Bob's Lake Fault, the Coleman 170 ore body has been delineated as a tabular structure that cuts off just east of the Lunch Room Fault (looking north). The relationship between the 153 & 170 ore bodies has yet to be established, particularly whether they were once part of a singular unit prior to the last movement on the Bob's Lake Fault. Sudbury Breccia packages and bimodal gneissic units comprise the predominant host lithologies for Cu-Ni-PGE mineralization within this area of the SIC footwall.

2.2 Methods

Over 130 hand samples of Cu-Ni-PGE mineralization and wallrock alteration were collected from the 153 & 170 ore bodies at levels 4250, 4810, 4945, 5440, and 5080 of the Coleman Mine. A systematic suite of 25 rock chip samples was collected underground (Figure 2.2 c) and 106 additional samples were gathered at Vale's Copper Cliff core shack from drill core (BHID: 1283350, 1283870, 1283360, 1296290 and 1296300) extracted through areas of the 153 and 170 ore bodies including the low sulfide "PM Zone," an extension of the McCreedy East Mine ore body (Figure 2.2 a; Farrow et al. 2005). Petrography was completed on 100 thin/thick sections comprising "high sulfide" mineralization, "low sulfide"
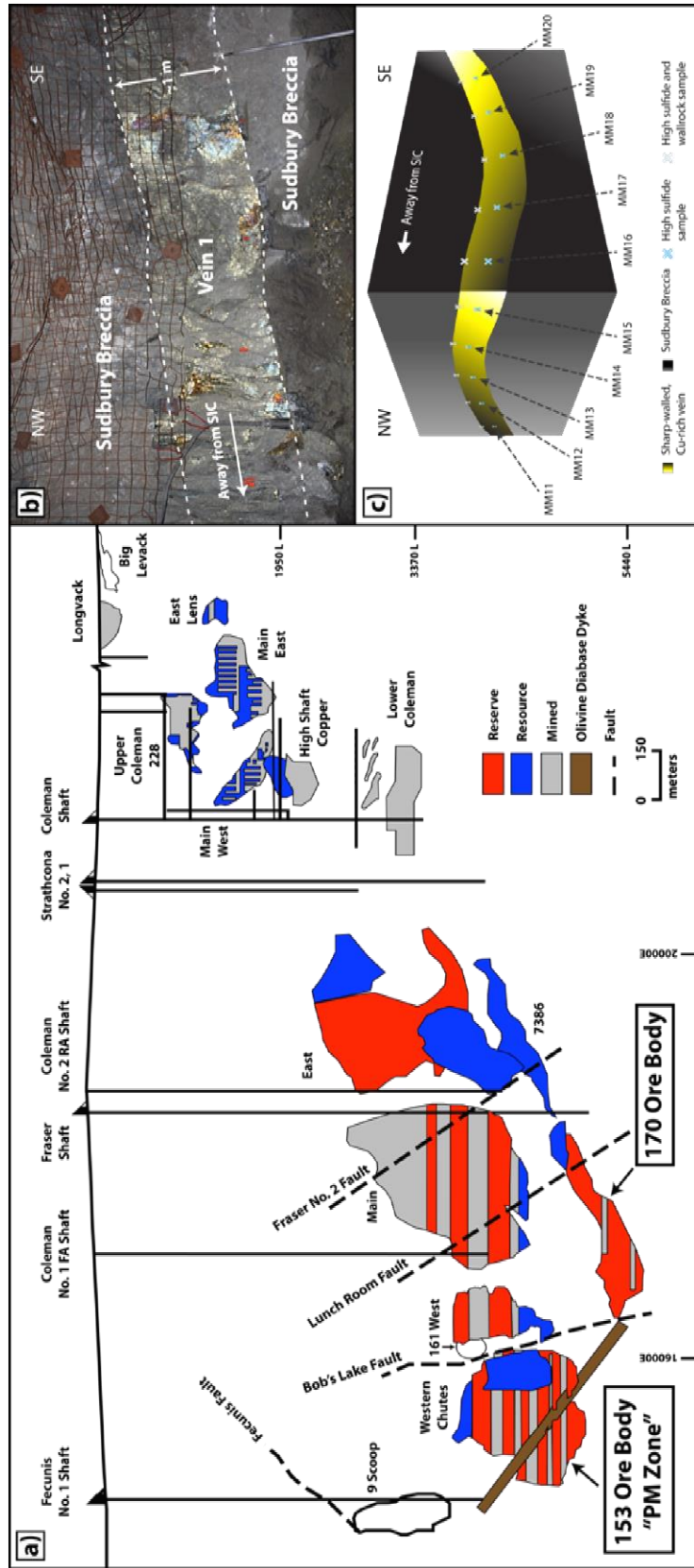
Figure 2.2 (previous page): Prominent geological features in the area of Vale's Coleman Mine. a) W-E longitudinal section, Coleman Mine. The deep 153 & 170 ore bodies are situated furthest away from the SIC relative to other occurrences of mineralization in this area of the SIC footwall (modified from Vale, Coleman Mine). b) Digital image of a segment along "Vein 1" displaying uniform vein width of ~ 1 meter. Scaling bar at bottom right for scale (170 Ore body, Level 5440, Cut 33). c) Diagram illustrating the sampling procedure for "Vein 1". Ten high sulfide samples were collected along the vein's core at 1-meter intervals (blue X's). Additionally, 20 samples were collected near the vein-wallrock contact at 1-meter intervals (grey X's). Each of the latter sample sites provided two samples. The first type comprised wallrock samples taken <20 cm into the wallrock away from the contact. The second type comprised high sulfide samples taken <20 cm into the vein away from the contact. The white arrow near the top of the image points in a direction that is further away from the SIC contact and deeper into the footwall to the SIC.

mineralization, and wallrock alteration using a Nikon Eclipse H550L microscope. Modal abundances for all phases reported in each section were calculated by highlighting and calculating the total area occupied by each phase in several representative photomicrographs using a threshold function in *ImageJ*, and doing a calculation that applies that area through the entire thin section. Forty of these samples have been characterized for their discrete, heavy metal-bearing phases using the LEO 1450VP scanning electron microscope (SEM) at Saint Mary's University. This instrument has an attached energy dispersive X-ray (EDS) Oxford INCA 80 mm^2 SDD detector capable of (semi-) quantitative analysis. The machine was operated at a working distance of 20 mm, beam current of 40 µA, and accelerating voltage of 20.00 – 25.00 kV for all analyses. Raw data was reduced using the software package LEO32.

Sulfide and oxide minerals in 23 samples from various levels in the 153 and 170 ore bodies, and along the length of "Vein 1" from the 170 ore body, were analyzed by laser ablation inductively coupled plasma mass spectrometry (LA-ICPMS) for their major, minor, and trace metal compositions at the GSC in Ottawa (Table 2.6). The instrument used was an *Agilent 7700 Quadrupole ICP-MS* that achieved sample introduction using a 193 nm Ar-F excimer laser and helium carrier gas. Three standards were bracketed between every 11 analyses of sulfide samples. USGS *GSE-1G*, a synthetic basaltic glass (routinely used for the calibration of mixed sulfides, silicates, carbonates), was used as the main calibration material during measurements. The MUN *LaFlamme* (Po-726) standard was used to calibrate

measurements of PGE's and Au. USGS *Mass-1* (synthetic sulfide pressed pellet) was analyzed with the standards for quality control purposes. The procedure for each analysis consisted of measuring 40 seconds of gas blank with the laser idle, followed by 65 seconds of sample ablation. The laser conditions used were: repetition rate of 10 Hz, energy of 2 mJ, and a spot size of 43 μm. The only exceptions were analyses of large magnetite grains, where a larger spot size (86 μm) was used, and analyses of very small grains, where a spot size of 43 μm would cause the measurements to be contaminated by the host phase, so smaller spot sizes had to be employed. All raw data was reduced using *Glitter* data reduction software (version 4.4.3). Due to the interference of $^{65}Cu+^{40}Ar$ on ^{105} Pd, ^{105}Pd was not included during integration of the Pd measurements. ^{106}Cd and ^{108}Cd isobaric interferences on ^{106}Pd and ^{108}Pd were corrected using the measured ^{111}Cd. Also, ^{99}Ru, ^{101}Ru, and ^{102}Ru will not be reported for millerite due to $^{59}Co^{40}Ar$, $^{61}Ni^{40}Ar$, and $^{62}Ni^{40}Ar$ interferences. Lastly, bulk rock assays were analyzed by SGS*é*Actlabs (funded by Vale) in late 2012 on 161 samples comprising high sulfide mineralization, low sulfide mineralization, and wallrock alteration using the standards ME-ICP61, Ag-AA62, Cu-AA62, Ni-AA62, Zn-AA62, Pb-AA62, PGM-ICP23, Au-GRA21, PGM-ICP27, and S-IR08.

2.3 Characteristics to distinguish between "high sulfide" and "low sulfide" styles of Cu-Ni-PGE mineralization within footwall ore packages at the Coleman Mine

The "high sulfide" style of Cu-Ni-PGE mineralization is recognized by spectacular occurrences of chalcopyrite-rich veins and veinlets that can locally reach widths on the order of several meters and consist of >90% sulfide minerals (Figure 2.2 b, Figure 2.3 a). This style of mineralization is referred to as "*sharp-walled*" due to the extremely sharp decrease (spatially) in sulfide contents moving across vein-contacts into wallrocks immediately adjacent to massive sulfide veins. The vein wallrocks have also been shown to display variably developed hydrothermal overprints in the vicinity of vein margins that are manifested by the presence of secondary (often Cl-rich) hydrous mineral phases such as quartz, epidote, chlorite, and amphibole (Farrow and Watkinson 1992; Farrow 1994; Hanley and Mungall 2003).

The "low sulfide" style of Cu-Ni-PGE mineralization is recognized as intergrown blebs, disseminations, and stringers of sulfide minerals that generally occur on millimeter- to decimeter-scales and typically comprise <5% of any given fist-sized hand sample (Figure 2.3 b). The presence of the relatively Fe-poor (compared to other major sulfide phases at Sudbury) mineral bornite (Cu_5FeS_4), along with the occurrence of hydrothermal packages consisting of quartz+calcite+epidote+chlorite that are texturally equilibrated with the sulfides, are key characteristics that permit identification of low sulfide mineralization.

Distinguishing between these mineralization styles can be done accurately on a macroscopic basis through basic textural/mineralogical criteria; however, chemical differences differentiate them unambiguously (Farrow et al. 2005). There are notable bulk rock differences in S vs. Pt+Pd trends between high sulfide and low sulfide samples and PGE/S ratios may reach up to an order of magnitude higher within low sulfide mineralization. The Coleman high- and low-sulfide mineralization shown on the S vs. Pt+Pd differentiation scheme (Figure 2.3 c) displays this spike in PGE/S ratios for a few of the low sulfide samples. These mineralization styles can be more readily distinguished using trace elements in other binary differentiation schemes (Fe vs. Ag+Au, Zn vs. Cr) (Figure 2.3 d, e). This study identifies the trace elements (Ag, Au, Cr, Zn, Pt, Pd) that characterize the two chemically distinct fields of Cu-Ni-PGE mineralization.

2.4 Ore Mineralogy

2.4.1 Mineralogical characteristics: "High sulfide" sharp-walled vein mineralization

"High sulfide" mineralization occurs as stockwork vein-systems comprising millimeter- to meter-scale veins/veinlets that are characterized by mineral assemblages of massive chalcopyrite with locally abundant concentrations (>50 vol%) of pentlandite, millerite, and cubanite (Figure 2.4). Pentlandite and millerite commonly occur near the margin edges of large massive chalcopyrite veins or in massive form within smaller veinlets splaying off larger sharp-walled veins, and thus have a strong affinity for wallrock. Cubanite forms minor exsolution lamellae in chalcopyrite that are ubiquitous when present. Magnetite (<5 vol%) is a
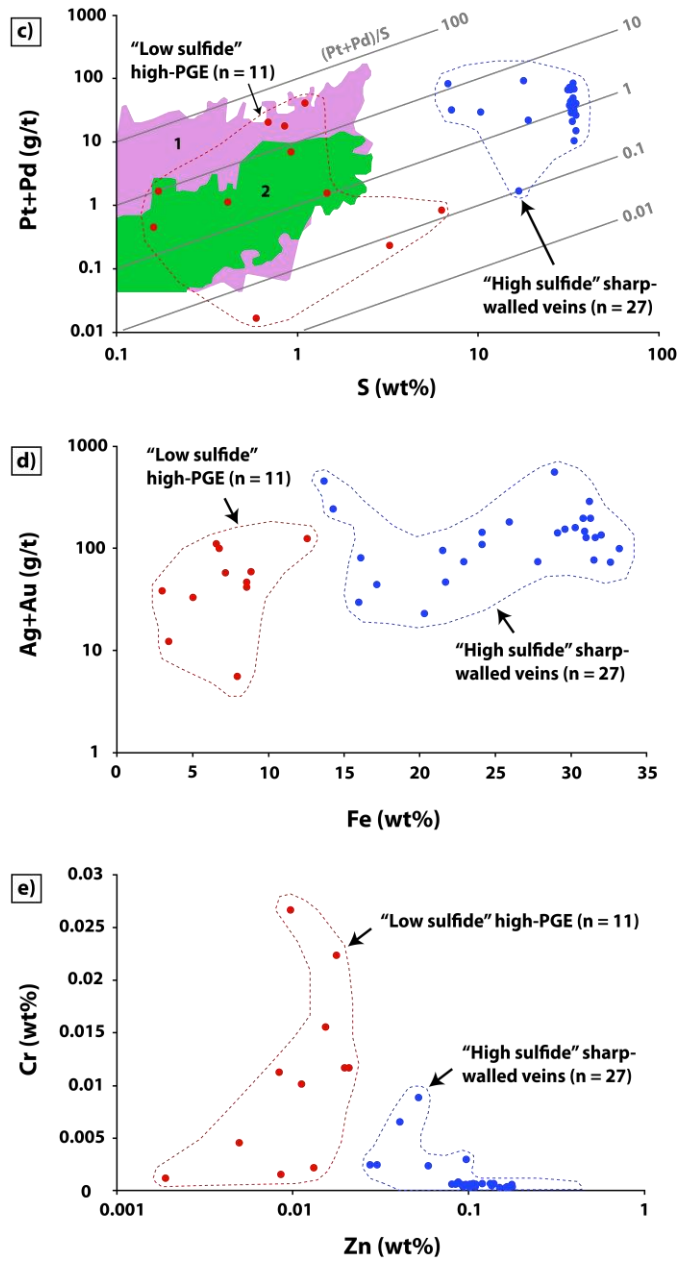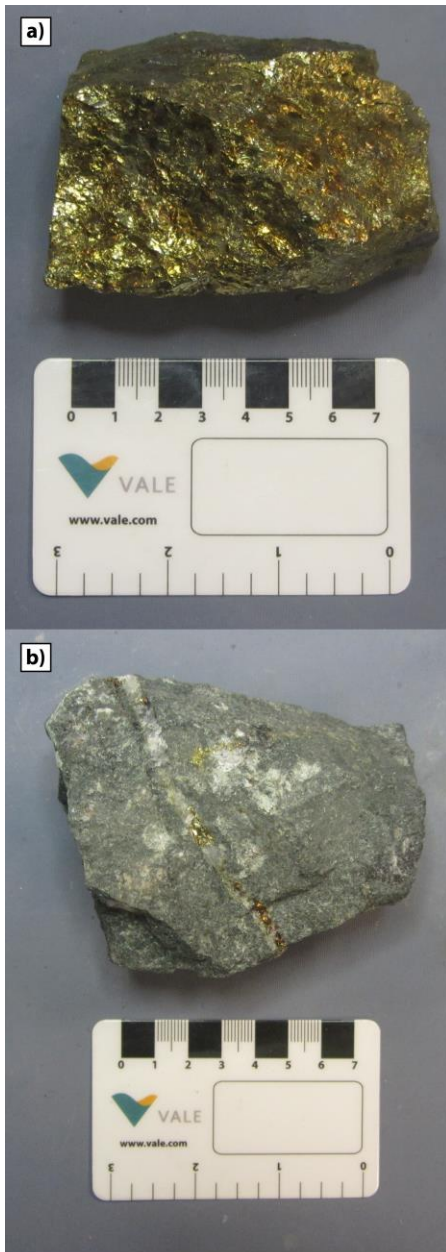
Figure 2.3 (previous page): Discriminants for "high sulfide" and "low sulfide" samples from the Coleman Mine using macroscopic/field and geochemical criteria. See digital appendix for supplementary data. a) Representative high sulfide (sharp-walled vein) chip sample consisting of massive chalcopyrite with >90% sulfide minerals by volume. b) Low sulfide (high-PGE) chip sample consisting of disseminations, blebs, and stringers of sulfide minerals contained within quartz-calcite-epidote assemblages that are hosted in Sudbury Breccia. Chips samples of low sulfide mineralization contain <5% sulfide minerals by volume. c) Plot of S (wt%) vs. Pt+Pd (g/t) using available bulk rock data for a series of high sulfide and low sulfide samples. Pt+Pd values for low sulfide mineralization can be comparable to those of high sulfide mineralization – resulting in Pt+Pd/S ratios for low sulfide samples that are up to an order of magnitude higher than those in high sulfide mineralization. High sulfide (#2) and low sulfide (#1) fields from the McCreedy West Mine (Farrow et al. 2005) are included as the green and pink fields. d) Precious metal discrimination diagram showing Fe (wt%) vs. Ag+Au (g/t), data this study only. Low sulfide samples are characterized by similar bulk Ag+Au values, with much lower bulk Fe values compared to high sulfide samples. e) Additional base metal discrimination diagram for high vs. low sulfide mineralization, Coleman Mine. The bivariate diagram of Zn (wt%) vs. Cr (wt%) illustrates that the low sulfide samples contain more bulk Cr and less bulk Zn compared to high sulfide samples.

minor vein phase that is present as sub-rounded to rounded inclusions within base metal sulfides along with trace sphalerite, pyrrhotite, and pyrite (Figure 2.4 b, c). High sulfide mineralization can be divided into three mineralogically different subgroups in order of prevalence:

1) *Ni-rich group*: Ccp+Pn+Mil+Mt+Sph±Po (most common)
2) *Fe-rich group*: Ccp+Cub+Py+Mt+Sph+Po±Pn
3) *Bornite group:* Bn+Ccp+Mil (least common)

The Ni-rich group was the most commonly observed high sulfide subgroup within both the 153 and 170 ore bodies. Millerite and cubanite do not co-exist in a single sample within any of the 3 subgroups and it should also be noted that samples from the Fe-rich group at Coleman have Ccp:Cub ratios >>3:1 – a ratio reported from high sulfide samples in the Deep Copper Zone, Strathcona Mine (Li et al. 1992; Li and Naldrett 1993). The precious metal mineralogy of both Ni- and Fe-rich groups consists of moncheite $(Pt,Pd)(Te,Bi)_2$, michenerite PdBiTe, hessite Ag_2Te, and native silver Ag, along with other localized Pt-, Pd-, Ag- and Au-containing phases; all of which are most commonly contained within the volumetrically-dominant sulfide: chalcopyrite (Table 2.2). Finally, the third and least common group of high sulfide mineralization is the bornite group. This group comprises massive bornite, chalcopyrite, and millerite that occur at the terminations of sharp-walled vein systems (Figure 2.4 d). One sample from this group was collected in this project and its precious metal mineralogy was dominated by moncheite $(Pt,Pd)(Te,Bi)_2$, hessite Ag_2Te, and naumannite Ag_2Se.

2.4.2 Wallrock alteration: "High sulfide" sharp-walled vein mineralization

The mineralogy of wallrocks along the margins of sharp-walled veins in the 153 and 170 ore bodies was systematically analyzed (Figure 2.2 c) and the exclusive host is Sudbury Breccia which was developed in leucocratic gneisses. The host breccia contains remnant blocks of granitoid protolith separated by fine-grained networks of intergrown chlorite crystals. The granitoid clasts are variably overprinted by secondary hydrothermal mineral phases (quartz, chlorite, epidote, titanite, hornblende, actinolite, apatite, stilpnomelane) and all remaining plagioclase is nearly pure albite (Ab_{90-100}). Representative petrographic and back-scattered electron (BSE) images for high sulfide mineralization and alteration are presented in Figure 2.4. Modal abundances, grain sizes, identifying features, and key textures for each high sulfide alteration phase are covered in Table 2.4.

2.4.3 Mineralogical characteristics: "Low sulfide" PGE-rich mineralization

"Low sulfide" mineralization occurs as ≤decimeter-scale blebs, disseminations, and stringers of sulfide minerals that are intergrown with hydrous mineral assemblages and are hosted in both Sudbury Breccia and bimodal gneissic units in and around the "precious metal/mineral zone" within the 153 ore body. The sulfides consist of bornite, chalcopyrite, and millerite that co-precipitated in this environment (Figure 2.5). Their precious metal minerals consist of a variety of Pt-, Pd-, Ag-, and Au-containing phases which display less *in-situ* chemical variability compared to precious metal minerals in high sulfide samples (i.e. end members occur more often) and are most commonly hosted within base metal sulfides or

along silicate grain margins (Figure 2.5, Table 2.3). All the discrete ore minerals that were identified in this study within both high sulfide and low sulfide samples are listed in Table 2.1; with further characterization of these minerals provided in Table 2.2 and Table 2.3. Quartz-epidote is the diagnostic alteration package associated with low sulfide mineralization. Textural varieties (poikilitic, grain boundary relationships) suggest that the alteration packages are coeval with or preceded precipitation of the base metal sulfides. Low sulfide alteration can be divided into three basic mineral assemblage types:

1) *Calcite-free assemblages*: quartz, epidote, chlorite, amphibole (actinolite, hornblende), titanite, apatite, k-feldspar, plagioclase, clinopyroxene (augite)

2) *Calcite-bearing assemblages*: quartz, epidote, calcite, chlorite, titanite, Na-Cl silicate, k-feldspar, plagioclase

3) *Garnet-bearing assemblages:* quartz, epidote, chlorite, calcite, garnet (andradite, grossular), amphibole (actinolite, calcic amphibole), rutile, clinopyroxene (augite)

The majority of the minerals listed in these 3 groups represent hydrothermally-precipitated phases that are associated with formation of the sulfides. However, a few of them are relict phases (i.e. clinopyroxene), while some comprise both relict and secondary hydrous phases (i.e. quartz). Representative petrographic and BSE images for low sulfide mineralization and alteration are presented in Figure 2.5 and modal abundances, grain sizes, identifying features, and key textures for each low sulfide alteration phase are covered in Table 2.4 and Table 2.5.

Table 2.1: Discrete, heavy metal-bearing ore minerals identified by SEM-EDS in 40 samples comprising both "high sulfide" and "low sulfide" styles of footwall Cu-Ni-PGE mineralization.

Ore Mineral	Formula	Environment
Bismuthotellurides		
Moncheite	$(Pt,Pd)(Te,Bi)_2$	High sulfide, low sulfide
Merenskyite	$(Pd,Pt)(Te,Bi)_2$	High sulfide, low sulfide
Michenerite	$(Pd,Pt)BiTe$	High sulfide, low sulfide
Maslovite	$PtBiTe$	Low sulfide
Kotulskite	$Pd(Te,Bi)$	High sulfide, low sulfide
Bismuthian palladian melonite	$(Ni,Pd)(Te,Bi)_2$	Low sulfide
Unnamed Pd-Pt-Bi-Te mineral	$(Pd,Pt)(Bi,Te)_2$	High sulfide, low sulfide
Tsumoite	$BiTe$	Low sulfide
Bismuthides		
Insizwaite	$Pt(Bi,Sb)_2$	Low sulfide
Froodite	$PdBi_2$	High sulfide, low sulfide
Sobolevskite	$PdBi$	High sulfide, low sulfide
Tellurides		
Hessite	Ag_2Te	High sulfide, low sulfide
Kurilite	$(Ag,Au)_2(Te,Se,S)$	High sulfide
Sulfbismuthides		
Crerarite	$Pt_{2-x}(Bi,Pb)_{11}(S,Se)_{11}$	Low sulfide
As-bearing argentocuprocosalite	$(Pb,Cu,Ag)_2Bi_2S_5$	Low sulfide
Parkerite	$Ni_3Bi_2S_2$	High sulfide, low sulfide
Wittichenite	Cu_3BiS_3	Low sulfide
Aikinite	$PbCuBiS_3$	Low sulfide
Sulfides		
Acanthite	Ag_2S	High sulfide, low sulfide
Bismuthiferous galena	$(Pb,Bi,Ag)S$	Low sulfide
Galena	PbS	High sulfide, low sulfide
Hawleyite	CdS	High sulfide
Molybdenite	MoS_2	High sulfide
Stannides		
Niggliite	$PtSn$	High sulfide
Paolovite	Pd_2Sn	High sulfide
Arsenides		
Sperrylite	$PtAs_2$	High sulfide, low sulfide
Menshikovite	$Pd_3Ni_2As_3$	High sulfide
Selenides		
Naumannite	Ag_2Se	High sulfide
Geffroyite	$(Cu,Fe,Ag)_9(Se,S)_8$	High sulfide
Clausthalite	$PbSe$	High sulfide
Native elements/alloys		
Native silver	Ag	High sulfide, low sulfide
Electrum	(Au,Ag)	High sulfide, low sulfide
Native zinc	Zn	Low sulfide
Chlorides		
Chlorargyrite	$AgCl$	High sulfide, low sulfide
Cotunnite	$PbCl_2$	High sulfide, low sulfide
Oxides		
Bismite	Bi_2O_3	High sulfide, low sulfide
Cassiterite	SnO_2	High sulfide, low sulfide
Paratellurite	TeO_2	High sulfide
Tenorite	CuO	Low sulfide
Zincite	ZnO	High sulfide
Sulfates		
Barite	$BaSO_4$	High sulfide, low sulfide
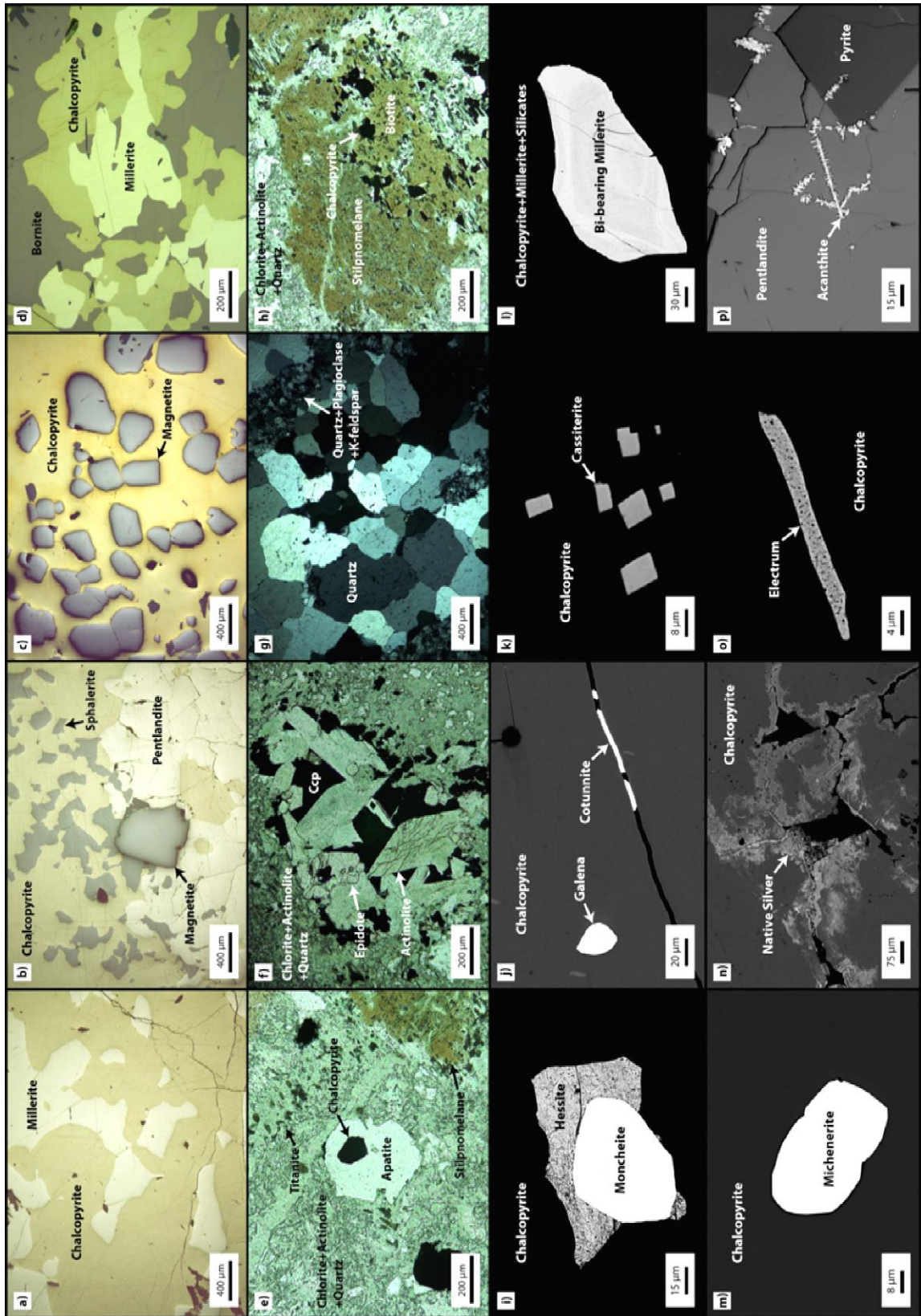
Figure 2.4 (previous page): Mineralogical characteristics of "high sulfide" mineralization in thin section. See digital appendix for sample numbers associated with each image. a) Randomly distributed blebs of millerite in chalcopyrite matrix. b) Anhedral aggregates of pentlandite in chalcopyrite that contain a sub-rounded inclusion of magnetite. Chalcopyrite and pentlandite also host a trail of sphalerite disseminations. c) Ubiquitous euhedral-subhedral magnetite inclusions in chalcopyrite matrix. d) Massive intergrown bornite, chalcopyrite, and millerite from vein termination ("bornite-group" sample). e) Euhedral crystal of apatite containing an inclusion of chalcopyrite. The apatite crystal displays a diagnostic hexagonal outline. Surrounding assemblage consists of a dense network of chlorite, actinolite and quartz. Stilpnomelane occurs at the bottom right and trails of massive, foliated chlorite containing titanite inclusions are seen at top right. PPL. f) Euhedral crystals of actinolite and granular epidote spatially associated with chalcopyrite. The surrounding matrix is predominantly chlorite, actinolite and quartz. The large actinolite grain in the lower central portion of the image displays the diamond-shaped basal section with diagnostic 56-124 amphibole cleavage. PPL. g) Aggregates of quartz grains containing trails of finer-grained (paragenetically earlier) k-feldspar, plagioclase and quartz blocks at top right and bottom left. XPL. h) Abrupt contact between biotite and stilpnomelane. The surrounding assemblage consists of chlorite, actinolite and quartz. Chalcopyrite disseminations are concentrated where biotite is being replaced by chlorite. PPL. i) Composite grain of hessite and moncheite hosted in chalcopyrite. j) Cotunnite filling a crack in chalcopyrite; anhedral inclusion of galena in chalcopyrite. k) Cluster of euhedral cassiterite inclusions in chalcopyrite. l) Anhedral inclusion of bismuth-bearing millerite in a host composed of chalcopyrite, millerite and silicates. m) Anhedral michenerite inclusion in chalcopyrite. n) Thin coatings of native silver on chalcopyrite near cracks and cavities in chalcopyrite. o) Elongate electrum inclusion in chalcopyrite. p) Trails of acanthite inclusions in massive pentlandite that are either isolated or aligned along the edges of euhedral pyrite grains.
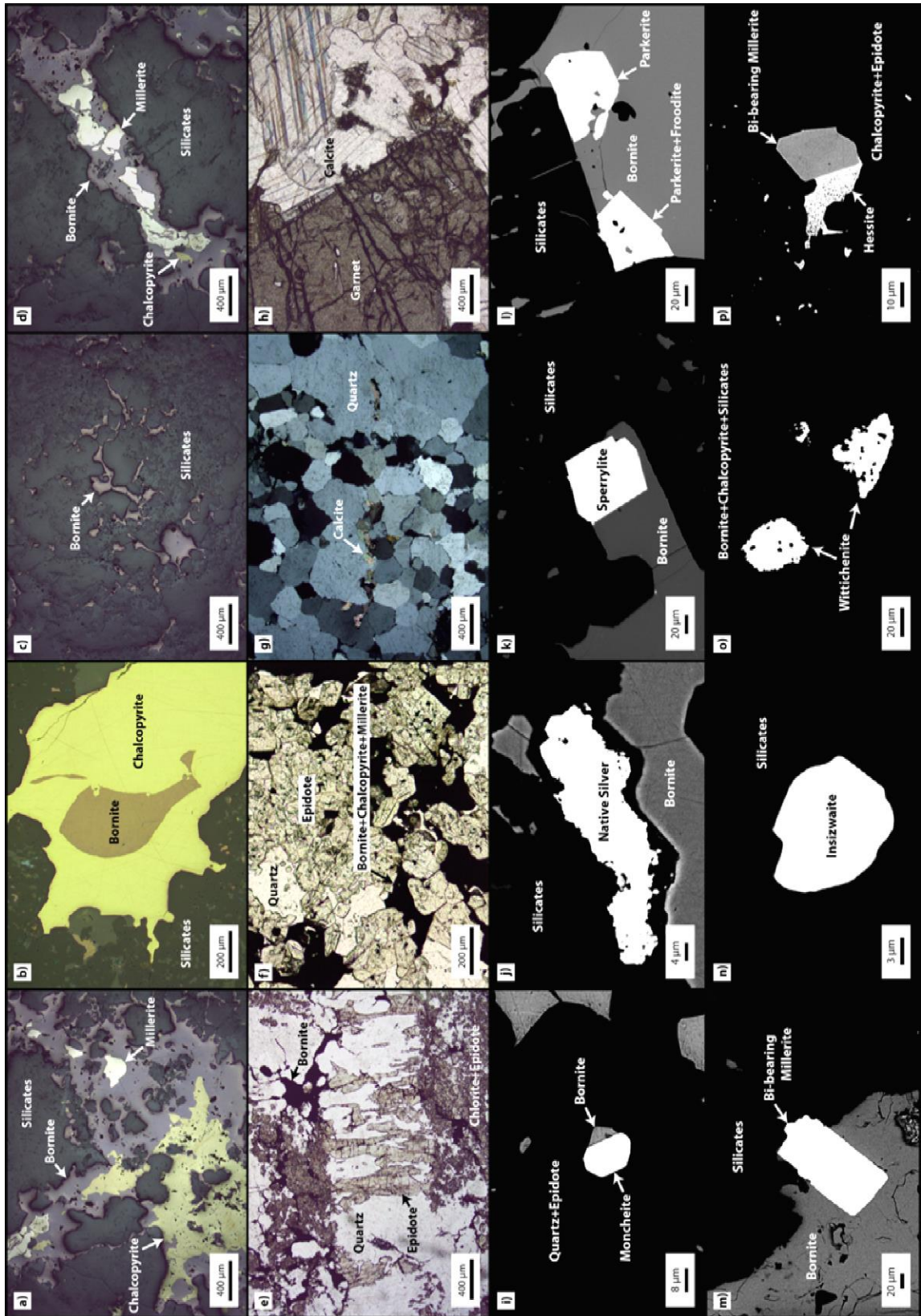
Figure 2.5 (previous page): Mineralogical characteristics of "low sulfide" mineralization in thin section. See digital appendix for sample numbers associated with each image. a) Intergrown masses of bornite and chalcopyrite; containing millerite inclusions, in silicate gangue. b) Blebs of bornite contained in a silicate-hosted chalcopyrite dissemination. c) Bornite disseminations in silicate gangue. d) Trail of bornite that is hosted in silicate gangue and contains millerite inclusions. e) Elongated/internally deformed grains of quartz and epidote forming a "comb-like" texture veinlet within a quartz, chlorite and epidote host. Networks of bornite are visible along the veinlet margins. PPL. f) Intergrown epidote, quartz and sulfides (bornite, chalcopyrite, millerite). PPL. g) Trails of calcite within aggregates of quartz grains. XPL. h) Section of a subhedral, fractured garnet crystal within a calcite host. PPL. i) Euhedral moncheite inclusion in contact with a bornite dissemination within a quartz and epidote host. j) Native silver concentrated along a boundary between silicates and bornite. k) Euhedral inclusion of sperrylite within a bornite and silicate host. l) Subhedral inclusions of parkerite in a dissemination of bornite within a silicate host. The left grain of parkerite contains an inclusion of froodite that is not visible at this brightness scale. m) Euhedral bismuth-bearing millerite inclusion situated along a boundary between silicates and bornite. n) Anhedral inclusion of insizwaite in a silicate host. o) Wittichenite inclusions in a bornite, chalcopyrite and silicate assemblage. The wittichenite grains each contain several inclusions of silicate minerals. p) Euhedral bismuth-bearing millerite crystal that has hessite aggregates along its grain boundary. Chalcopyrite and epidote comprise the host assemblage.

Table 2.2: Characterization of the discrete, heavy metal-bearing mineral phases analyzed within 26 samples of "high sulfide" mineralization.

Mineral	# of samples	Total # grains	Avg. vol% in sample	Avg. grain size μm^2	Host breakdown	Textural comments
Hessite	26/26	579	2.56×10^{-3}	828	61% Ccp, 12% Pn, 9% Mil, 8% Bn, 7% Sil, 1% Sph, 1% Ccp+Sil, 1% Mon	anhedral inclusions commonly (37%) as composite grains with Mon; may also be intergrown with Meren, Mich, Gn, Fr, Kot or in contact with Sil, Sph, Gn, Mt, Mon, Mich, Cst, Pao
Moncheite	26/26	350	1.64×10^{-3}	935	59% Ccp, 18% Pn, 16% Sil, 3% Mil, 2% Ccp+Sil, 1% Bn, 1% Sph	anhedral inclusions most commonly (59%) as composite grains with Hess; may also be intergrown with Gn, Fr, Spy or in contact with Sil, Mt, Prt
Galena	25/26	5973	3.00×10^{-2}	1013	79% Ccp, 10% Pn, 7% Sil, 2% Sph, 1% Mil, 1% Mt	anhedral inclusions; sometimes in contact with Sil, Mt, Sph, Bn, Cst, Geff, Hess, Cott, Mich, El, Aca or intergrown with Hess, Mon, Naum, Cott, Geff, Aca or filling BMS voids/hosting Mt, Sil
Cassiterite	24/26	972	7.05×10^{-3}	1358	69% Ccp, 11% Sil, 9% Pn, 5% Sph, 2% Crn, 2% Ccp+Sph, 1% Mil, 1% Mt	euhedral (common) and anhedral (less common) inclusions; often occur in clusters and sometimes in contact with Sph, Mt, Sil, Gn, Hess, Cott or situated within cavities in BMS
Michenerite	18/26	134	1.29×10^{-3}	1195	63% Ccp, 24% Pn, 11% Mil, 1% Hess, 1% Sil	anhedral inclusions; sometimes in contact with Mil, Sil, Gn, Mt, Mon or intergrown with Hess, Fr, Prk
Native silver	17/26	86	4.27×10^{-3}	6313	66% Ccp, 13% Pn, 13% Ccp+Pn, 6% Sil, 1% Mil, 1% Sph	very fine coating on base metal sulfides; sometimes in contact with Sil, Gn, Mt, Cott or occupying cracks/cavities in BMS
Cotunnite	15/26	270	8.70×10^{-4}	371	78% Ccp, 12% Pn, 4% Mil, 4% Sil, 1% Sph, 1% Pn+Sph	anhedral inclusions most commonly occupying cracks in BMS; also sometimes in contact with Mt, Sil, Gn, Cst, Aca, Kur or intergrown with Gn
Acanthite	9/26	20	4.13×10^{-4}	1479	70% Pn, 20% Ccp, 5% Sil, 5% Ccp+Pn	anhedral inclusions commonly forming trails that occupy cracks in Pn; sometimes in contact with Sil, Mt, Sph, Gn, Cott, Ag or intergrown with Gn
Froodite	8/26	53	1.51×10^{-4}	160	74% Pn, 15% Ccp, 9% Mil, 2% Sph	anhedral inclusions; sometimes intergrown with Mon, Hess, Mich, El, Prk or in contact with
Electrum	8/26	30	1.15×10^{-3}	1874	53% Pn, 17% Ccp, 10% Sph, 10% Ccp+Sph, 7% Mil, 3% Sil	anhedral inclusions; sometimes in contact with Sil, Mt, Gn, Kot or intergrown with Fr, Spy
Geffroyite	7/26	32	2.21×10^{-4}	343	38% Ccp, 25% Pn, 25% Mil, 9% Sph, 3% Ccp+Pn	anhedral inclusions; sometimes in contact with Sil, Gn, Mt or intergrown with Gn and occupying cracks in Mil
Kotulskite	7/26	30	3.88×10^{-5}	67	61% Mil, 13% Sil, 10% Ccp, 7% Pn, 3% Ccp+Mil+Sil, 3% Hess, 3% Mil+Hess	anhedral inclusions; sometimes intergrown with Mon, Hess or in contact with Mil, Sil, El
Merenskyite	6/26	29	3.65×10^{-4}	474	39% Ccp, 34% Pn, 21% Sil, 3% Mil, 3% Ccp+Sil	anhedral inclusions sometimes in contact with Sil or forming composite grains with Hess
Sperrylite	6/26	19	1.51×10^{-5}	41	47% Bn, 32% Pn, 21% Ccp	subhedral and anhedral inclusions; sometimes intergrown with Mon, El or in contact with Sil
Paolovite	2/26	44	1.70×10^{-4}	55	48% Pn, 27% Mil, 16% Ccp, 9% Ccp+Pn	anhedral inclusions; intermittently in contact with Sil, Mt, Hess
Naumannite	2/26	14	1.53×10^{-5}	20	43% Ccp, 22% Bn, 21% Ccp+Bn, 7% Mil, 7% Sil	anhedral inclusions that are sometimes intergrown with Gn
Parkerite	2/26	4	8.54×10^{-6}	30	50% Pn, 50% Mil	anhedral inclusions that are in contact with Fr or intergrown with Mich, Fr
Sobolevskite	2/26	3	1.23×10^{-6}	4	67% Mil, 33% Pn	isolated anhedral inclusions
Chlorargyrite	1/26	4	1.38×10^{-3}	3054	100% Ccp	isolated anhedral inclusions
Hawleyite	1/26	3	1.15×10^{-5}	21	100% Sil	anhedral inclusions; sometimes in contact with Sph
Niggliite	1/26	3	9.02×10^{-6}	21	100% Pn	anhedral inclusions occupying cracks in Pn
Barite	1/26	2	9.24×10^{-5}	365	100% Ccp	anhedral inclusions in contact with Sil
Kurilite	1/26	2	4.91×10^{-6}	17	100% Ccp	anhedral inclusions; sometimes in contact with Cott
Unnamed Pd-Pt-Bi-Te mineral	1/26	1	3.25×10^{-3}	24539	100% Ccp	individual anhedral inclusion in contact with Mt
Molybdenite	1/26	1	4.54×10^{-4}	3884	100% Ccp	isolated anhedral inclusion
Zincite	1/26	1	6.80×10^{-5}	539	100% Ccp	isolated anhedral inclusion
Bismite	1/26	1	3.51×10^{-5}	245	100% Pn	isolated anhedral inclusion
Paratellurite	1/26	1	9.84×10^{-6}	79	100% Ccp	individual anhedral inclusion in contact with Mon
Menshikovite	1/26	1	3.00×10^{-6}	21	100% Ccp	isolated anhedral inclusion
Naumannite	1/26	1	2.67×10^{-6}	11	100% Sil	isolated anhedral inclusion
Clausthalite	1/26	1	2.07×10^{-6}	9	100% Sil	isolated anhedral inclusion

Table 2.3: Characterization of the discrete, heavy metal-bearing mineral phases analyzed within 12 samples of "low sulfide" mineralization.

Mineral	# of samples	Total # grains	Avg. vol% in sample	Avg. grain size μm^2	Host breakdown	Textural comments
Galena	11/12	3098	$4.06*10^{-2}$	781	87% Sil, 11% Ccp, 1% Bn, 1% Ccp+Sil	mainly clusters of anhedral inclusions; sometimes in contact with Ccp, Bn, Mil, Sil, Sph, Hess, Meren, Prk, Bis or intergrown with Hess, Bis, Mon, Insiz, UN Pd-Pt-Bi-Te mineral, Prk
Hessite	9/12	63	$1.94*10^{-4}$	168	68% Sil, 13% Bn, 13% Ccp, 2% Cal, 2% Ccp+Sil, 1% Witt, 1% Brt	anhedral inclusions; sometimes intergrown with Mon (11%), Mil, Gn, Mich, UN Pd-Pt-Bi-Te mineral, Kot, Witt, Bis, Cre or in contact with Ccp, Bn, Sil, Gn, Mon, Kot
Moncheite	8/12	73	$1.38*10^{-3}$	1059	72% Sil, 15% Ccp, 12% Ccp+Sil, 1% Bn	euhedral, subhedral and anhedral inclusions; sometimes intergrown with Hess (10%) or intergrown with Gn, Kot, Insiz or in contact with Ccp, Bn, Sil, Gn, Hess
Parkerite	8/12	72	$6.86*10^{-4}$	433	54% Sil, 29% Bn, 8% Bn+Sil, 3% Ccp, 3% Mil, 3% Ccp+Sil	anhedral (most common), subhedral and euhedral inclusions; sometimes in contact with Ccp, Bn, Gn, Sil or intergrown with Gn, Fr or containing Sil inclusions
Native silver	6/12	53	$9.03*10^{-4}$	516	64% Sil, 23% Bn, 11% Ccp, 2% Bn+Sil	anhedral inclusions (much thicker than Ag in HS samples); sometimes in contact with Bn, Ccp or intergrown with/lining edges of Ccp
Bismite	6/12	92	$5.56*10^{-4}$	212	53% Sil, 37% Ccp, 5% Ccp+Sil, 2% Bn, 2% Ccp+Bn, 1% Hess	anhedral inclusions most commonly intergrown with Gn (83%); sometimes intergrown with Hess or in contact with Ccp, Bn, Sil, Aca, Cre
Froodite	6/12	9	$1.72*10^{-5}$	68	56% Sil, 11% Ccp, 11% Witt, 11% Prk, 11% Ccp+Cal	anhedral inclusions; sometimes in contact with Ccp, Sil, UN Pd-Pt-Bi-Te mineral, Gn or intergrown with Mil (Bi-bearing)
Electrum	5/12	8	$9.17*10^{-5}$	282	63% Sil, 25% Ccp, 12% Bn	anhedral inclusions; sometimes in contact with Ccp, Sil or intergrown with Tsu or in cavities
Sperrylite	3/12	5	$3.68*10^{-4}$	1190	60% Sil, 20% Bn+Sil, 20% Hess	euhedral, subhedral and anhedral (most common) inclusions; sometimes in contact with Ccp
Kotulskite	3/12	3	$3.52*10^{-4}$	3037	67% Sil, 33% Ccp	anhedral inclusions in contact with Hess or intergrown with Mon, Hess
Wittichenite	2/12	75	$3.92*10^{-3}$	665	74% Bn, 17% Sil, 4% Bn+Sil, 3% Mil, 1% Bn+Mil, 1% Bn+Mil+Sil	anhedral inclusions; sometimes in contact with Ccp, Bn, Mil, Sil or intergrown with Hess or containing Sil, Mil, Fr inclusions
Acanthite	2/12	21	$1.34*10^{-4}$	126	57% Sil, 43% Ccp	anhedral inclusions; sometimes in contact with Bn, Gn, Bis or intergrown with Ccp
Aikinite	2/12	19	$1.71*10^{-3}$	1051	100% Sil	mainly isolated anhedral inclusions; one grain intergrown with Ccp
Michenerite	1/12	11	$3.16*10^{-4}$	249	82% Sil, 18% Ccp	anhedral (common) and euhedral (less common) inclusions; sometimes intergrown with Hess or in contact with Ccp, Bn
Merenskyite	2/12	11	$5.60*10^{-4}$	596	100% Sil	anhedral inclusions; sometimes intergrown with Hess or in contact with Ccp, Sil, Gn
Tsumoite	2/12	3	$1.77*10^{-6}$	7	100% Sil	anhedral inclusions; sometimes intergrown with El
Insizwaite	2/12	2	$1.27*10^{-5}$	110	100% Sil	anhedral inclusions; sometimes intergrown with Gn, Mon
Sobolevskite	2/12	2	$8.30*10^{-6}$	57	50% Bn, 50% Sil	isolated anhedral inclusions
Barite	1/12	48	$6.83*10^{-3}$	830	79% Sil, 21% Ccp	anhedral (most common), subhedral and euhedral inclusions; sometimes in contact with Ccp, Sil or containing inclusions of Ccp, Sil
Crerarite	1/12	17	$5.49*10^{-4}$	280	88% Sil, 6% Ccp, 6% Ccp+Ap	mostly isolated anhedral inclusions; sometimes in contact with Bis or intergrown with Hess
Naumannite	1/12	13	$2.79*10^{-5}$	21	46% Ccp, 23% Bn, 23% Ccp+Bn, 8% Mil	anhedral inclusions most commonly intergrown with Gn (92%); sometimes in contact with Bn, Mil, Sil
Cassiterite	1/12	8	$5.34*10^{-4}$	631	100% Rt	isolated anhedral inclusions
Unnamed Pd-Pt-Bi-Te mineral	1/12	6	$1.82*10^{-2}$	26234	33% Sil, 33% Ccp+Cal, 17% Ccp, 17% Ccp+Sil	anhedral inclusions; sometimes containing inclusions of Sil, intergrown with Gn or filling interstices between Sil
Bismuthiferous galena	1/12	2	$4.55*10^{-5}$	117	100% Sil	anhedral inclusions; sometimes intergrown with Mon
Native zinc	1/12	1	$7.25*10^{-4}$	6852	100% Cal	isolated anhedral inclusion
Chlorargyrite	1/12	1	$1.09*10^{-4}$	586	100% Sil	isolated anhedral inclusion
Cotunnite	1/12	1	$4.04*10^{-5}$	235	100% Sil	isolated anhedral inclusion
Bismuthian palladian melonite	1/12	1	$3.54*10^{-5}$	207	100% Sil	isolated anhedral inclusion
Maslovite	1/12	1	$2.12*10^{-5}$	184	100% Sil	isolated anhedral inclusion
As-bearing argentocuprocosalite	1/12	1	$1.43*10^{-5}$	83	100% Sil	isolated anhedral inclusion
Tenorite	1/12	1	$9.97*10^{-6}$	94	100% Rt	isolated anhedral inclusion

Table 2.4: Alteration phases accompanying "high sulfide" and "low sulfide" (calcite-free) mineralization styles. Y = yes, N = no, B = both primary and secondary (alteration-associated) phase. Ranges are reported for modal abundances and grain sizes.

Mineral	Alteration	Modal abundance (%)	Grain size (μm)	Identifying features, key textures, relationships
High sulfide n = 10				
Quartz	B	1.3 - 63.3	2 - 1700	aggregates of equigranular grains (largest grains in samples; clearly not primary) fine-grained crystals associated with Kfs+Pl (± secondary Chl, Act) in relict granitoid/gneissic blocks inequigranular rounded crystals intergrown with Chl & Act; this assemblage comprises a large fraction of some samples some grains display moderate to high undulatory extinction (strain history)
Chlorite	Y	6.0 - 71.2	1 - 950	distinct continuous trails of massive foliated crystals that separate relict granitoid/gneissic blocks ubiquitous platy crystals (± Act) throughout sections of relict granitoid/gneissic blocks clots of platy crystals that contain ubiquitous Ttn inclusions and are spatially associated with Ep and disseminated Ccp often partially to completely replacing Hbl
Epidote	Y	0.01 - 5.7	3 - 525	localized clusters of anhedral aggregates spatially associated with disseminated Ccp continuous networks of fine-grained aggregates; isolated anhedral aggregates
Titanite	Y	0.07 - 1.4	1 - 80	brown-colored, wedge-shaped to somewhat rounded inclusions in massive Chl patches
Hornblende	N	0.008 - 18.4	1 - 35	remnants of medium brown-colored grains that are partially to completely replaced by Chl
Actinolite	Y	0.06 - 0.2	2 - 775	clusters of relatively coarse-grained euhedral bladed crystals associated with Ep and Ccp disseminations fine-grained crystals that form intergrowths with Qtz+Chl
Apatite	Y	0.0001 - 0.1	10 - 400	colorless grains with hexagonal outlines contained in secondary Qtz+Chl+Act assemblages (contain Ccp inclusions)
Biotite	N	0.003 - 0.09	7 - 190	light brown-colored grains partially replaced by Chl in areas (in contact with Ccp disseminations around these areas) sometimes wedged between/in contact with Stp flakes
Stilpnomelane	Y	6.8	12 - 1125	randomly distributed brown- to orange-colored flakes often in contact with massive Chl or Bt
Low sulfide (calcite-free) n=2				
Quartz	B	66.9 - 69.0	3 - 1625	relatively large equigranular clusters and trails of (secondary) rounded inclusions fine-grained crystals associated with Kfs+Pl in relict granitoid/gneissic blocks
Epidote	Y	0.5 - 1.0	1 - 425	granular aggregates that host, or are spatially associated with sulfide disseminations
Chlorite	Y	2.4 - 8.3	1 - 1000	large masses of foliated crystals that commonly host Ccp disseminations and partially to completely replace Hbl, Aug
Actinolite	Y	0.7	9 - 500	aggregates of euhedral bladed crystals that align relatively coarse-grained Qtz trails
Hornblende	N	0.02 - 0.3	1 - 400	chestnut brown-colored masses of crystals that are partially to completely replaced by Chl
Titanite	Y	0.004 - 0.2	1 - 35	brown-colored, wedge-shaped to somewhat rounded inclusions in Chl
Apatite	Y	0.04	35 - 425	localized colorless grains with disinct hexagonal outlines
K-feldspar	N	11.8 - 15.4	8 - 275	fine-grained crystals associated with Qtz+Pl in relict granitoid/gneissic blocks
Plagioclase	N	7.8 - 12.3	7 - 275	fine-grained crystals associated with Qtz+Kfs in relict granitoid/gneissic blocks
Augite	N	0.1 - 1.6	6 - 875	anhedral inclusions partially to completely replaced by Chl from their rims inward

Table 2.5: Alteration phases accompanying "low sulfide" (calcite-bearing, garnet-bearing) mineralization. Y = yes, N = no, B = both primary and secondary (alteration-associated) phase. Ranges are reported for modal abundances and grain sizes.

Mineral	Alteration	Modal abundance (%)	Grain size (µm)	Identifying features, key textures, relationships
Low sulfide (calcite-bearing) n=2				
Quartz	B	19.5 - 83.5	2 - 1950	aggregates of relatively coarse-grained, rounded crystals that are associated with Ep, Chl
				fine-grained crystals associated with Kfs+Pl in relict granitoid/gneissic blocks
				some grains display moderate to high undulatory extinction (strain history)
Epidote	Y	3.5 - 7.5	1 - 900	inequigranular patches of anhedral inlcusions that show a strong spatial association with sulfides
				very fine-grained networks of grains (with Chl); elongate grains associated with stretched Qtz grains
Calcite	Y	0.01 - 0.09	3 - 375	localized anhedral inclusions that fill interstices between (secondary) Qtz aggregates; often associated with Bn
Chlorite	Y	2.8 - 71.5	1 - 800	large masses of foliated crystals spatially associated with Ep, sulfides
				localized platy crystals filling interstices between quartz aggregates; very fine-grained networks of grains (with Ep)
Titanite	Y	0.02 - 0.3	1 - 90	brown-colored, wedge-shaped to somewhat rounded equigranular inclusions in Chl
Na-Cl silicate	Y	0.02	30 - 225	localized subhhedral to anhedral, light pink-colored, isotropic inclusions that occur within Ep clusters and Chl masses
K-feldspar	N	1.8	6 - 100	fine-grained crystals associated with Qtz+Pl in relict granitoid/gneissic blocks
Plagioclase	N	1.6	5 - 90	fine-grained crystals associated with Qtz+Kfs in relict granitoid/gneissic blocks
Low sulfide (garnet-bearing) n=1				
Quartz	B	2.4	5 - 950	randomly distributed grains that fill in voids between larger Cal grains
Epidote	Y	5.2	1 - 325	granular aggregates within Cal; often in contact with Grt or Act
Chlorite	Y	6.0	1 - 700	foliated masses occupying interstices between Cal grains
Calcite	Y	79.3	15 - 3800	coarse-grained aggregates that comprise the overall matrix (along with subordinate Qtz) to the sample
Garnet	Y	6.2	10 - 3500	euhedral, variably fractured inclusions in Cal+Qtz; often in contact with Ep, calcic amphibole, sulfides
Actinolite	Y	0.6	5 - 275	randomly distributed needle-shaped crystals in calcite that are commonly in contact with Ep
Calcic amphibole	Y	0.1	8 - 525	packages of Cal-hosted fibrous crystals commonly in contact with Grt; SEM-EDS results show it is not Act or tremolite
Augite	N	0.1	15 - 175	localized xenocrystic inclusions in Cal
Rutile	Y	0.1	3 - 290	relatively fine-grained Cal-hosted inclusions that are commonly associated with discrete phases

2.5 Mineral and bulk rock chemistry

2.5.1 Trace metal characteristics

The trace metal variability, both within an ore body (153 vs. 170) and between mineralization-styles ("high sulfide" vs. "low sulfide") is compared for which mineral phases are the most relevant carriers of Ni, Pb, Pt, Pd, Ag, Au, and Sn. Other notable (semi-) quantitative mineralogical trace metal characteristics encountered are: the presence of Bi–bearing millerite (~7-9 at% Bi), galena often contains SEM-EDS-detectable Se (on the order of~1-5 at%), and all electrum is more Ag-rich (generally on the order of ~60-70 at% Ag and ~30-40 at% Au). Selenium-bearing galena and Ag-rich electrum have each been reported in several mineralogical studies within footwall environments along the North Range (i.e. Springer 1989; Jago et al. 1994; Farrow and Watkinson, 1997; Ames et al. 2007; Dare et al. 2011; Dare et al. 2014 etc.); however, to the author's knowledge, this is the first time Bi-bearing millerite has been reported at Sudbury. Laser ablation – inductively coupled plasma mass spectrometry (LA-ICPMS) analyses for all samples analyzed are reported in Table 2.6. All michenerite analyzed contained very low Pt concentrations and thus a value of 1.0 at% (1.3 wt%) was assumed during the mass balance calculations.

2.5.1.1 "High sulfide" sharp-walled vein mineralization

Mass balances for Ni are accounted for nearly entirely by the BMS pentlandite and millerite in sharp-walled veins from both orebodies. Millerite covers the entire

Ni budget for the single high sulfide sample from the "bornite group" in the 153 ore body. Lead is accounted for by galena and solid solution among the base metal sulfides chalcopyrite (12.1 ppm), pentlandite (4.61 ppm), and millerite (0.62 ppm) in veins from the 153 ore body and by galena, chalcopyrite (13.1 ppm Pb), and pentlandite (5.71 ppm Pb) in veins from the 170 ore body. Lead in the "bornite group" was concentrated in galena, bornite (5.19 ppm Pb), and chalcopyrite (9.63 ppm Pb). Platinum is nearly entirely locked up in PGM and the contribution from BMS to the platinum budget is usually negligible. Mass balances for Pt from sharp-walled veins from the 153 ore body are covered by moncheite, michenerite, merenskyite, nigglite, and a small contribution from millerite (0.0086 ppm Pt); whereas veins from the 170 ore body distribute their Pt among moncheite, michenerite, merenskyite, and sperrylite. Moncheite and sperrylite are the sole contributors to the Pt mass balance for the "bornite group" sample. Palladium was distributed among several PGM within sharp-walled veins from the 153 ore body: kotulskite, froodite, paolovite, merenskyite, michenerite, and moncheite. Pentlandite (1.53 ppm Pd) accounted for part of the Pd mass balance for the sharp-walled veins from the 153 ore body veins as well. Palladium mass balances for veins from the 170 ore body were accounted for by michenerite, merenskyite, kotulskite, moncheite, and pentlandite (10.9 ppm Pd). The Pd mass balance for the single sample from the "bornite group" was virtually entirely covered by moncheite. Silver within veins from the 153 ore body is locked up in hessite, electrum, pentlandite (21.7 ppm Ag), chalcopyrite (39.4 ppm Ag), and millerite (2.19 ppm Ag).

Table 2.6: LA-ICPMS analyses of base metal sulfides and magnetite in selected samples of "high sulfide" and "low sulfide" mineralization. Each row is based on averaging 3-5 analyses on that mineral. See digital appendix for supplementary data.

Sample	Style	Phase	29Si	34S	42Ca	51V	53Cr	57Fe	59Co	60Ni	62Zn	65Cu	75As	77Se	88Sr	89Y	91Zr	101Ru	103Rh	105Pd	107Ag	108Pd	109Ag	111Cd	118Sn	121Sb	125Te	181Ta	185Re	189Os	193Ir	195Pt	197Au	205Tl	206Pb	208Pb	209Bi
MM11A	HS	Cpp	46.3	393205	2.73	0.013	0.44	304317	0.19	112	276	326632		0.043																							
MM11A	HS	Pn	94.4	419868	4.82	0.012	0.53	325538	4996	533295																											
MM11A	HS	Mt	238	341	BDL	4.38	3.92	723599	9.83	2582																											
MM12A	HS	Cpp	49.3	405868	7.35	0.014	3.06	304317	0.68	89.8																											
MM12A	HS	Mt	47.7	441338	190	0.22	0.39	325538	8795	505297																											
MM12A	HS	Mt	591	349	2.74	12.3	4.16	723599	17.3	2885																											
MM13A	HS	Cpp	50.2	402045	BDL	0.0082	0.34	304317	0.35	84.37																											
MM13A	HS	Mt	129	406554	97.0	0.049	0.71	325538	9214	481313																											
MM13A	HS	Mt	245	617	52.4	9.53	7.51	723599	8.94	2505																											
MM14A	HS	Mt	781	391888	7.35	0.019	0.40	304317	0.40	109																											
MM14A	HS	Mt	442	571	11.7	12.2	6.98	325538	17.2	814																											
MM14A	HS	Pn	417	396261	4.83	0.012	0.29	304317	6425	950																											
MM15A	HS	Mt	49.0	422433	21.3	9.44	4.66	723599	15.2	2889																											
MM15A	HS	Pn	489	275	6.58	0.022	0.65	325538	1.12	124																											
MM16A	HS	Mt	55.6	412034	8.34	0.010	1.08	304317	2.65	218																											
MM16A	HS	Pn	609	680	5.55	3.06	9.63	723599	33722	445453																											
MM16A	HS	Cpp	62.9	415522	16.1	0.0	9.63	304317	253	16065																											
MM17A	HS	Mt	112	410912	10.0	22.3	0.26	325538	5498	476874																											
MM17A	HS	Pn	671	810	111	0.014	0.40	304317	30.9	3219																											
MM18A	HS	Mt	36.7	401538	40.7	0.019	0.23	325538	0.069	109																											
MM18A	HS	Pn	65.0	426204	3.20	16.7	0.040	723599	5317	519394																											
MM19A	HS	Mt	549	468	8.96	0.0091	0.51	304317	104	646750																											
MM19A	HS	Pn	46.7	384796	13.3	0.0084	0.10	8842	4891	987																											
MM19A	HS	Mt	83.4	539411	295	15.6	1.21	723599	7260	519238																											
MM20A	HS	Mt	54.0	417712	14.1	0.011	0.44	304317	5263	646750																											
MM20A	HS	Pn	50.5	4966	11.4	0.0099	0.53	325538	19.6	2830																											
MM20A	HS	Cpp	59.2	389873	22.9	0.030	0.11	9289	2541	107																											
MM20A	HS	Mll	144	375254	13.0	18.0	7.08	723599	1821	2707																											
MM32	HS	Mt	488	401943	25.4	0.016	0.38	304317	0.49	214																											
MM32	HS	Mll	173	373	5.71	0.039	0.25	325538	5.52	584009																											
MM32	HS	Mll	72.4	426478	6.69	234	0.33	723599	16.5	22.1																											
92	HS	Mll	93.5	401031	13.0	0.012	0.46	11835	75.8	4125																											
92	HS	Mll	86.6	406533	10.9	0.012	0.23	304317	2287	343443																											
92	HS	Pn	55.3	422417	0.48	0.015	0.39	325538	5199	229																											
92	HS	Mll	628	380741	4.32	33.9	3.31	6568	10.2	2898																											
MM1T	HS	Mt	48.6	600	BDL	0.021	0.40	304317	0.085	0.33																											
MM1T	HS	Pn	67.5		11.9	0.046	0.29	116519	0.021	4.90																											
MM1T	HS	Cpp	53.6	414563	16.9	0.017	0.12	544	5315	646750																											
MM2T	HS	Mll	158	373	0.51	0.034	0.64	304317	0.12	52.2																											
MM2T	HS	Mll	137	387227	3.19	0.019	0.33	0.18	3511	646750																											
MM2T	HS	Cpp	564	13356	24.1	7.47	12.8	116519	16.5	2707																											
MM3U	HS	Mll	100	405980	12.9	0.012	0.28	304317	0.11	32.2																											
MM3U	HS	Mll	145	410153	1.72	0.068	0.42	304317	0.054	4122																											
MM3U	HS	Pn	900	420801	12.1	0.057	0.49	325538	19.9	10.5																											
MM5	HS	Cpp	66.3	392319	12.4	103	2.39	304317	2.39	3.85																											
MM5	HS	Mll	123	463376	1567	0.034	4.90	116519	1985	30067																											
MM5	HS	Mll	680	380924	313	83.1	3.96	723599	13.3	3150																											
MM5	HS	Cpp	68.1	574	64.1	0.016	0.34	0.097	0.16	2.15																											
MM8	HS	Mll	198	410439	193	7.47	12.8	116519	0.062	42.2																											
MM8	HS	Mll	154	266320	6169	346	0.71	304317	3893	650396																											
MM9(3)	HS	Mll	1748	627	12.1	0.068	0.82	304317	0.031	4098																											
MM9(3)	HS	Bn	89.9	384000	12.1	0.013	0.37	304317	0.053	12.2																											
MM9(3)	HS	Cpp	1189	240404	94.3	3.15	3.51	116519	5.52	54.9																											
MM5s	HS	Mll	94.8	382801	20.8	0.034	3.20	0.097	0.53	45.4																											
MM5s	HS	Mll	169	420801	12.1	0.023	0.36	304317	6028	646750																											
MM6S	HS	Mll	160	384797	15.1	1.77	1.90	304317	0.10	0.28																											
MM6S	HS	Bn	422	293917	173	3.57	1.90	116519	0.54	131																											
MM70	HS	Mll	160	358177	120	0.057	0.20	1217	0.62	4.87																											
MM70	HS	Cpp	214	283159	3.80	0.010	0.55	304317	0.63	5.86																											
MM70	HS	Bn	164	427190	6.39	0.090	0.42	304317	7528	646750																											
MM94	HS	Mll	121	304803	221	0.027	0.42	116519	0.71	25.1																											
MM94	HS	Mll	6868	413999	0.39	3.45	1.67	1516	6848	646750																											
MM94	LS	Cpp	165	303239	2775																																
9SA	LS	Bn	3981	303239																																	
9SA	LS	Mll	166	378369																																	

50

Veins from the 170 ore body distribute their Ag mass balance between hessite, native silver, geffroyite, and chalcopyrite (16.1 ppm Ag). Even though the sample from the "bornite group" contained several Ag-phases (hessite, native silver, naumannite), the Ag mass balance for this sample was covered almost exclusively by bornite (1120 ppm Ag); with small contributions from hessite and chalcopyrite (26.2 ppm Ag). Gold mass balances were divided nearly evenly between electrum and chalcopyrite (0.40 ppm Au) within vein samples from the 153 ore body; with small contributions from pentlandite (0.24 ppm Au) and magnetite (0.038 ppm Au). Chalcopyrite (0.28 ppm Au) was almost the sole contributor to the Au mass balance for 170 vein samples; with small contributions from pentlandite (0.0042 ppm Au) and millerite (0.0064 ppm Au). The Au mass balance for the sample from the "bornite group" was dominated by bornite (0.0018 ppm Au); with chalcopyrite (0.0013 ppm Au) and millerite (0.00083 ppm Au) filling out the mass balance. It is likely that the dominance of BMS to these mass balances is a function of the "nugget effect," where electrum is distributed heterogeneously among the veins at the scale of individual thin sections. Tin budgets for veins from the 153 ore body are divided among paolovite, cassiterite, niggliite, magnetite (226 ppm Sn), and chalcopyrite (14.2 ppm Sn). Millerite (0.18 ppm Sn) and pentlandite (0.11 ppm Sn) contribute small fractions to the Sn mass balances for veins from the 153 ore body as well. Veins from the 170 ore body attribute the majority of their Sn mass balance to cassiterite; with subordinate contributions from chalcopyrite (22.5 ppm Sn) and magnetite (184 ppm Sn). The "bornite group" sample owes nearly its entire Sn mass balance to chalcopyrite (5.77 ppm Sn); with a small contribution from bornite

(0.071 ppm Sn). Stacked column charts for high sulfide mass balances from both ore bodies are illustrated in Figure 2.6 a, b, c.

2.5.1.2 "Low sulfide" PGE-rich mineralization

All low sulfide samples that are discussed in this section were sampled from the 170 ore body. Nickel mass balances are distributed fairly evenly among pakerite, millerite, and chalcopyrite (90.6 ppm Ni) for the low sulfide samples. Lead is accounted for ~100% by galena in low sulfide mineralization. The Pt mass balances in low sulfide mineralization were distributed among several PGM: moncheite, sperrylite, insizwaite, maslovite, crerarite, and an unnamed $(Pd,Pt)(Bi,Te)_2$ mineral; as well as small contributions from solid solution in millerite (0.54 ppm Pt) and chalcopyrite (0.012 ppm Pt). Palladium budgets in low sulfide samples were controlled by kotulskite, froodite, michenerite, an unnamed $(Pd,Pt)(Bi,Te)_2$ mineral, and moncheite; with small contributions from chalcopyrite (0.018 ppm Pd), millerite (0.10 ppm Pd), and bornite (0.15 ppm Pd). Silver in the low sulfide samples is controlled by hessite, native silver, electrum, bornite (562 ppm Ag), and chalcopyrite (10.3 ppm Ag). Gold is distributed among electrum, chalcopyrite (0.11 ppm Au), bornite (0.074 ppm Au), and millerite (0.071 ppm Au) in low sulfide mineralization. Tin is covered nearly entirely by solid solution in chalcopyrite (10.4 ppm Sn) in low sulfide samples; with minor contributions from bornite (17.3 ppm Sn) and millerite (1.78 ppm Sn). Stacked column charts for low sulfide mass balances are illustrated in Figure 2.6 d.
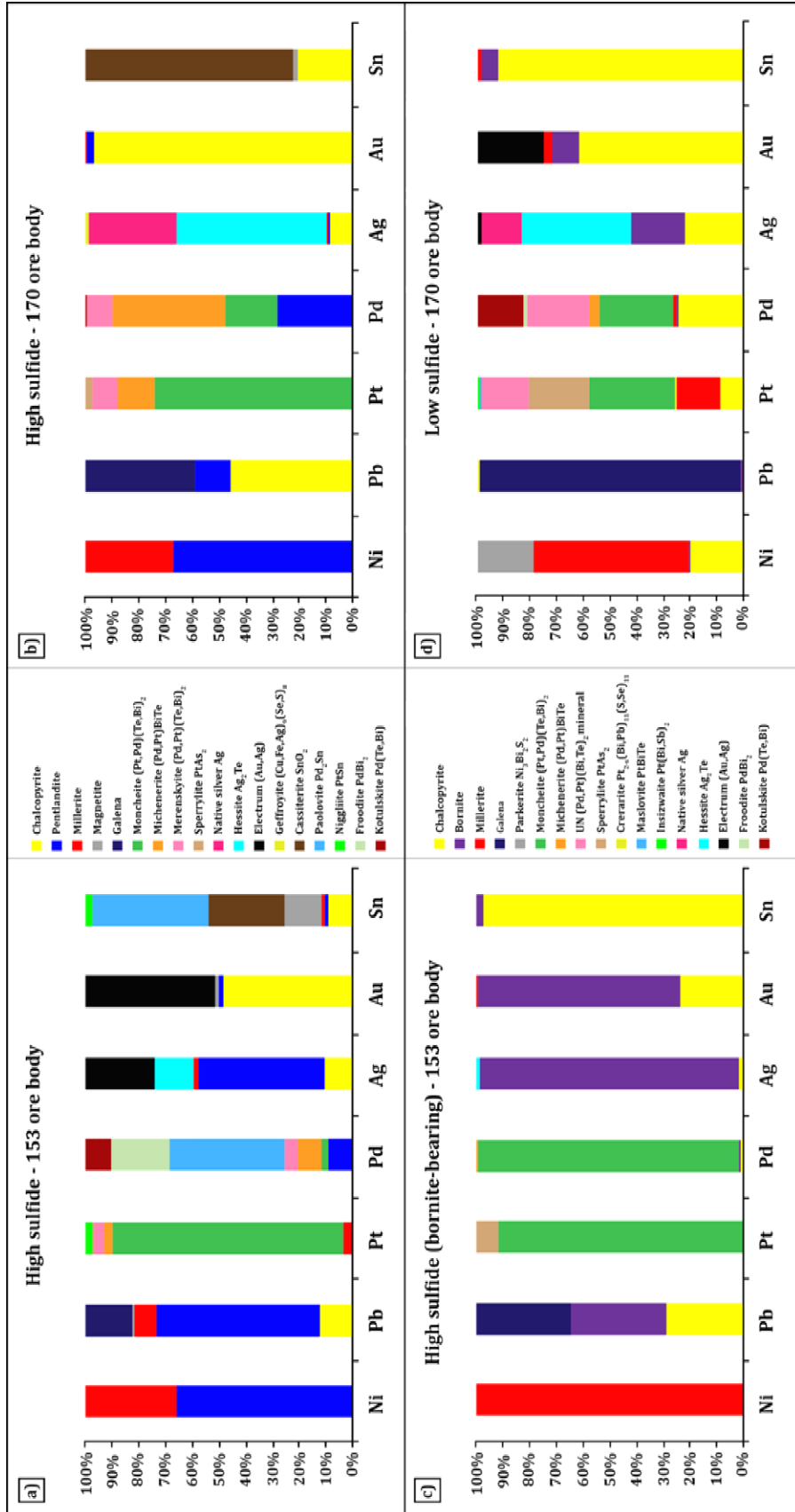
Figure 2.6 (previous page): Stacked column charts illustrating Ni, Pb, Pt, Pd, Ag, Au, and Sn mass balances for mineralized samples. See Table 2.6 for LA-ICPMS concentration values and digital appendix for mass balance calculator. a) High sulfide mineralization: 153 ore body (n = 2). b) High sulfide mineralization: 170 ore body (n = 2). c) High sulfide (bornite-bearing) mineralization: 153 ore body (n = 1). d) Low sulfide mineralization: 170 ore body (n=4).

2.5.2 Trace metal comparison between mutual sulfides in "high sulfide" and "low sulfide" mineralization

Differences in trace metal concentrations between minerals that are present in both high sulfide and low sulfide mineralization styles (chalcopyrite, millerite, bornite) are highlighted in Figure 2.7 a. Notable differences that pertain to each mineral are discussed below.

2.5.2.1 Chalcopyrite

Trace metal concentrations in high sulfide chalcopyrite vs. low sulfide chalcopyrite do not vary as much as the other BMS that are mutual to these two mineralization styles. The only metal to vary by >1 order of magnitude in its log(high sulfide chalcopyrite/low sulfide chalcopyrite) ratio is V. Vanadium is more concentrated in low sulfide chalcopyrite. Differences in the remaining 21 metals are illustrated in Figure 2.7 a.

2.5.2.2 Millerite

All trace metals analyzed have higher abundances in low sulfide millerite except for Pd and Te. Cadmium, Sn, Sb, Re, Pt, Tl, and Pb all vary by >1 order of magnitude in their log(high sulfide chalcopyrite/low sulfide chalcopyrite) ratios in favor of low sulfide millerite. Rhodium varies by >2 orders of magnitude in favor of low sulfide millerite.

2.5.2.3 Bornite

Like millerite, low sulfide bornite contains higher abundances for the majority of trace metals analyzed compared to its high sulfide counterpart. The only trace metals that are more abundant in high sulfide bornite are Rh and Ag. Chromium, Co, Zn, As, Pd, Ta, Os, Ir, Au, and Pb all vary by >1 order of magnitude in their log(high sulfide chalcopyrite/low sulfide chalcopyrite) ratios in favor of low sulfide mineralization. Vanadium, Sn, and Pt each vary by >2 orders of magnitude in favor of low sulfide bornite.

2.5.3 Trace metal comparison between chalcopyrite and bornite in "low sulfide" mineralization

Trace metal concentration comparisons between pairs of low sulfide chalcopyrite and low sulfide bornite that are in equilibrium together in single samples show that notable differences exist in the trace metal chemistry between these two Cu-BMS. These differences are highlighted in Figure 2.7 b. Nickel, Zn, and Sn are generally much more concentrated in chalcopyrite; while bornite contains higher concentrations for the majority of the remaining 21 metals plotted, with major (1-3 orders of magnitude) differences in log(high sulfide bornite/low sulfide bornite) ratios for the metals V, Ag, and Bi within most of the samples. Such different trace metal concentrations between chalcopyrite and bornite in the same samples preclude the formation of bornite by chalcopyrite replacement (this is supported by the equilibrium textural associations that were observed between these two phases under the microscope).
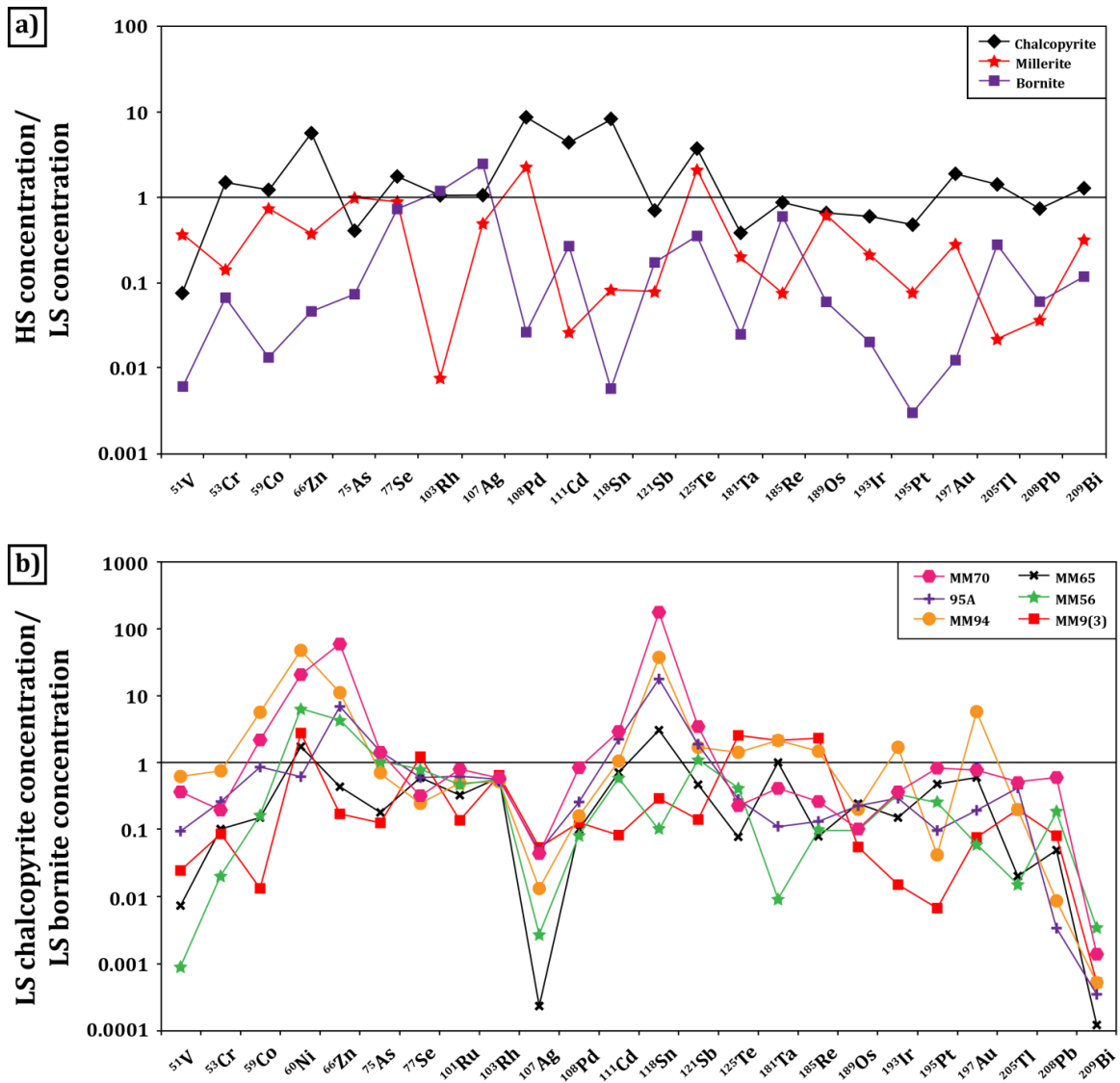
Figure 2.7: Trace metal variability in sulfides from Coleman ore samples. LA-ICPMS concentration values are listed in Table 2.6. a) Log graph of average high sulfide (HS)/low sulfide (LS) ratios for trace metal concentrations from the two sulfide phases present in both mineralization styles - chalcopyrite (HS: n = 15 samples; LS: n = 7 samples) and millerite (HS: n = 7 samples; LS: n = 6 samples). b) Log graph of chalcopyrite/bornite trace metal concentration ratios for 7 individual samples of low sulfide mineralization where chalcopyrite and bornite are in textural equilibrium.

2.5.4 Bulk rock comparison

High sulfide sharp-walled veins in both ore bodies are characterized by massive chalcopyrite with (generally) lesser and variable concentrations of pentlandite and millerite, and, as such, exhibit Cu grades between ~20 and 33 wt% and Ni grades between ~1 and 13 wt%. Bulk rock Ni correlates with the concentration of Ni-containing BMS in vein environments and this is confirmed through comparing petrographic analyses with bulk rock assays (Figure 2.9 a). High grade Ni samples (i.e. ~20 to 50 wt% Ni) can have Cu grades <5 wt% and are identified routinely by the presence of semi-massive to massive pentlandite and/or millerite. Iron grades remain fairly constant for all 8 veins; whereas there is a distinct negative correlation between grades for Cu and Ni which is manifested by the various proportions of chalcopyrite, pentlandite, and millerite throughout the veins. Figure 2.8 compares Cu, Ni, and Fe grades for 4 sharp-walled veins from the 153 ore body and 4 sharp-walled veins from the 170 ore body.

Silver is the most abundant precious metal in the sharp-walled veins within both ore bodies. It ranges from 29.7 g/t to 146 g/t within veins from the 153 ore body and from 120 g/t to 224 g/t within veins from the 170 ore body. There is no predictable relationship between bulk rock Pt and bulk rock Pd in the sharp-walled veins. Platinum is more abundant in some veins, whereas Pd is more abundant in others. In veins analyzed from the 153 ore body, 3/4 contain more Pd than Pt. Palladium ranges from 7.75 g/t to 14.0 g/t and Pt ranges from 1.97 g/t to 24.1 g/t in the 153 ore body veins. In veins analyzed from the 170 ore body, 2/4 contain more

Pd than Pt. Palladium ranges from 13.8 g/t to 34.2 g/t and Pt ranges from 5.45 g/t to 21.7 g/t in the 170 ore body veins. Gold grades are the lowest measured from the precious metals referred to herein. However, Au grades are systematically higher in sharp-walled veins from the 170 ore body when compared to those from the 153 ore body. Bulk rock Au ranges from 0.076 g/t to 0.58 g/t for veins from the 153 ore body and from 0.49 g/t to 1.57 g/t for veins from the 170 ore body.

Due to the low total sulfide mineral content of low sulfide mineralization (sulfide mineral concentrations <5 vol%), Cu, Ni, and Fe grades are substantially lower compared to veins and do not reach levels of economic interest for Sudbury footwall mineralization. The division of low sulfide mineralization into three separate alteration styles (calcite-free, calcite-bearing, garnet-bearing) allows Cu, Ni, and Fe grades to be compared among different low sulfide samples. Copper grades between ~0.5 and 3.3 wt% for all 3 low sulfide alteration styles; Fe grades between ~4.2 and 8.6 wt%; and Ni grades between ~0.04 and 0.4% (Figure 2.8). As a point of comparison, the hydrous alteration associated with sharp-walled veins is illustrated in Figure 2.8 as well. These uneconomic samples of vein alteration contain Ni and Fe grades that are similar to those measured in low sulfide samples and Cu grades that are 1 to 2 orders of magnitude lower than low sulfide samples.

Bulk rock Ag grades are fairly similar between the 3 alteration styles of low sulfide mineralization and range from 22.9 g/t to 50.3 g/t. However, marked differences exist for Pt, Pd, and Au between these alteration subgroups. Calcite-bearing alteration grades the highest Pt (17.0 g/t), followed by calcite-free
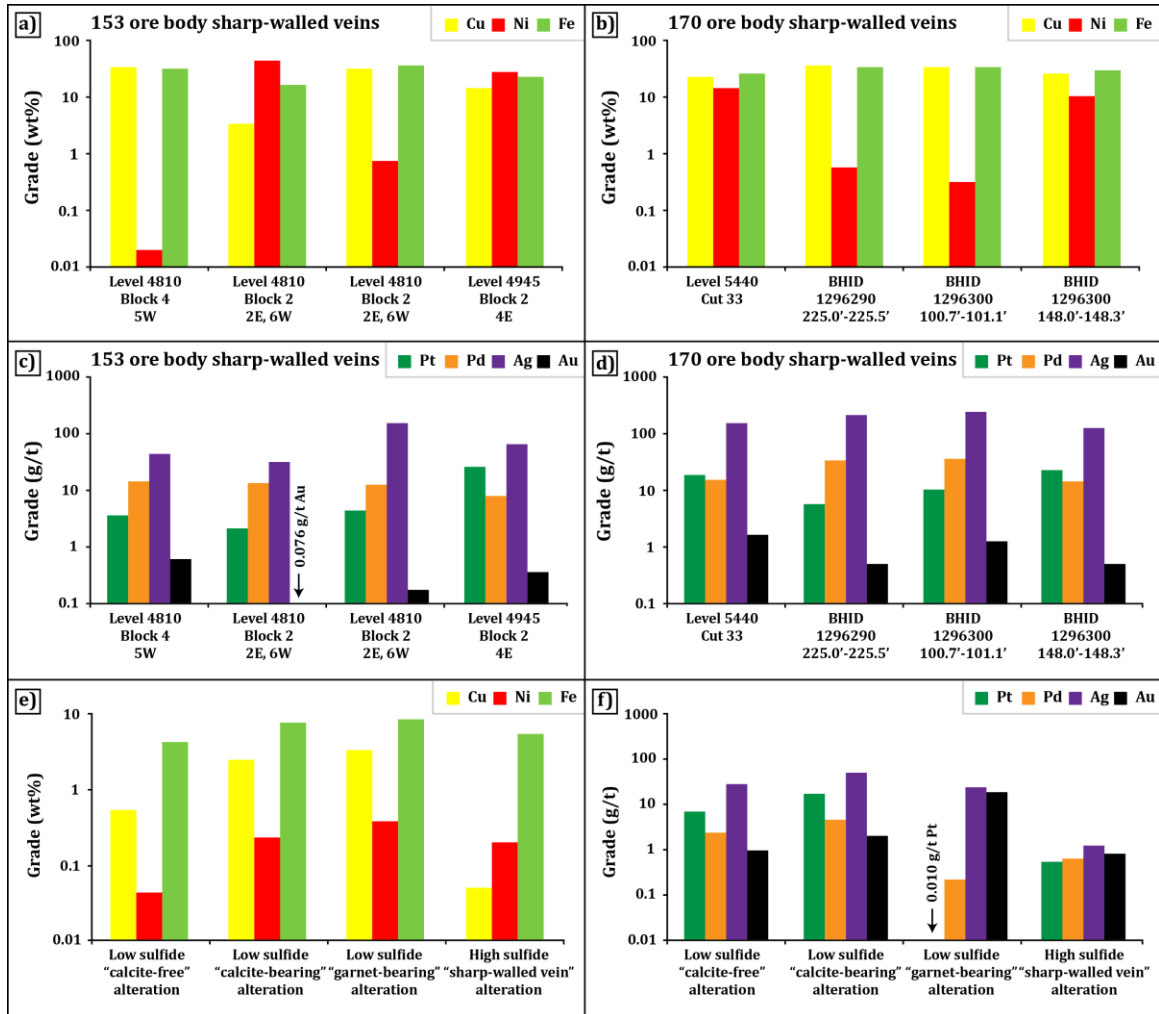
Figure 2.8: Variability in base/precious metal grades throughout the 153 and 170 ore bodies and as a function of alteration style. See digital appendix for supplementary data. a) Copper, Ni, and Fe grades (weight percent) for various sharp-walled veins sampled within the 153 ore body. b) Copper, Ni, and Fe grades (weight percent) for various sharp-walled veins sampled within the 170 ore body. c) Platinum, Pd, Ag, and Au grades (grams per ton) for various sharp-walled veins sampled within the 153 ore body. d) Platinum, Pd, Ag, and Au grades (grams per ton) for various sharp-walled veins sampled within the 170 ore body. e) Copper, Ni, and Fe grades (weight percent) for the different styles of hydrous alteration associated with low sulfide mineralization (calcite-free: n = 2, calcite-bearing: n = 2, garnet-bearing: n = 1) and for wallrock alteration present along the margins of sharp-walled veins (n = 3). f) Platinum, Pd, Ag, and Au grades (grams per ton) for the same samples displayed in (e).

alteration (6.67 g/t); with garnet-bearing alteration exhibiting much lower bulk rock Pt (0.01 g/t). A similar pattern is displayed for Pd, where calcite-bearing alteration contains Pd grades of 4.66 g/t, calcite-free alteration grades 2.40 g/t Pd, and garnet-bearing alteration contains bulk rock Pd values of 0.22 g/t. Gold exhibits the opposite pattern to Ag between the low sulfide alteration subgroups. Garnet-bearing alteration has the highest Au grades (18.7 g/t) whereas calcite-free alteration and calcite-bearing alteration have Au grades that are much lower, at 0.94 g/t and 2.03 g/t, respectively.

2.5.5 Individual sharp-walled vein study

Mineralogical and trace metal analyses carried out along "Vein 1" (Figure 2.2 b, c) allow variability at the scale of an individual stope to be addressed within sharp-walled vein environments. As discussed previously, sharp-walled veins are composed of massive chalcopyrite with variable concentrations of pentlandite and millerite. Using the sampling procedure outlined in Figure 2.2 c, it is shown that the absolute concentration of pentlandite+millerite exhibits an apparent decrease moving laterally along the core of the vein (furthest away from Sudbury Breccia contact) away from the SIC and deeper into the footwall (Figure 2.9 a); while no systematic lateral changes are apparent for samples taken along the vein margin (<20 cm for Sudbury Breccia contact). However, there is a drastic spike in the concentration of pentlandite+millerite for most samples collected along the vein margin compared to the vein core. This suggests that Ni-containing BMS are more

prevalent along vein margins and this observation is supported by higher average Ni grades along the margin (12.51 wt%) compared to the core (2.83 wt%).

The absolute concentration of Pt- and Pd-containing platinum group minerals that were analyzed along both the core and margin of "Vein 1" (moncheite, michenerite, merenskyite, sperrylite, kotulskite, froodite, menshikovite, unnamed $(Pd,Pt)(Bi,Te)_2$ mineral) display no apparent systematic changes both laterally and with proximity to Sudbury Breccia (Figure 2.9 b). Approximately equal Pt+Pd grades for the vein margin (43.37 g/t) and vein core (45.45 g/t) support this observation and it is therefore implied that the section sampled along the width of veins within sharp-walled environments has no bearing on overall PGE (Pt, Pd) grades.

Likewise, the abundance of Ag- and Au-containing precious metal minerals analyzed along the core and margin of "Vein 1" (native silver, hessite, acanthite, electrum, geffroyite, chlorargyrite, kurilite) do not display apparent systematic changes moving laterally (Figure 2.9 c) along the vein's length. A line of best-fit would show that they slightly increase moving deeper into the footwall along the vein's core. Additionally, these discrete Ag- and Au-containing precious metal minerals do not display unambiguously higher concentrations along the vein core vs. the vein margin or vice versa. However, samples along the margin grade ~60 g/t higher Ag+Au, while 7/10 vein core samples contain higher concentrations of Ag- and Au-containing precious metal minerals. This discrepancy could be accounted for by Ag and Au solid solution within base metal sulfides (notably chalcopyrite) and

suggests higher Ag+Au grades may be attained along vein margins within sharp-walled environments.

Signature base metal and precious metal ratios along the vein's core show that Cu/(Cu+Ni) ratios remain fairly constant laterally (at the scale of 10 meters) while Pt/(Pt+Pd) ratios exhibit slight drops moving deeper into the footwall away from the SIC contact (Figure 2.9 d).

Ten sets of mass balance calculations were carried out along the vein's core to determine what the dominant carriers for Ni, Pb, Pt, Pd, Ag, Au, and Sn are and whether these carriers show any lateral variability at the scale of an individual stope (Figure 2.10). The Ni budget is accounted for by pentlandite and millerite when they are present in any concentration that can be seen with the naked-eye (i.e. calculations show that if pentlandite+millerite concentrations exceed 0.05 vol% then these phases will contribute to nearly the entire mass balance for nickel). Chalcopyrite (avg. 112 ppm Ni) and magnetite (avg. 3251 ppm Ni) also contribute to the Ni mass balance in samples that do not contain pentlandite and/or millerite (or they are present in very low concentrations). Lead budgets for these vein core samples are nearly entirely covered by galena and contributions from solid solution in BMS are small to negligible. Cotunnite contributes a small fraction to the Pb mass balance within a few samples. Platinum mass balances are accounted for exclusively by platinum group minerals (moncheite, michenerite, merenskyite, sperrylite) and moncheite is by far the main carrier for Pt along this vein (as well as in most sharp-walled vein samples reported in this thesis). Palladium mass balances are
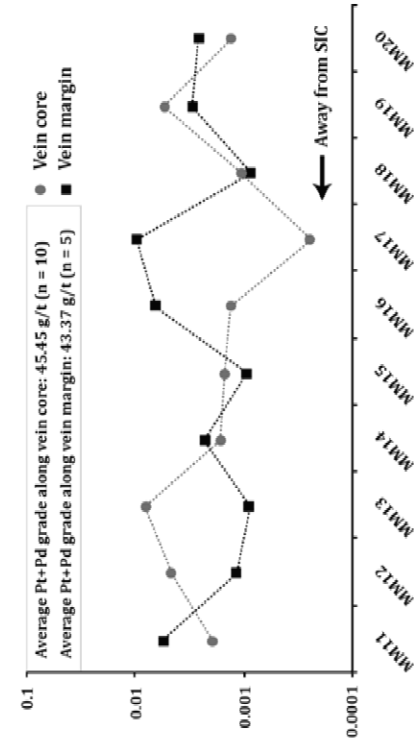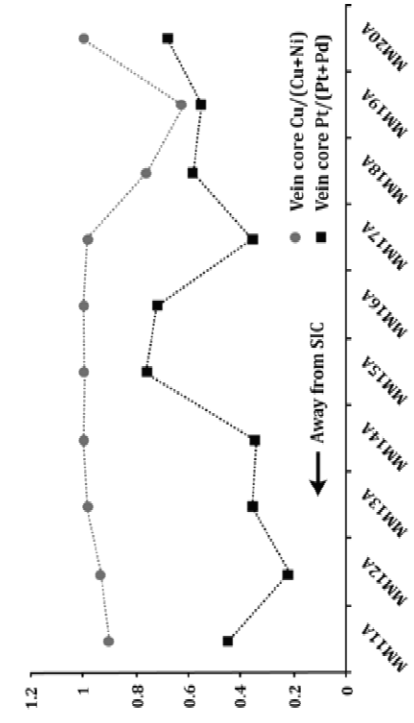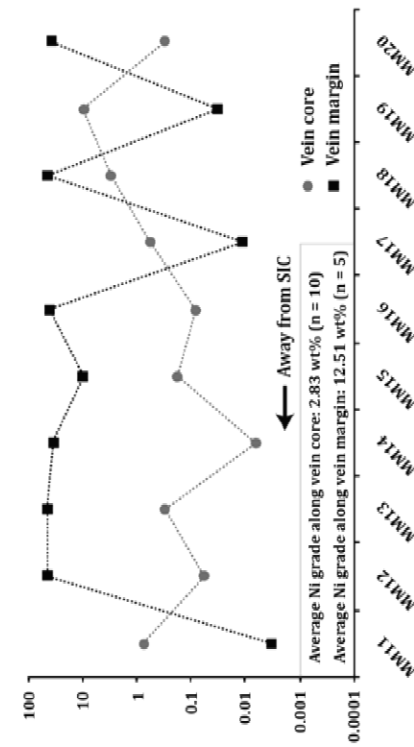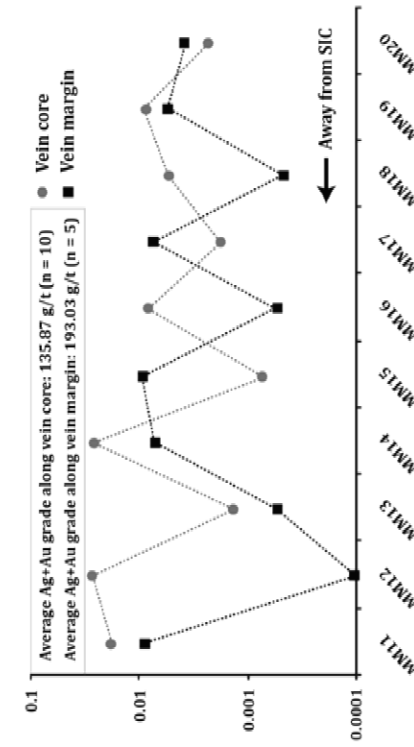
Figure 2.9 (previous page): Mineralogical and bulk rock variability along the length of "Vein 1" and with proximity to Sudbury Breccia host. See digital appendix for supplementary data. a) Comparison of the concentration of Ni-containing base metal sulfides (pentlandite, millerite) between samples taken from the vein core (furthest from Sudbury Breccia contact) and samples taken from the vein margin (<20 cm from Sudbury Breccia contact). There is a clear tendency for samples taken from the margin to contain concentrations of Ni-containing base metal sulfides that are up to an order of magnitude higher than those taken from the core. This observation coincides with ~10 wt% higher average Ni grades for those samples taken along the margin. The black arrow points in a direction that is further away from the SIC contact and deeper into the footwall to the SIC. b) Comparison of the total concentration of all Pt- and Pd-containing minerals (moncheite, michenerite, merenskyite, sperrylite, kotulskite, froodite, unnamed $(Pd,Pt)(Bi,Te)_2$ mineral, menshikovite) between samples taken from the vein core and samples taken from the vein margin. There does not seem to be any correlation between the concentration of these platinum group minerals with proximity to Sudbury Breccia. This is backed by approximately equal Pt+Pd grades between the vein core and the vein margin. c) Comparison of the total concentration of all Ag- and Au-containing minerals (native silver, hessite, acanthite, electrum, geffroyite, chlorargyrite, kurilite) between samples taken from the vein core and samples taken from the vein margin. There does not appear to be any correlation between the concentration of these precious metal minerals with proximity to Sudbury Breccia. However, average Ag+Au grades are slightly higher for samples collected along the vein margin. d) Variations in Cu/(Cu+Ni) and Pt/(Pt+Pd) along the core of "Vein 1." Cu/(Cu+Ni) remains fairly equal along the vein's length; while Pt/(Pt+Pd) appears to show a slight decrease (with the exception of 2 samples) moving away from the SIC contact and correspondingly further/deeper into the SIC footwall.

dominated by michenerite and moncheite and the magnitude of their dominance does not dwindle moving laterally in either direction. A few other PGM (merenskyite, froodite, kotulskite) play smaller (seemingly unsystematic) roles in the Pd mass balance within a few samples and base metal sulfide contributions to the Pd mass balances are small. Silver mass balances are accounted for predominantly by a diverse set of Ag-containing precious metal minerals (native silver, hessite, electrum, geffroyite, acanthite, chlorargyrite); however hessite and native silver account for the bulk of the Ag budget in all 10 vein samples. Solid solution in chalcopyrite (avg. 4.4 ppm Ag) plays a small role in the Ag budget for all 10 samples. Gold budgets are accounted for by solid solution within chalcopyrite (avg. 0.10 ppm Au) unless even a single 10 μm x 10 μm grain of electrum is present. If virtually any electrum is present within chalcopyrite matrix then electrum will contribute either substantially or entirely to the Au budget. This "nugget" effect makes Au-carriers difficult to predict within the veins. Tin budgets are divided fairly evenly between cassiterite and chalcopyrite (avg. 92 ppm Sn) for the majority of the samples analyzed but magnetite (avg. 130 ppm Sn) also contributes relevant amounts to the overall Sn mass balance within samples that are magnetite-rich.
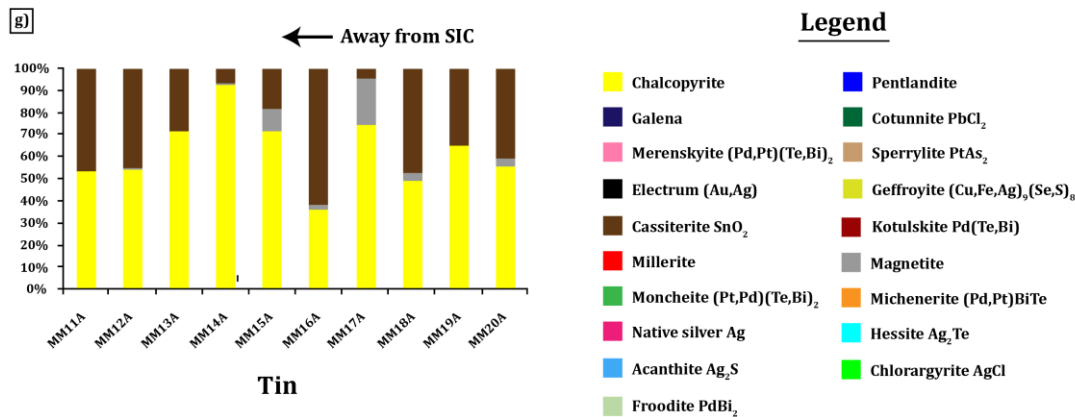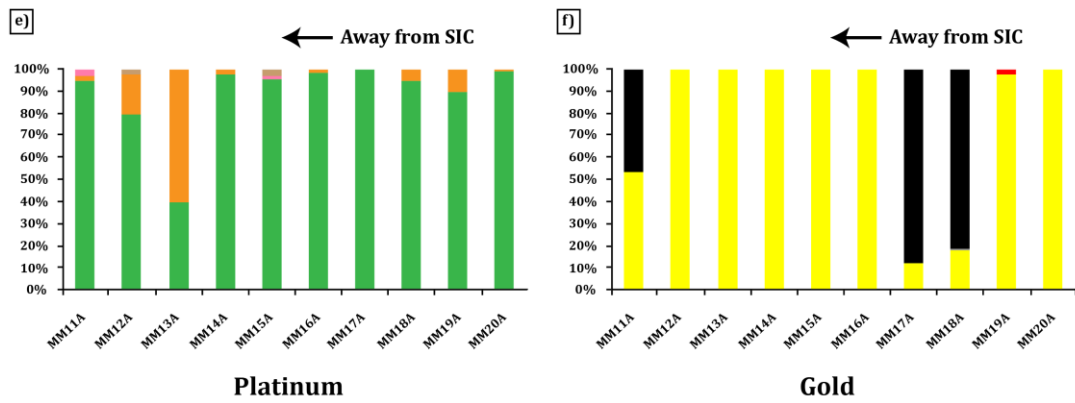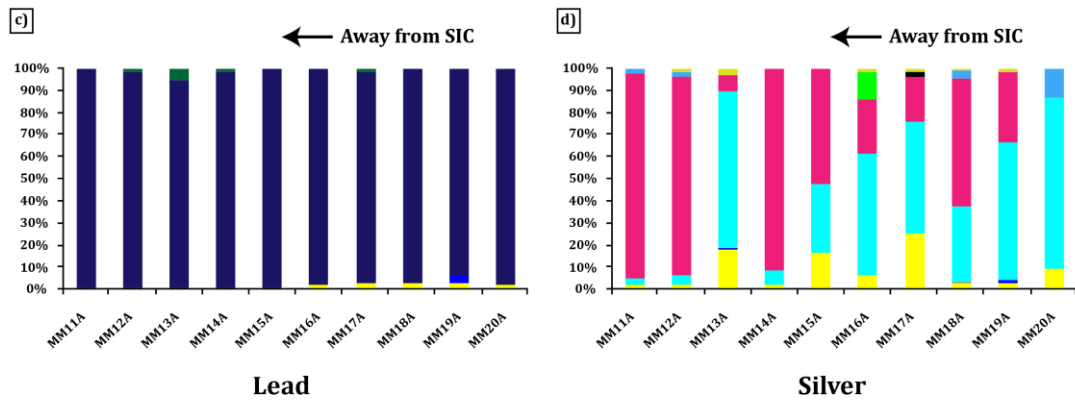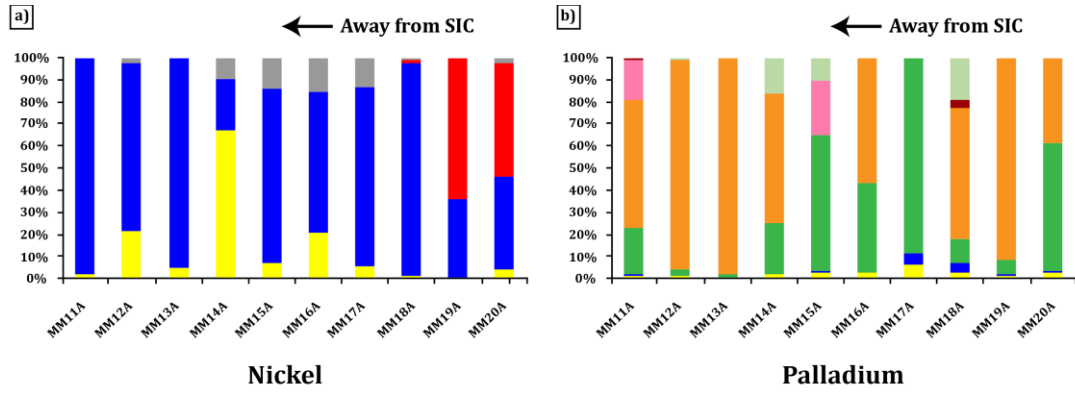
a) **Nickel** — Away from SIC

b) **Palladium** — Away from SIC

c) **Lead** — Away from SIC

d) **Silver** — Away from SIC

e) **Platinum** — Away from SIC

f) **Gold** — Away from SIC

g) **Tin** — Away from SIC

Legend

- Chalcopyrite
- Galena
- Merenskyite (Pd,Pt)(Te,Bi)$_2$
- Electrum (Au,Ag)
- Cassiterite SnO$_2$
- Millerite
- Moncheite (Pt,Pd)(Te,Bi)$_2$
- Native silver Ag
- Acanthite Ag$_2$S
- Froodite PdBi$_2$
- Pentlandite
- Cotunnite PbCl$_2$
- Sperrylite PtAs$_2$
- Geffroyite (Cu,Fe,Ag)$_9$(Se,S)$_8$
- Kotulskite Pd(Te,Bi)
- Magnetite
- Michenerite (Pd,Pt)BiTe
- Hessite Ag$_2$Te
- Chlorargyrite AgCl

67

Figure 2.10 (previous page): Nickel, Pb, Pt, Pd, Ag, Au, and Sn mass balances for the ten samples from the center of "Vein 1" (Figure 2.2 b, c). The arrows point in a direction that is deeper into the SIC footwall. See Table 2.6 for LA-ICPMS concentration values and digital appendix for mass balance calculator.

2.6 Discussion

2.6.1 Crystallization history of "high sulfide" sharp-walled vein mineralization

Following the accumulation of immiscible sulfide droplets along the basal contact of the SIC at ~1.85 Ga, a separate system began to evolve that would eventually give rise to the heterogeneous polymetallic ore packages that give Sudbury its present status as a world class Ni-Cu-PGE mining camp. This pool of sulfide liquid concentrated a large suite of ore metals. The first major assemblage to crystallize was monosulfide solid solution (MSS) at ~1120°C (Naldrett 1984). MSS collected Os, Ir, Ru, Rh, Re, and Co, and left behind a residual melt enriched in Cu, Ag, Au, Pt, Pd, As, Bi, Cd, Pb, Se, Sn, Te, Zn, and some Ni (Dare et al. 2014). Migration of this residual liquid into the underlying footwall occurred after the formation of MSS and was enhanced by the presence of channels/pathways that were created during meteorite impact (Rousell et al. 2003). Maximum thermal stabilities of the phases reported in the rest of this section come from many sources and it was not possible to constrain pressure for all of the phases that are reported. It is unlikely that any of the phases became saturated in these footwall systems above the temperatures that are reported; however, some phases may have stabilized at temperatures notably lower than the temperatures that are reported here. With respect to the "high sulfide" sharp-walled veins in the Coleman Mine environment, PGE-stannides and PGE-arsenides were likely the first phases to stabilize as residual liquids descended into the footwall. Sperrylite $PtAs_2$, paolovite Pd_2Sn and niggliite PtSn crystallized at high temperatures as solitary grains at <1369°C, <1326°C, and <1305 °C,

respectively (Skinner et al., 1976; Makovicky et al., 1992; Okamoto 1990; Elliot, 1965; Kosovinc and Grgasovic, 1972; Maleviskiy et al., 1978; Hansen and Anderko, 1958). Cassiterite SnO_2 occurs in clusters of primary euhedral inclusions (primarily chalcopyrite-hosted) and therefore should have formed early in sharp-walled vein paragenesis but an absolute stability value for its formation in magmatic sulfide environments was not found. The first phase to occur in minor concentrations in the veins (typically 1-5 vol%) was likely magnetite at >1000°C (Naldrett 1969; Fonseca et al., 2008; Dare et al., 2012). The presence of magnetite also indicates that the residual liquid was sufficiently oxidized to solidify in the stability field of intermediate solid solution (ISS). ISS would be the first major phase to crystallize at temperatures between 950°C and 800°C (Ballhaus et al., 2001) and later subsolidus exsolution of ISS resulted in the formation of the major sulfides that comprise the veins: chalcopyrite (<550°C), pentlandite (<650°C) and cubanite (<210°C) (Yund and Kullerud, 1966; Cabri, 1973; Peregoedova and Ohnenstetter, 2002; Sinyaknova and Kosyakov, 2009). Based on textural equilibrium between millerite, pentlandite, and chalcopyrite (grain-boundary relationships, inclusion characteristics, presence of trails of intergrown pentlandite and millerite within chalcopyrite, etc.), it is likely that millerite exsolved from (Ni-rich) ISS in the same temperature range as pentlandite and chalcopyrite. Galena forms ubiquitous anhedral inclusions in the veins and stabilizes at temperatures <1114°C (Freidrich 1907); however, it often fills voids between chalcopyrite grains and therefore likely exsolved from ISS (incorporating notable Se: >1 wt%) after the formation of the more volumetrically-abundant BMS (Pb ionic radius is too large for crystal structures of chalcopyrite,

cubanite, pentlandite, millerite, etc.). Although it can stabilize at <1078°C (Lawson, 1951), the selenide clausthalite PbSe likely formed in the same (lower) temperature realm as galena due to the observation that they are intergrown with one another. This primary association with galena is also exhibited by sphalerite and hawleyite CdS; suggesting similar positions in sharp-walled vein paragenesis (although sphalerite is stable at temperatures as high as 1680°C; Freidrich 1907).

Contemporaneous with the formation of ISS, an immiscible intercumulus semi/precious metal-rich (Pt-Pd-Bi-Te-Ag) liquid exsolved from the residual Cu-rich liquid and this new dense liquid was unable to settle out along the base of the veins. This liquid formed composite grains of moncheite $(Pt,Pd)(Te,Bi)_2$ (<920°C) and hessite Ag_2Te (<950°C) within voids between ISS grains (Helmy et al., 2007; Cabri and Laflamme, 1976). Unfortunately, it is difficult to determine whether the composite grains observed in this study are situated at the original grain boundaries of ISS because of the later exsolution of chalcopyrite and pentlandite from ISS. Another possibility is that these grains exsolved directly from ISS but this seems highly unlikely for two reasons: (1) Accepted exsolution of PGE from ISS to form PGM in magmatic sulfides from other deposits, like those from the Platreef of the Bushveld Complex (Hutchinson and McDonald, 2008), display thin (chalcopyrite-hosted) lath-like textures characteristic of exsolved phases; the composite grains in this study are rounded (droplet-like) and are not blade-like/elongated (Figure 2.11), (2) The modal ratio between moncheite and hessite along individual veins is notably consistent, with no end-member moncheite or hessite occurrences (keeping in mind

71

this is a 2D view of a 3D entity) (Figure 2.11). Platinum, Pd, Bi, Te, and Ag would need to be mixed extremely homogeneously in ISS to exsolve down-temperature into such compositionally-homogeneous composite grains. Other primary bismuthotellurides observed in different areas of the Coleman stockwork vein system, such as merenskyite $(Pd,Pt)(Te,Bi)_2$, michenerite $(Pd,Pt)BiTe$, and kotulskite $Pd(Te,Bi)$ either crystallized from immiscible semi/precious metal melt or exsolved from ISS at <740°C, <501°C, and <746°C, respectively (Hoffman and MacLean, 1976; Helmy et al., 2007). The composition of the PGM was largely controlled by the local availability of Pt, Pd, Bi, and Te. In a similar manner to the aforementioned bismuthotellurides, the bismuthides froodite $PdBi_2$ and sobolevskite $PdBi$ stabilized at <485°C and <618°C (Hoffman and MacLean, 1976; Okamoto, 1994). The unnamed $(Pd,Pt)(Bi,Te)_2$ phase would have crystallized in the same temperature range as these PGM.

Geffroyite $(Cu,Fe,Ag)_9(Se,S)_8$ is a reoccurring phase in sharp-walled vein samples that occurs as primary anhedral inclusions in BMS and it is sometimes intergrown with galena or in contact with silicates, galena, or magnetite. No experimental constraints can be put on its formation, but, based on its textural occurrence, it would have formed late in the crystallization history coincident with the crystallization of galena. Four grains of parkerite $Ni_3Bi_2S_2$ were observed intergrown with michenerite and froodite in a sample that was collected at the margin of a vein. Based on the fact that parkerite is intergrown with end-member PGM, only occurs in one sample, occurs along a vein margin, and does not appear to
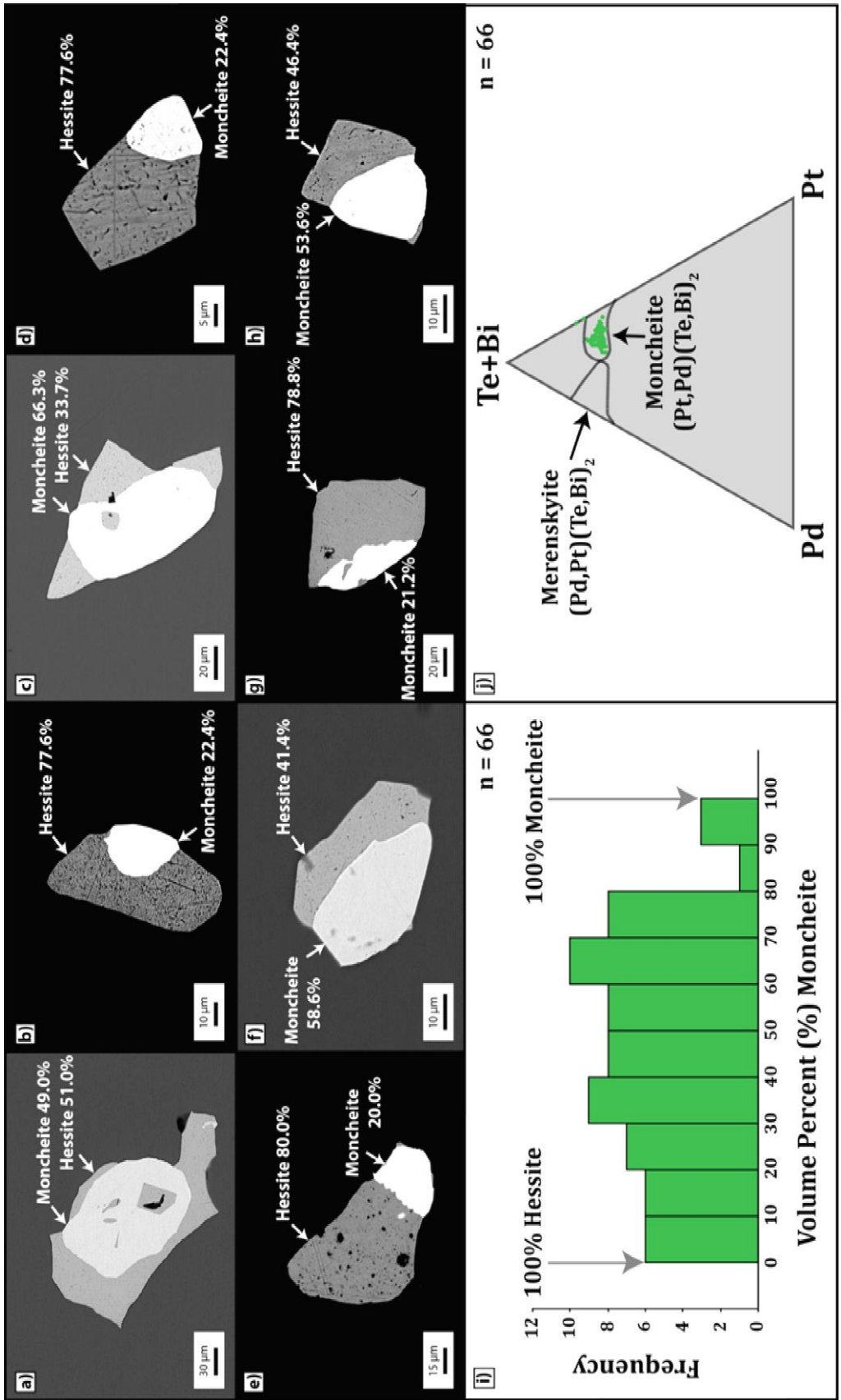
Figure 2.11 (previous page): Composite grains of moncheite and hessite along "Vein 1." (a) – (h) Back-scattered electron images of moncheite-hessite composite grains displaying variable volume % ratios. Volume percent values were calculated directly from the back-scattered electron images using the computer software *ImageJ*. See digital appendix for sample numbers associated with each image. i) Histogram showing variation in volume % ratios for 66 moncheite-hessite composite grains analyzed along "Vein 1." j) Pt-Pd-Bi-Te ternary from Harney and Merkle, 1990 that outlines the fields for moncheite and merenskyite. With the exception of two grains, all analyses span a small compositional range and cluster tightly within the center of the moncheite field. n = 66.

be a primary inclusion, it is likely that parkerite is a xenocrystic phase in the vein. Electrum (Au,Ag) forms anhedral inclusions in base metal sulfides that are sometimes intergrown with (or at least in contact with) PGM (sperrylite, froodite). It is difficult to place precise constraints on the formation of electrum; however it likely exsolved locally from ISS where Au and Ag were not taken up in base metal sulfides. One grain of paratellurite TeO_2 was observed hosted in chalcopyrite and in contact with moncheite. Paratellurite stabilizes at <732°C (Wiberg et al. 2001), thus likely formed before the dominantly Pd-PGM began to crystallize. One chalcopyrite-hosted anhedral inclusion of zincite ZnO and one pentlandite-hosted anhedral inclusion of bismite Bi_2O_3 were also observed. Zincite has an extremely high melting point of 1975°C and bismite melts at 817°C (Patnaik 2003). It is difficult to place these oxides in the vein paragenetic sequence but they likely formed before the exsolution of pentlandite at temperatures >650°C. The single grain of molybdenite hosted in chalcopyrite is likely an exsolution product of ISS at <650°C (Morimoto and Kullerud, 1962; Takeno and Moh, 1977). One primary anhedral inclusion of menshikovite $Pd_3Ni_2As_3$ was observed hosted in chalcopyrite. Experimental data on menshikovite is not available but based on its composition and the melting temperatures of chemically-similar phases, it likely formed somewhere in between the crystallization of ISS and the exsolution of chalcopyrite.

Pyrite and pyrrhotite are extremely minor and exhibit invariably resorbed grain boundaries within all occurrences. It is likely that they represent xenocrysts of early-forming MSS cumulate fragments. Pyrrhotite is mainly found as very fine

coatings on magnetite. Only two occurrences of barite were uncovered in sharp-walled vein samples and both crystals were in contact with silicate phases; thus barite cannot be unambiguously identified as a sharp-walled vein phase.

Cotunnite $PbCl_2$ and chlorargyrite AgCl are clearly secondary as they occupy cracks in base metal sulfides (Figure 2.4 j). Coupled with work at the Fraser Mine (Hanley and Mungall, 2003) that documents Cl-rich alteration haloes enveloping entire sharp-walled vein systems, it seems highly likely that a late-stage Cl-rich fluid exsolved from the veins, precipitating metal chlorides within open areas in sharp-walled veins and transferring large amounts of chlorine to surrounding wallrock. No experimental work was found for chlorargyrite. Cottunite can stabilize at temperatures <501°C (Lide 1998). Two grains of kurilite $(Ag,Au)_2(Te,Se,S)$ were observed as chalcopyrite-hosted inclusions in contact with cotunnite. Their association with cotunnite suggests they are paragenetically late with respect to the majority of the sharp-walled vein phases. Native silver and acanthite Ag_2S are present infilling fractures and cavities within base metal sulfides. Although native silver has a high melting point (<963°C), it likely represents a late phase (along with acanthite), which is seen readily in their textures (Figure 2.4 n, p).

Bornite was only encountered in one high sulfide sample (at the termination/ extremities of a vein system in the 153 ore body; Figure 2.4 d), where it occurred as massive sulfide patches intergrown with chalcopyrite, millerite, carbonate, quartz, epidote, k-feldpsar, and chlorite. Approximately 56 volume percent (%) of this thin section was bornite – placing it completely out of the low

sulfide classification scheme (<5 vol% total sulfide minerals). The occurrence of bornite at vein terminations is not well understood given that bornite contains less sulfur than ISS. Thirteen primary inclusions of naumannite Ag_2Se were also observed in this same sample. Melting point data was not found for naumannite but 12/13 naumannite inclusions were intergrown with galena.

2.6.2 Crystallization history of "low sulfide" PGE-rich mineralization

Coeval, or prior to (Farrow et al. 2005), the emplacement of the sharp-walled veins, a chemically-separate hydrocarbon-bearing (Hanley et al. 2005; Kerr 2013) hydrothermal fluid developed and (likely) separated from an SIC-related body (SIC, footwall granophyre, etc.) and incorporated substantial Pt and Pd, as well as other precious-, base-, and semi-metals including Cu, Fe, Ni, Zn, As, Au, Ag, Bi, and Te from an as-of-yet unidentified source. This fluid became mobilized into many of the same openings/pathways in the footwall as the sharp-walled veins. Upon its traverse away from the SIC contact/immediate footwall area, the hydrothermal fluid began to cool and precipitate predominantly end-member PGM (in stark contrast to the variable solid solutions exhibited by many of the PGM in high sulfide mineralization). The reduction in Bi-Te/Pd-Pt exchange in these "low sulfide" PGM may indicate precipitation at temperatures lower than in the sulfide veins (White, 2012). The first PGM to precipitate from this fluid was likely sperrylite $PtAs_2$ at temperatures <1369°C (Skinner et al., 1976). Galena can stabilize at temperatures <1114°C (Freidrich 1907); however it likely formed coeval to the precious metal bismuthotellurides as it was sometimes observed to be intergrown with them. This

galena did not incorporate Se like the galena grains that crystallized within the sharp-walled veins (Figure 2.12). Moncheite $(Pt,Pd)(Te,Bi)_2$ and hessite Ag_2Te precipitated as predominantly solitary grains at temperatures of <920°C and <950°C, respectively (Helmy et al., 2007; Cabri and Laflamme, 1976). In this case, these minerals rarely formed composite grains and moncheite crystallized nearly 100% Pt with no Pd solid solution. Bismuthiferous galena $(Pb,Bi,Ag)S$ likely crystallized around these temperatures as one grain was observed intergrown with moncheite. Insizwaite $Pt(Bi,Sb)_2$ crystallized at temperatures <765°C (with no detectable antimony) (Cabri and Harris, 1972), kotulskite $Pd(Te,Bi)$ stabilized at <746°C (Hoffman and MacLean, 1976), merenskyite $(Pd,Pt)(Te,Bi)_2$ precipitated with negligible Pt solid solution at temperatures <740°C (Hoffman and MacLean, 1976; Helmy et al., 2007), froodite $PdBi_2$ formed at <620°C (Hoffman and MacLean, 1976), sobolevskite $PdBi$ was saturated at temperatures <618°C (Okamoto, 1994), bismuthian palladian melonite $(Ni,Pd)(Te,Bi)_2$ crystallized at <600°C (Cabri and Laflamme, 1976), tsumoite $BiTe$ formed at <540°C (Hoffman and MacLean, 1976), and pure-Pd michenerite $(Pd,Pt)BiTe$ dropped out of solution at temperatures <501°C (Hoffman and MacLean, 1976). No experimental data were found for the opposite end-member of the michenerite solid solution series – maslovite $PtBiTe$; however it likely formed at temperatures >501°C. Maslovite contained no Pd solid solution. The unnamed $(Pd,Pt)(Bi,Te)_2$ phase also encountered in the sharp-walled veins would have crystallized in the same temperature range as these PGM.

Electrum (Au,Ag) was hosted by both silicates and BMS and in some instances it was observed intetrgrown with tsumoite. These textures suggest electrum was paragenetically early in low sulfide genesis; coincident with the precipitation of some of the PGM. Native silver was also hosted by both silicates and BMS and appeared to be much thicker (pure native silver signals with no background) than the secondary native silver concentrated around BMS cavities in high sulfide mineralization. While the upper stability limit of native silver is 963°C, this phase is difficult to place in the paragenetic sequence (i.e. not associated with phases that place paragenetic constraints) except that it likely formed before the BMS. One grain of native zinc was observed hosted in calcite within the (garnet-bearing) most-evolved low sulfide sample analyzed in this study. Local unavailability of sufficient anions (i.e. S^{2-}) coupled with rapid changes in fluid composition could cause it to precipitate (it was clearly one of the last metallic phases to crystallize in the low sulfide system).

An important mineral group that was prevalent in low sulfide mineralization and virtually absent in sharp-walled vein systems were the sulfbismuthites. Wittichenite Cu_3BiS_3 and crerarite $Pt_{2-x}(Bi,Pb)_{11}(S,Se)_{11}$ formed fairly early in the paragenesis of low sulfide mineralization because both phases were observed intergrown with hessite. Parkerite $Ni_3Bi_2S_2$ was observed intergrown with both lower temperature froodite and higher temperature galena and could therefore have formed over a fairly large range in the paragenetic sequence. It is tougher to place temporal constraints on the last two sulfbismuthites: aikinite $PbCuBiS_3$ and

As-bearing argentocuprocosalite $(Pb,Cu,Ag)_2Bi_2S_5$. Both phases are entirely hosted by silicate minerals and most likely precipitated before the sulfides.

The BMS in low sulfide deposits were paragenetically some of the last ore minerals to crystallize. Assuming cuprous complexes were the major source of Cu in hydrothermal fluid, and based on experimental work on chalcopyrite/bornite solubilities in hydrothermal solution (Crerar and Barnes, 1976), coupled with fluid inclusion work presented in Chapter 3, it seems reasonable that chalcopyrite and bornite precipitated as blebs, trails, and disseminations in coeval silicates/carbonates within the temperature range 300 – 150°C. By spatial and textural association of millerite within chalcopyrite/bornite/coeval silicates and carbonates, it appears that millerite crystallized within this same temperature range. Acanthite Ag_2S was observed intergrown with chalcopyrite and thus represents a late-stage phase as well.

Only one grain of chlorargyrite AgCl and one grain of cotunnite $PbCl_2$ were observed in all low sulfide samples that were analyzed. Both chlorargyrite and cotunnite comprised isolated anhedral inclusions within silicate hosts. While they could have formed from the hydrothermal fluid responsible for low sulfide mineralization, it seems more likely that they represent foreign phases precipitated off nearby sharp-walled vein systems. Barite crystals were found in one sample but they did not show any equilibrium textures with low sulfide phases and are thus interpreted as xenocrysts from the Levack Gneiss Complex. Cassiterite SnO_2 and tenorite CuO were found in single samples as isolated anhedral inclusion(s). It is

unlikely that cassiterite or tenorite constitute low sulfide phases and are therefore most likely foreign. The presence of bismite Bi_2O_3 in low sulfide mineralization is not well understood. It is commonly intergrown with high temperature phases such as galena or hessite. However, these oxides should not exist in low sulfide mineralization as will be discussed in the following section. It is possible that human error misidentified bismite when it was really bismuthinite Bi_2S_3 or native bismuth.

2.6.3 Sharp-walled vein "high sulfide" and high-PGE "low sulfide" mineralization: Two independent systems that deposited Cu-Ni-PGE mineralization by evolving in opposite redox directions

While models for the origin of sharp-walled vein "high sulfide" mineralization are generally accepted and ascribed to magmatic fractionation (± ore metal redistribution by high temperature volatiles), models for high-PGE "low sulfide" mineralization are in their infancy. There is one particular mineralogical similarity between the two mineralization styles which seems to cause researchers to combine these styles into the same genetic model: the enigmatic presence of bornite. The presence of primary magnetite in sharp-walled veins indicates that the residual liquid was sufficiently oxidized to solidify in the stability field of ISS (Ballhaus et al., 2001). However, because bornite contains less sulfur than ISS, the deposition of massive bornite at vein terminations indicates that the evolution of these veins could not have followed traditional sulfide fractionation models. The inability to adequately explain the presence of massive bornite at the extremities of stockwork vein systems has resulted in the misconception that bornite-bearing

high-PGE blebs, disseminations, and stringers are in some way related to the deposition of sharp-walled veins. This study suggests that these two mineralization styles (high sulfide and low sulfide) each produced bornite (+Cu-Ni-PGE mineralization) through entirely independent geochemical mechanisms.

In a manner analogous to that proposed for the Ni-rich Epidote Zone at the Fraser Mine (Farrow and Watkinson, 1996), footwall-hosted sharp-walled veins are recording an increasingly oxidizing geochemical system. Evidence for this is fourfold:

1) Recent experimental studies have demonstrated that Cu-rich magmatic sulfides may be the result of magmatic oxidation. Wohlgemuth-Ueberwasser et al. (2013) demonstrated that, as the fO_2 of sulfide melt is progressively increased, the Cu/Fe ratio of the melt also increases because of the preferential conversion of FeS into FeO and $FeO_{1.5}$, and the resistance of Cu_2S to being converted into oxide components (even at fO_2 values corresponding to the sulfide/sulfate transition: >FMQ+1). The oxidation of sulfide melt also leads to increases in its bulk metal/S ratio (e.g., Naldrett 1969; Kaiser and Elliot 1986; Kress 1997, 2000, 2007; Fonseca et al. 2008; Moretti and Baker 2008). Ballhaus et al. (2001) showed that both liquidus and solidus temperatures for sulfide melts decrease with an increase in their bulk metal/S ratio. For this reason, oxidized sulfide melts are expected to fractionate past ISS stability and solidify at a Cu-rich thermal minimum where both bornite and millerite are present as equilibrium phases. Massive bornite (56 vol%) and millerite (1 vol%) are both present in equilibrium with chalcopyrite (29 vol%) in the high

sulfide bornite-bearing sample from the vein termination that is alluded to in this study.

2) Precious metal selenides such as padmaite PdBiSe from the Jinchuan intrusion, China (Prichard et al. 2013) and fischesserite Ag_3AuSe_2 and naumannite Ag_2Se from the De Lamar Mine, Idaho, USA (Bindi and Cipriani, 2004) have been reported in equilibrium with carbonate assemblages in oxidizing geochemical environments. The stabilization of these selenide minerals is suggested to arise as a consequence of progressive oxidation of the medium responsible for mineralization. Not surprisingly, the selenide mineral naumannite Ag_2Se is a dominant precious metal mineral (13 grains) in the massive bornite sample collected at the termination of the Coleman stockwork vein system where massive bornite, chalcopyrite, and millerite are in equilibrium with carbonate. Only one other grain of naumannite was observed in the entire vein system. The crystallization of naumannite appears to represent the end-member of an oxidizing sulfide melt system.

3) If the bulk metal/S ratio of the sulfide melt that descended into the footwall was raised, the availability of the S^{2-} anion for metal cations would be correspondingly lowered. In its place we would expect Se^{2-}. It is likely that footwall Se-bearing galena (Figure 2.12) reported by many authors (e.g., Jago et al. 1994; Farrow and Watkinson, 1997; Ames et al. 2007; Dare et al. 2011; Dare et al. 2014 etc.) is recording this evolution whereby the Se-content of galena positively correlates to the fO_2 of the sharp-walled veins (i.e., the deeper and further away from the SIC contact that you move along individual sharp-walled veins, the higher the Se-

Figure a) Histogram showing Frequency versus Weight Percent (%) Se detected in galena by SEM-EDS. Low sulfide (n = 179), Reducing evolution. High sulfide (n = 164), Oxidizing evolution (Increase bulk metal/S). Detection limit indicated near 0.0.

Figure b) Bornite, Pb(S,Se), Ag$_2$Se, High sulfide, 2 μm scale bar.

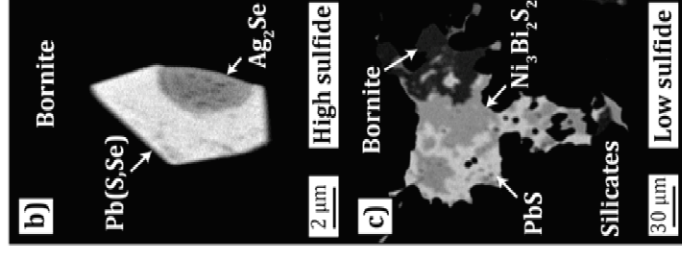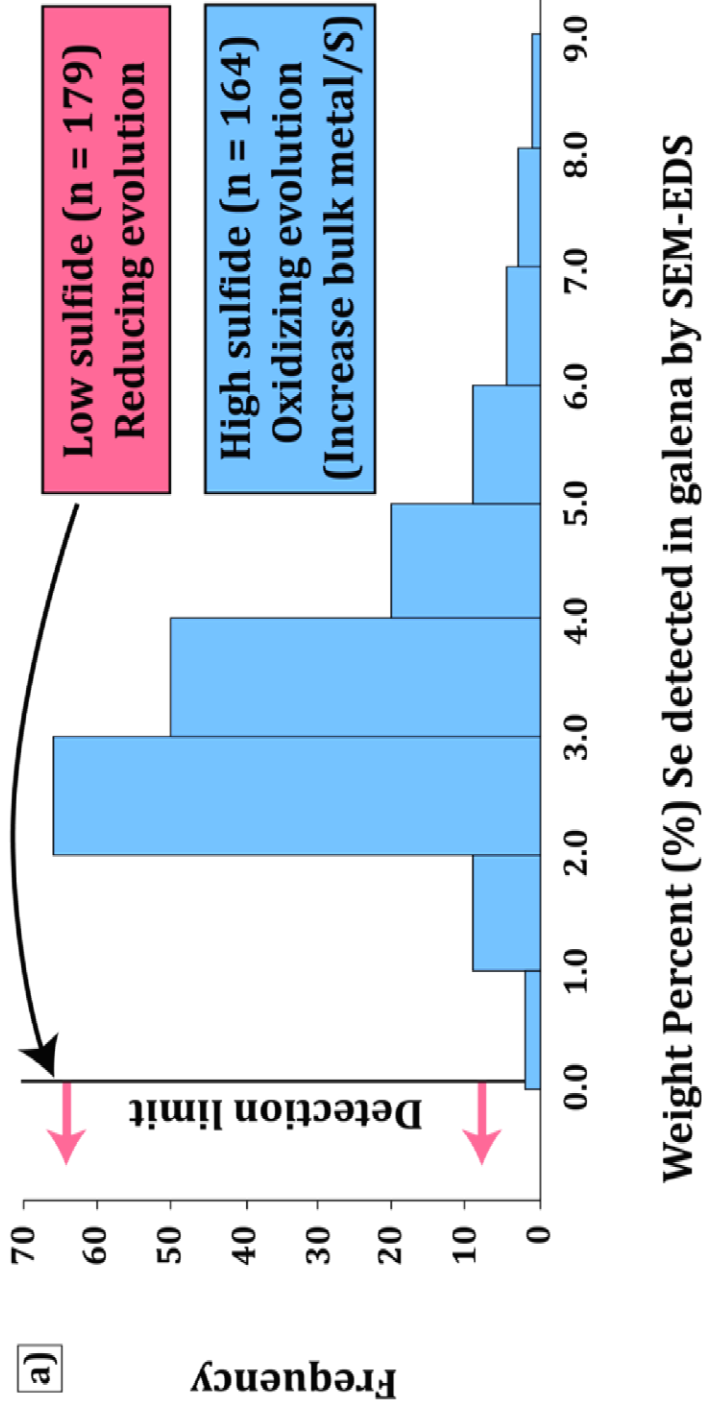Figure c) Bornite, Ni$_3$Bi$_2$S$_2$, PbS, Silicates, Low sulfide, 30 μm scale bar.

Figure 2.12 (previous page): Effects of mineralization style on Se concentration in galena. The data plotted constitutes a representative subset of galena analyses from samples taken at various localities at the Coleman Mine. See digital appendix for sample numbers associated with each image. a) Histogram showing the variation in Se concentrations measured in galena from high sulfide samples and the absence of Se in galena from low sulfide samples encountered during SEM-EDS analyses. Galena is a (relatively) late sulfide phase in the high sulfide sharp-walled veins and its incorporation of Se is an artifact of progressive oxidation which results in increasing bulk metal/S ratios (less S availability to metal cations). Since the low sulfide system is characterized by progressive reduction, the bulk metal/S ratio was not affected in the sense that it was in the high sulfide sharp-walled veins and all galena crystallized without S deficiencies and the need to incorporate Se in its crystal structure. b) Intergrown Se-rich galena (3.36 wt% Se) and naumannite (Ag_2Se) in massive bornite (high sulfide sample from the vein termination). In this assemblage, the selenide naumannite is indicative of oxidizing environments (see text). c) Intergrown stoichiometric galena (PbS; Se-free), parkerite ($Ni_3Bi_2S_2$), and bornite in a silicate host. Minerals from the sulfbismuthite group are indicative of reducing environments (see text).

content in galena). One grain of clausthalite PbSe was observed in the veins, potentially recording an extremely high local bulk metal/S ratio. Solid solution in the selenide geffroyite $(Cu,Fe,Ag)_9(Se,S)_8$ (observed in 7/25 sharp-walled vein samples analyzed) is also likely recording this oxidizing phenomenon.

4) The prevalence of oxide minerals cannot be discounted. Magnetite is a minor (~1-5 vol%) phase in virtually all high sulfide vein samples. It is unclear at present how the concentration and chemistry of magnetite varies with position in the footwall but its presence suggests some extent of oxidation. Likewise, cassiterite SnO_2 occurs as clusters of primary chalcopyrite-hosted euhedral inclusions. Other less common oxides in the veins are bismite Bi_2O_3, paratellurite TeO_2, and zincite ZnO. It seems unlikely that these oxides would prevail in progressively reducing geochemical systems.

Low sulfide mineralization formed through the introduction of a PGE (Pt, Pd)-loaded hydrothermal fluid into the footwall that became enriched in hydrocarbons (Hanley et al. 2005; Kerr 2013). This fluid was sourced from an igneous body (See Chapter 3 SIMS) and became increasingly reducing over the course of its evolution upon reacting with deep $CaCl_2$-rich groundwater (See Chapter 3 SIMS/Discussion) to precipitate blebs, disseminations, and stingers of sulfide minerals and precious metal minerals that contained high bulk PGE/S ratios. Evidence for reduction in the low sulfide system is twofold:

1) Zoned hydrothermal garnet comprising part of a low sulfide assemblage that was sampled from the extremities of low sulfide mineralization in the 153 ore body

records the evolution of low sulfide-type mineralization (See Chapter 3). Trace element variation across garnets for elements that take on more than 1 oxidation state, compositional considerations in areas of garnet-epidote equilibria, and the timing of sulfide mineralization as deduced by silicate-sulfide textures, indicate that the fluid responsible for low sulfide mineralization became more reducing over the course of its evolution. Chapter 3 discusses this in detail.

2) Sulfbismuthites, such as aikinite $PbCuBiS_3$ and emplectite $CuBiS_2$ from the Bald Mountain Gold Mining District, Nevada, USA (Nutt and Hofstra, 2007) and bismuthinite Bi_2S_3, lillianite $Pb_3Bi_2S_6$, matilaite $AgBiS_2$, aikinite $PbCuBiS_3$, mummeite $(Cu,Ag)_{3-4}(Bi,Pb)_{7-8}S_{13}$, emplectite $CuBiS_2$, and wittichenite Cu_3BiS_3 from the Kamariza area, Lavrion, Greece (Voudouris et al. 2008) are associated with geochemical systems characterized by progressively reducing hydrothermal fluids. The sulfbismuthites parkerite $Ni_3Bi_2S_2$, aikinite $PbCuBiS_3$, wittichenite Cu_3BiS_3, crerarite $Pt_{2-x}(Bi,Pb)_{11}(S,Se)_{11}$, and As-bearing argentocuprocosalite $(Pb,Cu,Ag)_2Bi_2S_5$ are common/reoccurring discrete mineral phases in low sulfide mineralization (sulbismuthites are noticeably absent in sharp-walled veins) and they present an additional line of first order evidence that low sulfide mineralization records a progressively reducing geochemical system – in contrast to the oxidizing evolution recorded in the sharp-walled veins.

2.7 Conclusions

"High sulfide" sharp-walled veins within the North Range footwall of the Sudbury Igneous Complex (SIC) are characterized by >90% total sulfide minerals that are dominated by chalcopyrite, with lesser and variable Cu-, Ni-, and Fe-sulfides and oxides. In the area of the Coleman Mine, these veins can be further divided into *Ni-rich* (chalcopyrite+pentlandite+millerite+magnetite+sphalerite± pyrrhotite), *Fe-rich* (chalcopyrite+cubanite+pyrite+magnetite+sphalerite+pyrrho-tite±pentlandite), and *bornite-bearing* (bornite+chalcopyrite+millerite) subgroups based on their respective mineralogies. The high precious metal tenors are largely controlled by the presence of (locally) chemically homogeneous composite grains of moncheite $(Pt,Pd)(Te,Bi)_2$ and hessite Ag_2Te, but many other precious metal minerals persist within different sections of the mine. The PGM often exhibit considerable solid solution between Pt-Pd and Te-Bi.

In contrast, "low sulfide" high-PGE blebs, disseminations, and stringers are characterized by <5% total sulfide minerals dominated by bornite, chalcopyrite, and millerite. Low sulfide samples contain PGE/S ratios that can be up to an order of magnitude higher than those in sharp-walled veins (Farrow et al. 2005). At the Coleman Mine, low sulfide occurrences are associated with alteration assemblages that are further subdivided into 3 groups: (1) *calcite-free* (quartz, epidote, chlorite, actinolite, titanite, apatite), (2) *calcite-bearing* (quartz, epidote, calcite, chlorite, titanite, Na-Cl silicate), (3) *garnet-bearing* (quartz, epidote, calcite, garnet, actinolite,

calcic amphibole). The precious metal tenors are controlled by end-member PMM that exhibit no solid solution (between Pt-Pd, Bi-Te, etc.).

Mass balances for Ni in all styles of high sulfide-type mineralization are nearly exclusively covered by pentlandite and millerite in both the 153 and 170 ore bodies. Lead is contained in galena within all high sulfide samples, as well as partly by chalcopyrite, millerite, pentlandite, and/or bornite depending on the respective high sulfide subgroup (i.e. typical sharp-walled veins vs. vein terminations). Platinum is accounted for nearly entirely by the PGM (moncheite, michenerite, merenskyite, sperrylite, nigglite) regardless of the type of high sulfide mineralization in question. Like Pt, the dominant carriers of Pd are the PGM (kotulskite, froodite, paolovite, merenskyite, michenerite, moncheite) in both ore bodies. Pentlandite also contributed small fractions to the Pd mass balances in sharp-walled veins from both ore bodies. The most relevant carriers of Ag in sharp-walled veins are hessite, native silver, electrum, and geffroyite; with notable contributions from pentlandite and chalcopyrite. In the high sulfide bornite-rich sample from the extremities of the 153 vein system, bornite (1120 ppm Ag) accounts for >97% of the Ag mass balance. Gold is distributed between electrum and BMS and oxides (chalcopyrite, pentlandite, millerite, bornite, magnetite) in all high sulfide mineralization styles. It is likely that the domination of BMS to Au mass balances in high sulfide mineralization is a function of the "nugget effect," where electrum is distributed heterogeneously within the veins at the scale of individual thin sections. Tin is variably distributed between paolovite, cassiterite, niggliite, and

BMS/oxides (chalcopyrite, pentlandite, millerite, magnetite) in all samples analyzed except for the high sulfide bornite-rich sample which did not contain discrete Sn phases and its mass balance was covered almost exclusively (>97%) by chalcopyrite (5.77 ppm Sn), with an extremely small Sn contribution (<3%) from bornite (0.071 ppm Sn).

Mass balances for Ni in low sulfide samples are distributed between millerite, parkerite, and chalcopyrite (90.6 ppm Ni). Lead in low sulfide mineralization is accounted for ~100% by galena. The most relevant Pt-carriers in low sulfide samples are moncheite, sperrylite, insizwaite, maslovite, crerarite, and an unnamed $(Pd,Pt)(Bi,Te)_2$ mineral; as well as small contributions from millerite (0.54 ppm Pt) and chalcopyrite (0.012 ppm Pt). Palladium in low sulfide mineralization is controlled by kotulskite, froodite, michenerite, an unnamed $(Pd,Pt)(Bi,Te)_2$ mineral, and moncheite; with small fractions to the Pd mass balance also coming from chalcopyrite, millerite, and bornite. Silver low sulfide budgets are divided between hessite, native silver, electrum, bornite (562 ppm Ag), and chalcopyrite (10.3 ppm Ag). Low sulfide Au mass balances are filled out by electrum, chalcopyrite (0.11 ppm Au), bornite (0.074 ppm Au), and millerite (0.071 ppm Au). Lastly, Sn mass balances for low sulfide mineralization are covered nearly entirely by solid solution in chalcopyrite (10.4 ppm Sn); with minor contributions from bornite (17.3 ppm Sn) and millerite (1.78 ppm Sn). However, Sn-bearing silicates (up to 4.76 wt% Sn) have been observed in low sulfide mineralization in the deep Morrison deposit (Ames poster, open file 7329) and it is possible that they could carry Sn in these samples.

Notable differences exist among certain precious metal bulk rock grades for the different low sulfide alteration styles (calcite-free alteration, calcite-bearing alteration, garnet-bearing alteration) presented in this study. Calcite-bearing alteration has the highest Pt grades (17.0 g/t), followed by calcite-free alteration (6.67 g/t); with garnet-bearing alteration exhibiting remarkably lower bulk rock Pt (0.01 g/t). Bulk rock Pd grades show a similar pattern. Calcite-bearing alteration contains Pd grades of 4.66 g/t, calcite-free alteration grades 2.40 g/t Pd, and garnet-bearing alteration contains Pd grades of 0.22 g/t. Gold exhibits the opposite pattern. Garnet-bearing alteration has the highest Au grades (18.7 g/t); whereas calcite-free alteration and calcite-bearing alteration contain much lower Au grades of 0.94 g/t and 2.03 g/t, respectively.

Systematic mass balance calculations carried out at 1-meter intervals along 10-meters of a sharp-walled vein ("Vein 1") in the 170 ore body address stope-scale ore metal variability. Nickel is constrained to pentlandite and millerite along the entire length of the vein with the rare exception of one pentlandite/millerite-poor sample where chalcopyrite solid solution plays a significant role in hosting Ni. The Pb budget is entirely covered by galena along the length of the vein. Both Pt and Pd are accounted for by PGM and their dominant residence sites do not vary; which are moncheite and michenerite, respectively. The majority of silver is locked up in hessite and native silver along the vein's length, whereas Au predominantly occurs dissolved in chalcopyrite unless any electrum is present. Tin is distributed fairly evenly along the entire vein between cassiterite and chalcopyrite; and sometimes

magnetite. In summary, with respect to the PGM (Pt, Pd) it appears that at the scale of an individual stope there is no significant lateral variation in their residence sites.

High sulfide sharp-walled veins in the 153 and 170 ore bodies at the Coleman Mine represent the residual sulfide melt that separated from earlier-forming MSS cumulates at the base of the SIC and descended into permeable meteorite impact breccias in the footwall. This melt started crystallizing PGE-arsenides, PGE-stannides, and magnetite at high temperatures (>1000°C). Intermediate solid solution (ISS) would crystallize as the temperature dropped below 1000°C, and these assemblages would later exsolve chalcopyrite, pentlandite, millerite, and cubanite when the temperatures dropped to <650°C. Coincident to, or shortly following the crystallization of ISS at 950-800°C, an immiscible Pt-Pd-Ag-Bi-Te melt would separate from the Cu-rich residue and begin crystallizing composite grains of moncheite and hessite. Other precious metal minerals would later exsolve from ISS or crystallize from immiscible semimetal melt in areas of the veins where Pt, Pd, Ag, Bi, and Te availabilities were variable. During the traverse away from the SIC, this Cu-rich residue would progressively oxidize and begin forming selenides (naumannite, geffroyite, clausthalite). This oxidation phenomenon would also cause galena to incorporate substantial Se (replacing sulfur) as the bulk metal/S ratio progressively increased and would cause Cu/Fe ratios to rise to the point where the melt could fractionate past ISS stability and solidify at a Cu-rich thermal minimum where both bornite and millerite could crystallize as equilibrium phases with carbonate – representing the termination of the vein systems. A final low

temperature phenomenon that occurred along most of the veins is the exsolution of a Cl-rich fluid. Evidence for this comes from secondary metal chlorides (cotunnite, chlorargyrite) infilling voids in vein phases, as well as Cl-rich alteration haloes in wallrocks surrounding entire vein systems (Hanley and Mungall 2003).

Low sulfide high-PGE footwall mineralization derives from a hydrocarbon-enriched aqueous fluid that concentrated ore metals from an unidentified source and entered the footwall using some of the same pathways as the sharp-walled veins (cross-cutting relationships around Sudbury suggest that in some areas it entered the footwall prior to mobilization of the Cu-rich residue). As this hydrothermal fluid descended into the footwall and began to cool, it started crystallizing end-member PGE-arsenides, PGE-bismides, PGE-tellurides, and PGE-bismuthotellurides (exhibiting no solid solution). With progressive temperature drops, the fluid became increasingly reducing as it reacted with deep $CaCl_2$-rich ground water and this reduction is recorded in the ore mineralogy of low sulfide samples by the primary presence of sulfbismuthites (parkerite, aikinite, wittichenite, crerarite, As-bearing argentocuprocosalite) that are intergrown with sulfides and hydrothermal silicates/carbonates. The precipitation of calcic silicates and carbonates caused the saturation of the relatively low-temperature paragenetically-late sulfides (bornite, chalcopyrite, millerite) which exhausted the low sulfide fluids of their metal-loads.

2.8 References

Addison WD, Brumpton GR, Vallini DA, McNaughton NJ, Davis DW, Kissin SA, Fralick PW, Hammond AL (2005) Discovery of distal ejecta from the 1850 Ma Sudbury impact event. Geology 33:193-196

Ames DE, Golightly JP, Lightfoot PC, Gibson HL (2002) Vitric compositions in the Onaping Formation and their relationship to the Sudbury Igneous Complex, Sudbury structure. Economic Geology 97:1541-1562

Ames DE, Farrow CEG (2007) Metallogeny of the Sudbury Mining Camp, Ontario. In Goodfellow WD (ed) Mineral deposits of Canada: A synthesis of major deposit-types, district metallogeny, the evolution of geological provinces, and exploration methods. GAC Mineral Deposits Division Special Publication 5:329-350

Ames DE, McClenaghan MB, Averill S (2007) Footwall-hosted Cu-PGE (Au, Ag), Sudbury Canada: Towards a new exploration vector (abs). Fifth Decentennial International Conference on Mineral Exploration, September 2007, Toronto, Canada

Ames DE, Davidson A, Wodicka N (2008) Geology of the giant Sudbury polymetallic mining camp, Ontario, Canada. Economic Geology 103:1057-1077

Ames DE, Kjarsgaard I (2013) Sulfide and alteration mineral chemistry of low- and high-sulphide Cu-PGE-Ni deposits in the footwall environment, Sudbury, Canada. Geological Survey of Canada, Open File 7331, poster. dol:10.4095/292707

Ballhaus C, Tredoux M, Spath A (2001) Phase relations in the Fe-Ni-Cu-PGE-S system at magmatic temperature and application to massive sulfide ores of the Sudbury Igneous Complex. Journal of Petrology 42:1911-1926

Bindi L, Cipriani C (2004) Structural and physical properties of fischesserite, a rare gold-silver selenide from the De Lamar Mine, Owyhee County, Idaho, USA. The Canadian Mineralogist 42:1733-1737

Cabri LJ, Harris DC (1972) The new mineral insizwaite ($PtBi_2$) and new data on niggliite (PtSn). Mineralogical Magazine 38:794-800

Cabri LJ (1973) New data on phase relations in the Cu-Fe-S system. Economic Geology 68:443-454

Cabri LJ, Laflamme JHG (1976) The mineralogy of the platinum-group elements from some copper-nickel deposits of the Sudbury area, Ontario. Economic Geology 71:1159-1195

Card KD (1994) Geology of the Levack Gneiss Complex, the northern footwall of the Sudbury structure, Ontario. Geological Survey of Canada Current Research 1994-C:269-278

Crerar DA, Barnes HL (1976) Ore solution chemistry V. Solubilities of chalcopyrite and chalcocite assemblages in hydrothermal solution at 200° to 350°C. Economic Geology 71:772-794

Dare SAS, Barnes SAJ, Prichard HM, Fisher PC (2011) Chalcophile and platinum-group element (PGE) concentrations in sulfide minerals from the McCreedy East deposit, Sudbury, Canada, and the origin of PGE in pyrite. Mineralium Deposita 46:381-407

Dare SAS, Barnes SJ, Beaudoin G (2012) Variation in trace element content of magnetite crystallized from a fractionating sulfide liquid, Sudbury, Canada: Implications for provenance discrimination. Geochimica et Cosmochimica Acta 88:27-50

Dare SAS, Barnes SJ, Prichard HM, Fisher PC (2014) Mineralogy and geochemistry of Cu-rich ores from the McCreedy East Ni-Cu-PGE deposit (Sudbury, Canada): Implications for the behavior of platinum group and chalcophile elements at the end of crystallization of a sulfide liquid. Economic Geology 109:343-366

Dietz RS (1964) Sudbury structure as an astrobleme. Journal of Geology 72:412-434

Elliot RP (1965) Constitution of binary alloys, 1st supplement. In: Materials science and engineering series: New York. McGraw-Hill Book Co., 877 p.

Farrow CEG, Watkinson DH (1992) Alteration and the role of fluids in Ni, Cu and platinum-group element deposition, Sudbury Igneous Complex Contact, Onaping-Levack area, Ontario. Mineralogy and Petrology 46:67-83

Farrow CEG (1994) Geology, alteration, and the role of fluids in Cu-Ni-PGE mineralization of the footwall rocks to the Sudbury Igneous Complex, Levack and Morgan Townships, Sudbury District, Ontario. Unpublished Ph.D. thesis, Carleton University, Ottawa, Canada, 373 p.

Farrow CEG, Watkinson DH (1996) Geochemical evolution of the Epidote Zone, Fraser Mine, Sudbury, Ontario: Ni-Cu-PGE remobilization by saline fluids. Exploration and Mining Geology 5(1):17-31

Farrow CEG, Watkinson DH (1997) Diversity of precious-metal mineralization in footwall Cu-Ni-PGE deposits, Sudbury, Ontario: Implications for hydrothermal models of formation. The Canadian Mineralogist 35:817-839

Farrow CEG, Lightfoot PC (2002) Sudbury PGE revisited: Toward an integrated model. In: Cabri LJ (ed) The geology, geochemistry, mineralogy and mineral beneficiation of platinum-group elements. Canadian Institute of Mining, Metallurgy and Petroleum Special Volume 54:13-130

Farrow CEG, Everest JO, King DM, Jolette C (2005) Sudbury Cu(-Ni)-PGE systems: Refining the classification using McCreedy West Mine and Podolsky project case studies. In: Mungall JE (ed) Exploration for deposits of platinum-group elements. MAC Short Course Series 35:163-180

Fedorowich JS, Rousell DH, Peredery WV (1999) Sudbury Breccia distribution and orientation in an embayment environment. Geological Society of America Special Paper 339: 305-315

Freidrich K (1907) The binary systems FeS-ZnS and FeS-PbS. Metallurgie 4:479-485 (in German)

Fonseca ROC, Campbell AH, O'Neill HSC, Fitzgerald JD (2008) Oxygen solubility and speciation in sulphide-rich mattes. Geochimica et Cosmochimica Acta 72:2619-2635

Hanley JJ, Mungall JE (2003) Chlorine enrichment and hydrous alteration of the Sudbury Breccia hosting footwall Cu-Ni-PGE mineralization at the Fraser Mine, Sudbury, Ontario, Canada. The Canadian Mineralogist 41:857-881

Hanley JJ, Mungall JE, Pettke T, Spooner ETC, Bray CJ (2005) Ore metal redistribution by hydrocarbon-brine and hydrocarbon-halide melt phases, North Range footwall of the Sudbury Igneous Complex, Ontario, Canada. Mineralium Deposita 40:237-256

Hanley JJ, Ames D, Barnes J, Sharp Z, Guillong M (2011) Interaction of magmatic fluids and silicate melt residues with saline groundwater in the footwall of the Sudbury Igneous Complex, Ontario, Canada: New evidence from bulk rock geochemistry, fluid inclusions and stable isotopes. Chemical Geology 281:1-25

Hansen M, Anderko K (1958) Constitution of binary alloys. In: New-York, McGraw-Hill or Schenectady, New York, General Electric Co., Business Growth Services, 1305 p.

Harney DMW, Merkle RKW (1990) Pt-Pd minerals from the upper zone of the eastern Bushveld Complex, South Africa. The Canadian Mineralogist 28:619-628

Helmy HM, Ballhaus C, Berndt J, Bockrath C, Wohlgemuth-Ueberwasser C (2007) Formation of Pt, Pd and Ni tellurides: experiments in sulfide-telluride systems. Contributions to Mineralogy and Petrology 153:577-591

Hoffman E, MacLean WH (1976) Phase relations of michenerite and merenskyite in the Pd-Bi-Te system. Economic Geology 71:1461-1468

Hutchinson D, McDonald I (2008) Laser ablation ICP-MS study of platinum-group elements in sulphides from the Platreef at Turfspruit, northern limb of the Bushveld Complex, South Africa. Mineralium Deposita 43:695-711

Jago BC, Morrison GG, Little TL (1994) Metal zonation patterns and microtextural and micromineralogical evidence for alkali- and halogen-rich fluids in the genesis of the Victor Deep and McCreedy East footwall copper orebodies, Sudbury Igneous Complex. In: Lightfoot PC, Naldrett AJ (ed) Proceedings of the Sudbury-Noril'sk Symposium. Ontario Geological Survey Special Volume 5:65-90

Kaiser CL, Elliott JF (1986) Solubility of oxygen and sulfur in copper-iron mattes. Metal Mater Trans B 17:147-157

Kerr MJ (2013) The application of gas chromatography in characterizing bulk fluid inclusion hydrocarbons in the footwall of the Sudbury Igneous Complex and other magmatic, hydrothermal and surficial ore-forming environments. Unpublished M.Sc. thesis, Saint Mary's University, Halifax, Canada, 241 p.

Kormos SE (1999) Metal distribution within Zone 39, a Proterozoic vein-type Cu-Ni-Au-Ag-PGE deposit, Strathcona Mine, Ontario, Canada. Unpublished M.Sc. thesis, Laurentian University, Sudbury, Canada, 163 p.

Kosovinc I, Grgasovic T (1972) Phases in ternary Pd-In-Sn alloys at temperatures 900C to 400C. Mining and Metallurgy Quarterly 1:71-77

Kress VC (1997) Thermochemistry of sulfide liquids. I. The system O-S-Fe at 1 bar. Contributions to Mineralogy and Petrology 127:176-186

Kress VC (2000) Thermochemistry of sulfide liquids. II. Associated solution model for sulfide liquids in the system O-S-F. Contributions to Mineralogy and Petrology 139:316-325

Kress VC (2007) Thermochemistry of sulfide liquids. III. Ni-bearing liquids at 1 bar. Contributions to Mineralogy and Petrology 154:191-204

Kretz R (1983) Symbols for rock-forming minerals. American Mineralogist 68:277-279

Krogh TE, Davis DW, Corfu F (1984) Precise U-Pb zircon and baddeleyite ages for the Sudbury area. In: Pye EG, Naldrett AJ, Giblin PE (ed) The geology and ore deposits of the Sudbury structure. Ontario Geological Survey Special Volume 1:431-447

Krogh TE, Corfu F, Davis DW, Dunning GR, Heaman LM (1987) Precise U-Pb isotopic ages of diabase dykes and mafic to ultramafic rocks using trace amounts of baddeleyite and zircon. Geological Association of Canada Special Paper 34:147-152

Lawson WD (1951) A method of growing single crystals of lead telluride and lead selenide. Journal of Applied Physics 22:1444

Legault D, Lafrance B, Ames DE (2003) Structural study of Sudbury breccia and sulphide veins, Levack embayment, North Range of the Sudbury structure, Ontario. Geological Survey of Canada Current Research 2003-C1:1-9

Li C, Naldrett AJ, Coats CJA, Johannessen P (1992) Platinum, palladium, gold and copper-rich stringers at the Strathcona Mine, Sudbury: Their enrichment by fractionation of a sulfide liquid. Economic Geology 87:1584-1598.

Li C, Naldrett AJ (1993) Platinum-group minerals from the Deep Copper Zone of the Strathcona deposit, Sudbury, Ontario. The Canadian Mineralogist 31:31-44.

Lide DR (1998) Handbook of chemistry and physics. 87th edition, Boca Raton, FL, CRC Press: 4-65

Lightfoot PC, Keays RR, Doherty W (2001) Chemical evolution and origin of nickel sulfide mineralization in the Sudbury Igneous Complex, Ontario, Canada. Economic Geology 96:1855-1875

Makovicky M, Makovicky E, Rose-Hansen J (1992) The phase system Pt-Fe-As-S at 850°C and 470°C. Neues Jahrbuch für Mineralogie-Monatshefte 10:441-453

Makovicky E (2002) Ternary and quaternary phase systems with PGE. In Cabri LJ (ed) The geology, geochemistry, mineralogy and mineral beneficiation of platinum-group elements. Canadian Institute of Mining, Metallurgy and Petroleum Special Volume 54: 131-176

Maleviskiy AYA, Yushko-Zakharova OYE, Dubakina LS (1978) Minerals of the series Pt$_3$Sn-Pd$_3$Sn. International Geology Review 20:229-235

McCormick KA, Fedorowich JS, McDonald AM, James RS (2002) A textural, mineralogical, and statistical study of the footwall breccia within the Strathcona Embayment of the Sudbury structure. Economic Geology 97:125-143

Money DP (1993) Metal zoning in the Deep Copper Zone 3700 Level, Strathcona Mine, Ontario. Exploration and Mining Geology 2:307-320

Moretti R, Baker DR (2008) Modelling the interplay of fO$_2$ and fS$_2$ along the FeS-silicate melt equilibrium. Chemical Geology 256:286-298

Morimoto N, Kullerud G (1962) The Mo-S system. Carnegie Institution, Washington. Year B 61:143-144

Morrison GG (1984) Morphological features of the Sudbury Structure in relation to an impact. In: Pye EG, Naldrett AJ, Giblin PE (ed) The geology and ore deposits of the Sudbury Structure. Ontario Geological Survey Special Volume 1:513-520

Morrison GG, Jago BC, White TL (1994) Footwall mineralization of the Sudbury Igneous Complex. In: Lightfoot PC, Naldrett AJ (ed) Proceedings of the Sudbury-Noril'sk Symposium. Ontario Geological Survey Special Volume 5:57-64

Mungall JE, Ames DE, Hanley JJ (2004) Geochemical evidence from the Sudbury structure for crustal redistribution by large bolide impacts. Nature 429:546-548

Naldrett AJ, Kullerud G (1967) A study of the Strathcona Mine and its bearing on the origin of the nickel-copper ores of the Sudbury District, Ontario. Journal of Petrology 8:453-531

Naldrett AJ (1969) A portion of the system Fe-S-O between 900 and 1080°C and its application to sulfide ore magmas. Journal of Petrology 10:171-201

Naldrett AJ (1984) Mineralogy and composition of the Sudbury ores. In: Pye EG, Naldrett AJ, Giblin PE (ed) The geology and ore deposits of the Sudbury structure. Ontario Geological Survey Special Volume 1:309-326

Naldrett AJ, Asif M, Schandl E, Searcy T (1999) Platinum-group elements in the Sudbury ores: Significance with respect to the origin of different ore zones and to the exploration for footwall orebodies. Economic Geology 94:185-210

Nelles EW, Lesher CM, Lafrance B (2010) Mineralogy and textures of Cu–PPGE–Au-rich mineralization in the Morrison (Levack footwall) Deposit, Sudbury, Ontario (abs). SEG 2010 Conference, 2010, Keystone, USA

Nelles EW (2012) Genesis of Cu-PGE-rich footwall-type mineralization in the Morrison Deposit, Sudbury. Unpublished M.Sc. thesis, Laurentian University, Sudbury, Ontario, Canada, 87 p.

Nutt CJ, Hofstra AH (2007) Bald Mountain Gold Mining District, Nevada: A Jurassic reduced intrustion-related gold system. Economic Geology 102:1129-115

Okamoto H (1990) The As-Pt (arsenic-platinum) system. Bulletin of Alloy Phase Diagrams 11:508-510

Okamoto H (1994) The Bi-Pd (bismuth-palladium) system. Journal of Phase Equilibria 15:191-194

Patnaik P (2003) Handbook of Inorganic Chemical Compounds. McGraw-Hill 1086 p.

Péntek A, Molnár F, Watkinson DH, Jones PC (2008) Footwall-type Cu-Ni-PGE mineralization in the Broken Hammer area, Wisner township, North Range, Sudbury structure. Economic Geology 103:1005-1028

Peregoedova A, Ohnenstetter M (2002) Collectors of Pt, Pd and Rh in a S-poor Fe-Ni-Cu sulfide system at 760°C: Experimental data and application to ore deposits. The Canadian Mineralogist 40:527-561

Prichard HM, Knight RD, Fisher PC, McDonald I, Zhou MF, Wang CY (2013) Distribution of platinum-group elements in magmatic and altered ores in the Jinchuan intrusion, China: An example of selenium remobilization by postmagmatic fluids. Mineralium Deposita 48:767-786

Rousell DH (1984) Onwatin and Chelmsford Formations In: Pye EG, Naldrett AJ, Giblin PE (ed) The geology and ore deposits of the Sudbury structure. Ontario Geological Survey Special Volume 1:211-218

Rousell DH, Fedorowich JS, Dressler BO (2003) Sudbury breccia (Canada): A product of the 1850 Ma Sudbury event and host to footwall Cu-Ni-PGE deposits. Earth-Science Reviews 60:147-174

Sinyakova EF, Kosyakov VI (2009) An experimental modelling of primary, secondary and impurity zoning during fractional crystallization of the Cu-Fe-Ni-S-(Pt,Pd) melts. Electronic Scientific Information Journal "Vestnik Otdelenia nauk o Zemle RAN" 1(27):1-3

Skinner BJ, Luce FD, Dill JA, Ellis DE, Hagan HA, Lewis DM, Odell DA, Sverjensky DA, Williams N (1976) Phase relations in ternary portions of the system Pt-Pd-As-S. Economic Geology 71:1469-1475

Springer G (1989) Chlorine-bearing and other uncommon minerals in the Strathcona Deep Copper Zone, Sudbury District, Ontario. The Canadian Mineralogist 27:311-313

Takeno S, Moh GH (1977) Liquidus reactions of the Mo-S system. Neues Jahrbuch für Mineralogie 131:43-48

Tuba G, Molnár F, Watkinson DH, Jones PC, Mogessie A (2010) Hydrothermal vein and alteration assemblages associated with low-sulfide footwall Cu-Ni-PGE mineralization and regional hydrothermal processes, North and East Ranges, Sudbury structure, Canada. SEG Special Publication 15:573-598

Thompson LM, Spray JG (1994) Pseudotachylitic rock distribution and genesis within the Sudbury impact structure. In: Large Meteorite Impacts and Planetary Evolution (ed.) Dressler BO, Grieve RAF, Sharpton VL; Geological Society of America, Special Paper   293:275-288

Voudouris P, Melfos V, Spry PG, Bonsall TA, Tarkian M, Solomos CH (2008) Carbonate-replacement Pb-Zn-Ag±Au mineralization in the Kamariza area, Lavrion, Greece: Mineralogy and thermochemical conditions of formation. Mineralogy and Petrology 94:85-106

White CJ (2012) Low-sulfide PGE-Cu-Ni mineralization from five prospects within the footwall of the Sudbury Igneous Complex, Ontario, Canada. Unpublished Ph.D. thesis, University of Toronto, Toronto, Ontario, Canada, 318 p.

Wiberg E, Wiberg N, Holleman AF (2001) Inorganic chemistry. Academic Press, 1884 p.

Wohlgemuth-Ueberwasser CC, Fonseca ROC, Ballhaus C, Berndt J (2013) Sulfide oxidation as a process for the formation of copper-rich magmatic sulfides. Mineralium Deposita 48:115-127

Yund RA, Kullerud G (1966) The Fe-Pb-S system. Journal of Petrology 7:454-488

Chapter 3: Mineralogical, fluid inclusion, and stable isotope constraints on metal precipitation mechanisms associated with the formation of "low sulfide" hydrothermal Cu-Ni-PGE mineralization within the 153 ore body, Sudbury, Canada

Matthew MacMillan*[1], Jacob Hanley[1], Kevin Neyedley[1], Doreen Ames[2], Chris McFarlane[3], Mostafa Fayek[4], Ryan Sharpe[4]

[1]*Department of Geology, Saint Mary's University, Halifax, NS, Canada*
[2] *Geological Survey of Canada, Ottawa, ON, Canada*
[3]*Department of Earth Sciences, University of New Brunswick, Fredericton, NB, Canada*
[4]*Department of Geological Sciences, University of Manitoba, Winnipeg, MB, Canada*
*corresponding author e-mail address: macmillanmatt41@gmail.com

Abstract

Hydrothermal garnet-bearing alteration assemblages associated with "low sulfide" high-PGE footwall Cu-Ni-PGE mineralization are reported for the first time in a calcite-quartz-garnet-epidote-chlorite-amphibole-sulfide vein from Level 5080 of the Coleman 153 ore body. The garnets have two compositionally-different growth zones (andradite cores, grossular-rich rims) and the sulfide minerals (bornite, chalcopyrite, millerite) are coeval with both the massive calcite (~80 vol%) matrix and the grossular-rich rims on garnet. Fluid inclusions in calcite are two phase L-V and comprise two different populations: (1) 23.65 wt% eq. NaCl and (2) 8.26 wt% eq. NaCl. Homogenization temperatures observed among both populations have an average of 140.2°C and range from 90.1 - 210.0°C. Secondary

ion mass spectrometry analyses (SIMS) of 10 (sulfide-coeval) calcite grains record an average $\delta^{18}O$ value of 5.1 ± 1.2‰, corresponding to calculated $\delta^{18}O$ values (O'Neil et al. 1969) of -4.22‰ and -1.79‰ at 200°C and 250°C for the mineralizing fluid at the time of sulfide precipitation. Shifts towards lighter $\delta^{18}O$ from the paragentically-early garnet cores (10.0 ‰) to the syn-sulfide precipitation rims (4.7 ‰) record progressive interaction with and dilution by ($CaCl_2$-rich) isotopically light North Range groundwater: -10.8 to -10.5‰ (Kaufmann et al. 1987). Recent work (Hanley et al. 2005; Kerr 2013) has shown the fluid associated with low sulfide mineralization to be CH_4-rich and several observations in this study (sulfide/gangue relationships, trace element zoning in garnet, garnet-epidote equilibria considerations, stabilization of sulfbismuthites) suggest this fluid became more reducing over the course of its evolution. The progressive mixing of meteoric groundwater with this hydrocarbon-rich mineralizing aqueous fluid has the ability to achieve carbonate and sulfide precipitation and lower the oxygen fugacity of the system in the process. The calcium-rich alteration assemblage (calcite, garnet, epidote, calcic amphiboles) in the low sulfide package described herein represents an apparent end member to the low sulfide continuum (it has seen the most interaction with $CaCl_2$ groundwater). Low Pt+Pd grades and the lack of Pt- and Pd-PGM in this calcium mineral-rich sample indicates that this fluid dropped out most of its PGE load earlier in its evolution. High Au grades and the presence of primary electrum suggest Au deposition was decoupled with precipitation of the PGM and persisted to the extremities of low sulfide systems.

3.0 Introduction

The North Range of the Sudbury Igneous Complex (SIC) hosts a diverse series of small-volume (relative to other SIC-associated polymetallic deposits) footwall Cu-Ni-PGE mineral deposits that have become increasingly attractive exploration targets over the last decade owing to their anomalously high base metal (Cu, Ni) contents and precious metal tenors. Farrow et al. 2005 subdivided footwall deposits at Sudbury into "high sulfide" (sharp-walled vein) and "low sulfide" (PGE-rich) systems based on their ore mineralogy, alteration mineralogy, and bulk rock chemistry. Both deposit types have garnered significant representation in the literature and current genetic models for their formation attributes the formation of high sulfide mineralization to magmatic/magmatic-hydrothermal processes and/or remobilization by high temperature volatiles (e.g., Li et al. 1992; Naldrett et al. 1999; Péntek et al. 2008; Hanley et al. 2011 etc.) and the formation of low sulfide mineralization to the circulation of metal-bearing hydrothermal fluids (e.g., Péntek et al. 2008; Tuba et al. 2010, 2013; Nelles et al. 2010, White 2012 etc.). Cross-cutting relationships within the 2000 Deposit at the Podolsky Property (Figure 3.1 a) suggest that the formation of low sulfide mineralization preceded high sulfide (Farrow et al. 2005), at least in this area; however, there is still no general characterization of many of the fluid conditions (fluid sources, transport mechanisms, fO_2 of fluids, fluid compositions, etc.) associated with the formation of high-PGE low sulfide-style systems.

Several variations of low sulfide mineralization have been reported in the literature that are distinguished on textural (i.e. veinlets, disseminations, blebs, stringers, etc.) and/or mineralogical (prevalent alteration phases, precious metal mineral assemblages) bases (Farrow et al. 2005; Gibson et al. 2010; Tuba et al. 2010, 2013; Nelles 2012; White 2012; Péntek et al. 2013;). However, common characteristics linking the low sulfide subdivisions are: 1) the presence of <5 volume percent (%) Cu- and Ni-sulfide minerals, (bornite, chalcopyrite, millerite), 2) elevated (up to an order of magnitude higher) bulk rock PGE/S compared to sharp-walled veins, and 3) hydrous alteration assemblages intergrown with the ore phases (sulfide minerals, precious metal minerals). A characteristic alteration mineralogy that prevails in most low sulfide environments comprises quartz+epidote+chlorite assemblages that enclose mineralization; however, more calcic alteration is common with the addition of phases such as calcite and calcic amphibole(s) to the alteration assemblage.

This study uses an alteration assemblage containing hydrothermal garnet (previously unreported in SIC footwall alteration) to constrain fluid conditions associated with the precipitation of low sulfide mineralization in the SIC footwall environment within the 153 ore body at Vale's Coleman Mine.

3.1 Geological setting

The Sudbury Igneous Complex (SIC) is a large (~ 60 km x 30 km), elliptical package of igneous rock that is located near Sudbury, Ontario and cuts the contact between the Superior and Southern Provinces of the Canadian Shield (Figure 3.1 a).

The SIC is a layered igneous body that contains (from bottom up) norite, quartz gabbro, and granophyre sections (Ames et al. 2008); and is widely accepted to be the result of meteorite impact at ~1850 Ma (Krogh et al. 1984). Lithologies stratigraphically above the SIC include crater-fill fallback-breccia and marine sediments that are collectively referred to as the "Whitewater Group" (Rousell, 1984; Ames et al. 2002; Mungall et al. 2004).

World-class mineral deposits of Ni, Cu, and PGE are associated with the SIC and are located both along its base and within its footwall. These deposits are broadly subdivided into 3 distinct ore groups on the basis of both their geological settings and metal contents. *Contact deposits* are Ni-, Ir-, and Rh-enriched ore bodies (compared to the other SIC-associated deposits) that account for >50% of the historical resource of SIC-associated mineral deposits (Lightfoot et al. 2001), and are situated within embayments near the base of the SIC. O*ffset dyke deposits* represent the next most abundant historical resource at Sudbury (Ames and Farrow 2007) and consist of Ni-, Cu-, and precious metal-containing mineral deposits hosted in both radial and concentric quartz diorite offset dykes that splay off the SIC into its surrounding country rock (Lightfoot et al. 2001). *Footwall deposits* account for <10% of Sudbury's historical metal resource (Farrow and Lightfoot 2002), but have become increasingly prospective in recent years (Ames 2007) as a result of their pronounced enrichments in Cu, Pt, Pd, Ag, and Au compared to both contact- and offset dyke-style deposits (Morrison et al. 1994). Pseudotachylitic Sudbury Breccia (described in Chapter 2) is the main host for footwall Cu-Ni-PGE mineralization.

Known footwall deposits are more commonly developed in the North and East ranges at Sudbury and have recently been subdivided into 2 separate mineralization styles: "high sulfide" (sharp-walled vein) and "low sulfide" (high-PGE) (Farrow et al. 2005). Copper-rich sharp-walled veins (predominantly massive chalcopyrite), contain >90% sulfide minerals by volume (away from wallrock contact areas) and can locally reach widths exceeding 1 meter (Farrow et al. 2005). Low sulfide occurrences, like the PM Zone at McCreedy East, contain <5% sulfide minerals by volume (Farrow et al. 2005), that are manifested as blebs, disseminations, and stringers of bornite, chalcopyrite, and millerite; as well as many discrete precious metal mineral phases. Low sulfide deposits are hosted in footwall lithologies developed within the Levack Gneiss Complex (Card 1994) such as Sudbury Breccia, granitoids ranging in composition, or felsic gneiss; but can occur in localized packages of mafic gneiss as well. The low sulfide samples may also be distinguished from high sulfide samples by bulk rock PGE/S values that can be up to an order of magnitude higher than those in high sulfide sharp-walled vein mineralization (Farrow et al. 2005). "Hybrid" footwall Cu-Ni-PGE mineralization is characterized by the presence of both high sulfide sharp-walled vein and low sulfide high-PGE mineralization in the same locality (Farrow et al. 2005).

Low sulfide environments are prevalent within the footwall along the North Range at Sudbury, where they are often spatially associated with high sulfide environments. Perhaps the most notable (and first) low sulfide deposit to be developed in this area is the Sudbury Breccia-hosted "PM Zone." Farrow et al. 2005

summarize resource calculations, structural setting, and overall dimensions of the PM Zone which occupied part of the 153 ore body at the former McCreedy East Mine. Textural variability among low sulfide ores within the PM Zone is also discussed in this study; common characteristics include that low sulfide samples comprise some variation of veins, veinlets, stockworks, blebs, disseminations, or stringers of sulfide minerals (bornite, chalcopyrite, millerite) with associated precious metal minerals that are all intergrown with hydrous alteration characterized by assemblages most commonly dominated by quartz, feldspar, epidote, chlorite, amphibole, and calcite. The low sulfide PM Zone, which is in close proximity to the sharp-walled vein 153 ore body, is now part of Vale's Coleman Mine and its position within the footwall in this area of the North Range relative to other known mineral deposits is illustrated in the longitudinal section presented in Figure 3.1 b.

Previously unreported (among footwall alteration assemblages) hydrothermal garnet has been collected from an approximately 10 cm wide mafic gneiss-hosted sulfide-bearing calcite-quartz-garnet-epidote-chlorite-amphibole vein sampled underground at Level 5080 of the Coleman 153 ore body. The assemblage is used to constrain conditions associated with the precipitation of low sulfide ores in this area of the footwall.

Figure 3.1 (previous page): General geology of the Sudbury Igneous Complex (SIC) and position of the 153 ore body at Vale's Coleman Mine. a) Geological map of the Sudbury Igneous Complex, Sudbury Basin, and associated country rocks. The position of the Coleman Mine is highlighted by a star symbol and the locations of all other known footwall-style deposits and occurrences are indicated as well (Ames and Farrow 2007). b) W-E longitudinal section in the area of the Coleman Mine. The deep 153 is situated furthest away from the SIC relative to other occurrences of mineralization in this area of the SIC footwall (modified from Vale, Coleman Mine).

3.2 Methods

The mafic gneiss-hosted garnet-bearing "low sulfide" alteration assemblage of interest was sampled *in-situ* at Level 5080 (Block 2, Cut 3, ACC) from the 153 ore body (Coleman Mine). This is the deepest and furthest away from the SIC contact of any sample described in this thesis.

Petrography was carried out using a Nikon Eclipse H550L microscope and mineral compositions for silicates, carbonates, sulfides, and discrete heavy metal-bearing phases were determined (semi-) quantitatively using the LEO 1450VP scanning electron microscope (SEM) at Saint Mary's University. The SEM has an attached energy dispersive X-ray (EDS) Oxford INCA 80 mm^2 SDD detector capable of (semi-) quantitative analysis and was operated at a working distance of 20 mm, beam current of 40 μA, and accelerating voltage of 20.00 – 25.00 kV for all analyses. Raw data were reduced using the software package LEO32.

Two-dimensional trace element mapping of 6 garnets was performed at the University of New Brunswick using a Resonetics S-155-LR 193 nm excimer laser coupled to an Agilent 7700x quadrupole ICP-MS. A series of raster scans were carried out on each garnet and subsequently integrated offline into concentration maps using *lolite* software. The standards NIST 612 and BCR-2G were used to calibrate analyte sensitivities and monitor instrumental bias. Calcium (from SEM-EDS) was used for internal standardization. The laser conditions used during all analyses were a spot size of 124 μm, scan speed between 12 to 25 μm/s, and pulse rate of 10 Hz.

Electron microprobe analyses of garnet rims in equilibrium with epidote were carried out using the JEOL 8200 Superprobe at Dalhousie University. All measurements employed an accelerating voltage of 15.0 kV, beam diameter of 1 μm, and 20 seconds/10 seconds for mineral measurements/background measurements on each element, respectively. Standards and crystals used for each measured element were: K (Sanidine, PETJ), Cr (Cr_metal_CH2P, PETJ), Na (Jadeite_Naonly, TAPH), Si (Sanidine, TAP), Mn (PyrolusiteCH5L, LIFH), Ca (K_KaersCaTiMg, PETJ), Ti (K_KaersCaTiMg, PETJ), Mg (K_KaersCaTiMg, TAPH), Al (Sanidine, TAP), Fe (Garnet12442Fe5, LIFH), Ba (Barite_BaCH2P, PETJ), Ni (Ni_metal_CH5L, LIFH), and Zn (Gahnite, LIFH).

Microthermometric analyses were carried out at Saint Mary's University on calcite-hosted fluid inclusions using a Linkam FTIR 600 heating-freezing stage mounted on an Olympus BX51 microscope. Calibration of the stage was accomplished using synthetic fluid inclusion standards containing pure CO_2 (melting at -56.6°C) and pure, critical density H_2O (melting at 0°C and homogenizing at 374.1°C). Absolute uncertainties associated with the measurements (based on measurement reproducibility on standards and measurement precision of the instrumentation) range from ±2-3°C for output temperatures around the extremes of working conditions for the heating-freezing stages (-190°C and 560°C); to better than ±0.2°C for output temperatures near 0°C. Measurements of eutectic (first) ice melting temperatures (T_e^{ice}) were observed to aid in identifying the major cation composition of the respective inclusions. Final ice melting temperatures were used

to calculate NaCl weight percent equivalency values (i.e., bulk salinity) based on the salinity-freezing point depression relationship using the fluid inclusion program *SoWat.*

The oxygen isotopic composition of garnet cores, garnet rims, and calcite were measured using a Cameca IMS 7f secondary ion mass spectrometer (SIMS) at the University of Manitoba. Garnet and calcite crystals were hand-picked, mounted in epoxy resin, and polished using diamond paste to create smooth and even surfaces with exposed mineral grains. Prior to analysis, the samples were thoroughly cleaned using ethanol and a dilute soap solution; then immersed in an ultrasonic bath. The samples were then coated with a thin layer of gold to ensure a conductive surface. Samples were placed in SIMS sample holders and kept under vacuum overnight. A cesium (Cs^+) primary beam with an ~2nA current was accelerated at 8.75kV onto the sample surface with a sputtering diameter of ~15 - 20μm. The instrument operated at a 250V offset, -9kV negative secondary accelerating voltage, and at mass resolving power of 347. During the measurement process by SIMS, an intrinsic mass-dependent bias is introduced, which is referred to as instrumental mass fractionation (IMF) and typically favors the low mass isotope. The greatest contributor to IMF is the ionization process, which depends most strongly upon sample characteristics (i.e., chemical composition) and is routinely referred to as "compositionally-dependent fractionation" or "matrix effects" (e.g., Riciputi et al. 1998). To obtain accurate isotopic SIMS analyses requires that IMF be corrected for by standardizing the IMF using mineral standards

that are compositionally similar to the unknown. SIMS results from the standard are compared to its accepted isotopic composition in order to calculate a correction factor that is applied to the unknowns measured during the same analysis session (e.g., Holliger and Cathelineau 1988). Joplin Calcite, with a $\delta^{18}O_{V\text{-}SMOW}$ value of 5.7‰ (where $\delta^{18}O_{V\text{-}SMOW} = 1.03086*\delta^{18}O_{PDB} + 30.86$) was used for calcite analyses. UWG-2, with a $\delta^{18}O_{V\text{-}SMOW}$ value of 5.8‰ (Valley et al. 1995) was used for both garnet core and garnet rim analyses. However, the composition of UWG-2 ($Alm_{45}Prp_{40}Grs_{14}Sps_1$) does not closely match the compositions of the cores or rims analyzed in this study. The most closely matched garnet standards for the cores and rims of the garnets analyzed herein are 92LEW7 ($Adr_{89}Grs_6Alm_4Prp_1$) and 92LEW10 ($Adr_{50}Grs_{42}Alm_4CaTi_2Prp_2$), respectively. Page et al. 2010 reported average instrumental biases for 92LEW7 and 92LEW10 when corrected using UWG-2 of +6.69‰ and +5.64‰. These additional errors are addressed in the SIMS results section.

Andraditic garnet was also separated from a representative sample of *contact ore* sampled within the "Epidote Zone" at the Fraser Mine (Farrow 1994) and its oxygen isotopic composition was analyzed at Queen's University. Oxygen was extracted using a conventional bromine pentafluorine extraction line, with the isotopes measured on a Finnigan Mat 252 isotope ratio mass spectrometer. Analytical uncertainty was ±0.3‰ (K. Klassen, pers. commun.).

3.3 Results

3.3.1 Petrography and chemistry of (garnet-bearing) "low sulfide" vein

Samples of interest derive from an approximately 10 cm-wide mafic gneiss-hosted individual sinuous vein that contains visible sulfide mineralization (Figure 3.2 a). The vein is characterized by >80 volume percent (%) calcite+quartz matrix (predominantly calcite) that contains paragenetically early garnet crystals as well as interstitial assemblages of granular epidote, foliated chlorite, acicular amphibole, and rutile. Modal abundances (vol%) for these minerals in thin section are as follows: 79% calcite, 6% garnet, 6% chlorite, 5% epidote, 2% quartz, <1% amphibole, and <1% rutile (+enclaves of altered wallrock). Several calcite and garnet grains contain mm-scale (1 - 6 mm) diameters whereas the remaining gangue phases are fine (micron scale). SEM-EDS analyses of the garnets reveal large cores of andradite ($Ca_3Fe_2Si_3O_{12}$) enveloped by thin rims that are richer in the grossular ($Ca_3Al_2Si_3O_{12}$) component of garnet (Figure 3.2 d, e, f). The amphiboles are stoichiometric actinolite or another calcic amphibole (not actinolite or tremolite). Early xenocrystic inclusions of clinopyroxene (augite) are disseminated in andraditic cores of garnet crystals and several examples of garnet-epidote equilibrium (Figure 3.2 c, e) are evident where primary contacts between granular epidote and grossular-rich rims exist.

The sulfides bornite, chalcopyrite, and millerite occur as primary blebs, disseminations, and stringers within calcite-quartz matrix (often spatially associated with epidote, chlorite, amphibole) and also as primary inclusions in the

115
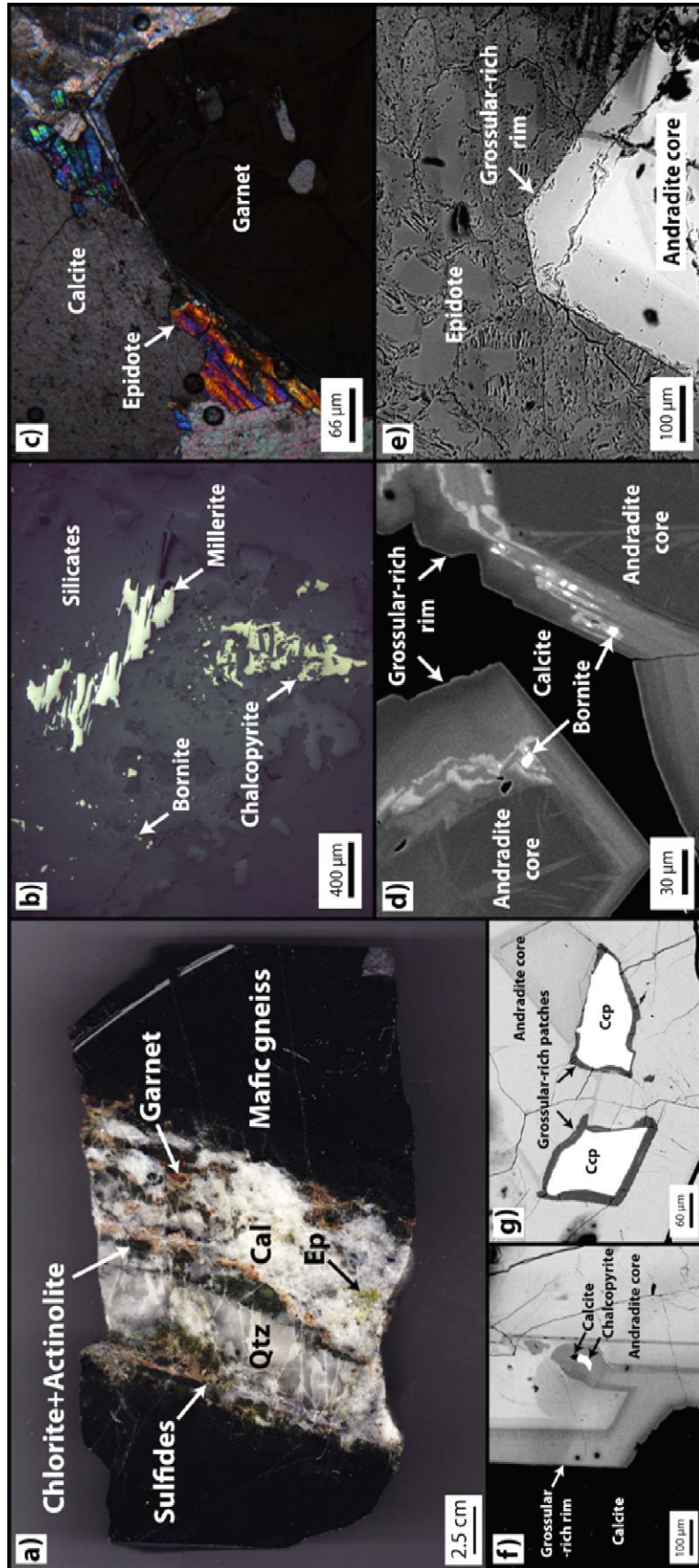
Figure 3.2 (previous page): Mineralogical characteristics of hydrothermal garnet-bearing "low sulfide" mineralization. See digital appendix for sample numbers associated with each image. a) Chip sample from vein showing a calcite-quartz matrix hosting garnet crystals and patches of epidote, amphibole, chlorite and sulfides. b) Calcite-hosted garnet in equilibrium with granular epidote. XPL. c) Disseminations of bornite and networks of chalcopyrite and millerite within silicate host. d) Patches of epidote and chlorite along garnet rims; all of which are hosted in calcite. e) Inclusions of calcite and chalcopyrite within grossular-rich rim of a calcite-hosted garnet crystal. The core is of andraditic composition. f) Chalcopyrite inclusions contained in grossular-rich patches within the andradite core of a garnet crystal. g) Euhedral garnet crystal (grossular-rich rim/andradite core) in equilibrium with granular epidote. h) Bornite inclusions hosted in grossular-rich rims of 2 andraditic garnets. Garnets are hosted in calcite.

grossular-rich rims on garnet crystals or in grossular-rich "patches" that are present within the andradite cores (Figure 3.2 g). Blebs and trails of these sulfide minerals occupy cracks and voids within andradite cores of the garnet crystals; however they are secondary inclusions. The discrete, heavy metal-bearing phases identified in this vein are Bi-bearing millerite (<8 at% Bi), cassiterite (hosted in rutile), electrum (hosted in epidote and chalcopyrite), hessite (hosted in chalcopyrite), native zinc (hosted in calcite), tenorite (hosted in rutile), and an unknown Ni-Mo-Bi mineral (hosted in chalcopyrite and millerite). Precious metal minerals were not found as primary inclusions within any sections of the garnet crystals and no platinum group minerals were identified in this sample. Representative SEM-EDS analyses of andradite cores and grossular-rich rims across 15 garnets are presented in Table 3.1. The average Fe-rich core composition is $Adr_{83.35}Alm_{13.81}Grs_{2.48}Prp_{0.35}Sps_{0.01}$ (n = 169), whereas the average Al-rich rim composition is $Adr_{53.54}Grs_{32.60}Alm_{13.78}Sps_{0.09}$ (n = 25). Table 3.2 and 3.3 provide electron microprobe analyses of 38 garnet rim-epidote equilibrium pairs.

3.3.2 Trace element zoning across garnets and implications for fluid conditions

Major, minor, and trace element LA-ICPMS mapping (raster sequences) of 6 individual garnets was carried out at the University of New Brunswick in 2013 for Fe, Al, Ca, Si, Mg, Mn, Na, La, Ce, Eu, Sm, Nd, Yb, Lu, Hf, Sn, Bi, Pb, Ni, Cu, Ag, Au, Pt, and Pd. As expected, Fe and Al zonation patterns corresponded accurately with the large andradite cores and thin grossular-rich rims that were identified via SEM-EDS. The precious metals (Ag, Au, Pt, Pd) showed negligible variation and were mapped

118

Table 3.1: Representative SEM-EDS analyses of cores and rims from 15 garnets in hydrothermal garnet-bearing "low sulfide" mineralization.

	SiO_2	CaO	FeO	Al_2O_3	MgO	MnO	Na_2O	K_2O	Composition	Core/Rim
					Weight Percent %					
A1	40.713	32.338	26.038	0.093	0.492	0	0.172	0.1	$Adr_{84.54}Alm_{13.10}Prp_{1.80}Grs_{0.56}$	Core
A2	40.928	32.525	26.33	0.1142	0.1033	0	0	0	$Adr_{84.44}Alm_{14.48}Grs_{0.71}Prp_{0.38}$	Core
A3	40.272	32.831	26.797	0.102	0	0	0	0	$Adr_{86.74}Alm_{12.65}Grs_{0.60}$	Core
A4	40.918	32.686	26.324	0	0	0	0.0708	0	$Adr_{85.59}Alm_{14.41}$	Core
A5	40.756	32.714	25.496	1.0313	0	0	0	0	$Adr_{79.80}Alm_{13.99}Grs_{6.21}$	Core
A6	40.758	32.953	26.29	0	0	0	0	0	$Adr_{86.62}Alm_{13.38}$	Core
A7	40.943	32.424	26.454	0	0.1263	0.0538	0	0	$Adr_{84.85}Alm_{14.58}Prp_{0.46}Sps_{0.11}$	Core
B1	40.352	33.014	26.633	0	0	0	0	0	$Adr_{87.66}Alm_{12.34}$	Core
B2	40.417	32.944	26.64	0	0	0	0	0	$Adr_{87.33}Alm_{12.67}$	Core
B3	40.823	32.789	26.239	0.1492	0	0	0	0	$Adr_{85.13}Alm_{13.94}Grs_{0.92}$	Core
B4	40.924	32.714	26.363	0	0	0	0	0	$Adr_{85.65}Alm_{14.35}$	Core
B5	41.31	32.608	25.984	0.0988	0	0	0	0	$Adr_{83.94}Alm_{15.43}Grs_{0.64}$	Core
B6	41.034	32.61	26.203	0.059	0	0	0	0	$Adr_{84.77}Alm_{14.85}Grs_{0.37}$	Core
B7	40.718	32.762	26.517	0	0	0	0	0	$Adr_{86.21}Alm_{13.79}$	Core
C1	40.914	32.743	26.266	0	0.0756	0	0	0	$Adr_{85.74}Alm_{13.98}Prp_{0.28}$	Core
A1	40.875	33.49	16.665	8.965	0	0	0	0	$Grs_{47.54}Adr_{40.24}Alm_{12.22}$	Rim
A2	41.91	32.64	13.23	12.22	0	0	0	0	$Grs_{64.86}Adr_{18.58}Alm_{16.56}$	Rim
A3	40.545	33.41	18.85	6.955	0	0.24	0	0	$Adr_{51.01}Grs_{37.27}Alm_{11.21}Sps_{0.5}$	Rim
A5	42.97	31.72	14.55	10.3	0	0	0	0	$Grs_{62.66}Alm_{20.91}Adr_{16.43}$	Rim
A6	41.005	33.815	16.08	9.105	0	0	0	0	$Grs_{48.86}Adr_{39.49}Alm_{11.65}$	Rim
B2	41.31	33.46	18.07	7.15	0	0	0	0	$Adr_{46.33}Grs_{40.45}Alm_{13.22}$	Rim
B4	40.81	33.21	20.04	5.94	0	0	0	0	$Adr_{54.25}Grs_{32.94}Alm_{12.81}$	Rim
B6	40.783	32.963	16.897	8.77	0	0.1867	0.31	0	$Grs_{46.72}Adr_{39.88}Alm_{13.01}Sps_{0.39}$	Rim
B7	41.58	32.8	18.6	7.02	0	0	0	0	$Adr_{44.31}Grs_{40.21}Alm_{15.48}$	Rim

Table 3.2: EMP analyses of garnet rims in equilibrium with epidote.

Sample				Weight Percent (%)										
Sample	K_2O	Cr_2O_3	Na_2O	SiO_2	MnO	CaO	TiO_2	MgO	Al_2O_3	FeO	BaO	NiO	ZnO	Total
1Grt_1	0.018	0	0.009	37.18	0.209	35.635	0	0.019	8.481	18.005	0	0.014	0	99.57
1Grt_2	0.014	0.009	0	37.155	0.234	35.829	0	0.017	8.653	17.733	0	0	0.065	99.709
1Grt_3	0.013	0	0	36.942	0.196	35.846	0	0.031	8.378	17.818	0	0	0.002	99.226
1Grt_4	0.013	0.002	0.001	37.292	0.184	35.661	0	0.014	8.017	18.006	0	0.001	0.024	99.215
1Grt_5	0.028	0	0.009	36.478	0.248	35.718	0	0.022	7.902	18.282	0	0.01	0	98.697
1Grt_6	0.015	0	0	35.671	0.221	35.464	0	0.019	7.867	18.053	0	0.017	0.047	97.374
1Grt_7	0.019	0	0	36.301	0.245	35.92	0	0.037	8.513	17.529	0	0.029	0.019	98.612
1Grt_8	0.019	0	0	36.368	0.222	35.916	0	0.014	7.894	18.114	0	0	0.014	98.561
1Grt_9	0.01	0.014	0	37.062	0.242	35.653	0	0.025	7.908	18.022	0	0	0.037	98.973
1Grt_10	0.007	0	0.005	35.715	0.235	35.542	0	0.018	7.84	18.646	0	0	0	98.008
2Grt_1	0.011	0	0	37.634	0.23	35.664	0.037	0.04	8.27	17.598	0	0.037	0	99.521
2Grt_2	0.029	0	0	36.971	0.237	36.07	0.075	0.035	8.539	17.532	0	0	0.017	99.505
2Grt_3	0.01	0	0	36.977	0.238	35.794	0.083	0.045	8.4	17.484	0	0	0.012	99.043
2Grt_4	0.001	0	0	37.283	0.26	35.481	0.066	0.049	8.681	16.82	0	0.037	0	98.678
2Grt_5	0.012	0	0	37.244	0.264	35.558	0.077	0.029	8.682	17.048	0	0	0.038	98.952
2Grt_6	0	0.003	0.003	36.621	0.255	35.672	0.064	0.055	8.757	17.143	0	0	0	98.573
2Grt_7	0.024	0.04	0	37.093	0.228	35.577	0.042	0.044	8.399	17.142	0	0.008	0.015	98.612
2Grt_8	0.026	0	0	35.831	0.214	35.532	0	0.038	8.629	17.172	0	0.034	0	97.476
2Grt_9	0.006	0.009	0	37.322	0.239	35.417	0.027	0.03	8.885	16.671	0	0	0	98.606
2Grt_10	0.017	0	0	36.972	0.249	36.061	0.055	0.048	8.847	16.906	0	0	0	99.155
3Grt_1	0.002	0	0	37.454	0.231	35.475	0	0.023	8.804	16.866	0.053	0.024	0	98.932
3Grt_2	0.01	0.032	0	35.848	0.192	35.679	0	0.017	8.978	16.999	0	0.002	0.039	97.796
3Grt_3	0.009	0	0	36.777	0.26	35.542	0.009	0.016	9.215	16.65	0	0	0.012	98.49
3Grt_4	0	0.001	0	36.876	0.248	35.763	0	0.029	8.884	16.844	0	0	0	98.645
3Grt_5	0.002	0.006	0	37.379	0.238	35.443	0	0.04	8.935	16.755	0.006	0.015	0	98.819
3Grt_6	0.019	0	0.011	37.434	0.289	34.811	0	0.027	9.026	16.569	0	0	0	98.186
4Grt_1	0.002	0	0	36.686	0.237	35.622	0	0.025	8.893	16.983	0	0.001	0.002	98.451
4Grt_2	0.015	0	0	36.138	0.21	35.769	0	0.03	8.955	17.054	0	0	0.041	98.212
4Grt_3	0.005	0	0.007	36.701	0.23	35.734	0	0.041	8.913	16.858	0	0	0	98.489
4Grt_4	0.005	0	0.005	36.237	0.258	35.544	0	0.04	8.588	17.274	0	0.006	0	97.957
4Grt_5	0.03	0.028	0.001	35.105	0.186	35.847	0	0	9.196	16.764	0	0	0	97.157
4Grt_6	0.025	0.014	0.001	36.809	0.236	35.451	0	0.039	8.173	17.711	0	0.013	0	98.472
5Grt_1	0.015	0	0	36.602	0.261	35.5	0	0.038	8.416	17.508	0	0.011	0	98.351
5Grt_2	0.024	0	0	36.92	0.237	35.271	0	0.051	8.059	17.753	0	0	0	98.315
5Grt_3	0.002	0	0.012	35.935	0.206	35.659	0	0.028	8.491	17.391	0	0	0	97.724
5Grt_4	0.016	0	0	37.363	0.241	35.019	0	0.027	8.613	17.051	0.025	0	0.024	98.379
5Grt_5	0.013	0	0	37.081	0.28	35.484	0	0.012	9.001	16.986	0	0.001	0.039	98.897
5Grt_6	0.017	0	0.01	36.107	0.277	35.552	0	0.03	8.791	17.156	0	0.03	0.052	98.022

Table 3.3: EMP analyses of epidote in equilibrium with garnet rims.

						Weight Percent (%)								
Sample	K$_2$O	Cr$_2$O$_3$	Na$_2$O	SiO$_2$	MnO	CaO	TiO$_2$	MgO	Al$_2$O$_3$	FeO	BaO	NiO	ZnO	Total
1Ep_1	0	0.003	0	38.112	0.052	24.141	0	0	25.836	9.617	0	0	0	97.761
1Ep_2	0.013	0	0.001	36.063	0.045	24.588	0	0	25.07	9.947	0.04	0.014	0	95.781
1Ep_3	0.024	0	0.02	35.165	0.05	23.193	0.024	0	20.483	13.136	0	0	0.052	92.147
1Ep_4	0.018	0	0.014	35.924	0.101	23.578	0	0	21.695	12.037	0	0	0.042	93.409
1Ep_5	0.004	0	0.013	37.054	0.037	24.155	0	0	25.201	9.438	0	0	0	95.902
1Ep_6	0.017	0.019	0.007	37.647	0.013	24.233	0	0.007	22.712	12.764	0	0.017	0	97.436
1Ep_7	0.015	0	0	38.556	0.025	24.22	0	0.019	24.971	10.371	0	0	0	98.177
1Ep_8	0.006	0	0.006	37.663	0.056	23.497	0	0.586	24.43	10.254	0	0.018	0.028	96.544
1Ep_9	0.037	0.027	0.034	35.73	0.08	23.641	0	0.019	23.434	10.599	0	0	0	93.601
1Ep_10	0.019	0	0.009	37.097	0.022	24.188	0	0.004	25.078	9.265	0	0.028	0.034	95.744
2Ep_1	0.014	0.02	0	36.963	0.029	24.112	0	0.021	22.553	12.231	0	0	0	95.943
2Ep_2	0.022	0	0.004	37.669	0.021	23.978	0	0.021	22.861	12.133	0	0.023	0	96.732
2Ep_3	0.015	0.002	0	37.638	0.01	24.048	0.007	0.014	22.857	12.494	0	0	0	97.085
2Ep_4	0.013	0.005	0.018	40.019	0.045	23.718	0.055	0	26.017	9.026	0.067	0.004	0.069	99.056
2Ep_5	0.004	0.014	0.016	37.587	0.078	22.043	0	1.228	24.499	9.68	0	0.019	0.019	95.187
2Ep_6	0.012	0.014	0	38.168	0.066	23.936	0	0.044	23.099	12.052	0	0.012	0.08	97.483
2Ep_7	0.029	0.027	0	37.845	0.021	24.066	0	0.069	23.76	11.572	0.001	0	0.008	97.398
2Ep_8	0.008	0.015	0	36.508	0.043	23.896	0.019	0.027	22.796	11.965	0	0	0.065	95.342
2Ep_9	0.021	0.002	0	37.383	0.02	24.085	0	0.038	23.313	12.005	0	0.005	0.018	96.89
2Ep_10	0.016	0	0	36.446	0.011	24.204	0	0	22.674	12.3	0	0.002	0.022	95.675
3Ep_1	0.03	0.013	0	35.402	0.009	24.197	0	0.112	21.938	11.998	0	0.043	0	93.742
3Ep_2	0.018	0.032	0.006	38.515	0.016	24.135	0	0.003	23.542	11.914	0	0.006	0	98.187
3Ep_3	0.026	0.011	0.006	38.023	0.031	24.158	0	0.031	24.128	10.689	0	0.025	0	97.128
3Ep_4	0.016	0	0.01	38.211	0.059	23.877	0	0.028	24.262	9.944	0	0.009	0.042	96.458
3Ep_5	0.012	0	0.009	38.637	0.007	23.443	0	0.007	25.506	8.908	0	0	0.033	96.562
3Ep_6	0	0	0.004	37.691	0.052	24.251	0	0.05	25.052	9.585	0	0.01	0.008	96.703
4Ep_1	0.015	0	0.008	37.744	0.027	24.063	0	0.004	25.478	9.688	0	0	0.004	97.031
4Ep_2	0.01	0	0.008	38.047	0.03	24.169	0	0	23.736	11.608	0	0.038	0.048	97.694
4Ep_3	0.025	0	0	36.876	0.012	24.319	0	0.024	23.53	11.725	0	0.002	0	96.513
4Ep_4	0.011	0.016	0	36.307	0.016	24.081	0	0.023	22.926	12.127	0	0	0	95.507
4Ep_5	0.005	0	0	37.661	0.037	24.138	0	0.018	23.024	12.077	0	0.016	0.048	97.024
4Ep_6	0.014	0.035	0.011	37.77	0.008	24.009	0	0	22.613	12.882	0	0.048	0.026	97.416
5Ep_1	0.002	0.002	0.012	37.188	0.015	24.303	0	0.019	24.1	11.291	0	0	0	96.932
5Ep_2	0.011	0	0.006	37.693	0.059	24.018	0	0.019	23.315	11.946	0	0	0	97.067
5Ep_3	0.011	0.001	0	38.527	0	23.967	0	0	23.902	11.415	0	0.015	0.007	97.845
5Ep_4	0.014	0	0	36.839	0.022	24.217	0	0.036	23.207	11.931	0	0.012	0	96.278
5Ep_5	0.011	0	0.004	38.031	0.026	23.716	0	0.02	23.535	11.997	0	0.014	0.026	97.38
5Ep_6	0.03	0	0.017	38.557	0.027	23.415	0	0.346	23.972	11.192	0	0.005	0	97.561

using ppb-range detection limits for the largest garnet that was analyzed. However, 6 components (Mn, Sn, Ce, Nd, Eu, Eu*) showed considerable zonation that supports the hypothesis that an influx of an increasingly reducing fluid was responsible for the rim formation and contemporaneous sulfide precipitation surrounding the oxidized andraditic cores. These 6 components are each discussed separately below and their corresponding LA-ICPMS maps are presented in Figure 3.3.

Mn: Manganese displays distinct zoning across all 6 garnets where it is present in relatively uniformly low concentrations throughout the regions corresponding to the andradite cores and jumps to notably higher concentrations in the regions corresponding to the grossular-rich rims. (Figure 3.3). It can be inferred that the Mn enrichment in the rims may be a consequence of progressive reduction of the hydrothermal fluid during rim-formation. Reduction of Mn from being dominantly trivalent (3^+) to divalent (2^+) would make Mn more compatible in the garnet structure (Jamtveit et al. 1995). Einaudi et al. (1981) deomonstrated skarn garnets to be Mn-enriched when formed from relatively reducing fluids and Mn-depleted when formed from relatively oxidizing fluids.

Sn: Two important observations can be deduced from the Sn zoning patterns across the garnets. The first observation is that (opposite to Mn), Sn concentrations in all garnets become much lower in the areas corresponding to the grossular-rich rims relative to the areas corresponding to the andradite cores (Figure 3.3). The second is observed on the largest garnet (~6 mm) (Figure 3.3, C1); a third zone of notable relative Sn-enrichment (~400 – 500 ppm Sn) exists in the very center of the

122

andradite cores (its outlines are well constrained to the andradite cores and do not approach contact with the grossular-rich rims). Based on the ionic radii of Sn^{4+} and Sn^{2+}, it is expected that Sn^{4+} is more compatible in andradite-grossular garnets. The ionic radius of Sn^{2+} is too large to be incorporated in the Fe^{3+} or Al^{3+} sites in andradite and grossular (Mulholland, 1984).

Ce: Unfortunately, only 3 of the 6 log maps for Ce were able to be accurately produced in this study (Figure 3.3). However, it can be seen that the Ce concentration is relatively much higher in the areas corresponding to the andradite cores and drops to much lower values in areas corresponding to the grossular-rich rims. Cerium is only one of two REE that can take on more than solely trivalent (3$^+$) oxidation states under terrestrial magmatic conditions; it can also occur as Ce^{4+} (Berry et al. 2013). Ce^{4+} is stable in relatively oxidizing environments and it is therefore inferred that that the drop in Ce concentration along the rims of these garnets reflects a drop in the Ce^{4+}/Ce^{3+} ratio as a consequence of increasingly reducing fluid conditions.

Nd: Neodymium variation across all garnets is much less pronounced relative to the other 5 components discussed in this section. It appears that Nd concentrations are similar in both the areas corresponding to the andradite cores and the areas corresponding to the grossular-rich rims. However, as best seen in the largest garnet C1 (but present in 4/5 garnets), there appears to be a transient Nd anomaly at the onset of grossular-rich rim growth. The less drastic zoning in Nd

compared to the other components says little about the redox state of the system as it is a monovalent REE (3^+).

Eu: Europium shows zoning patterns across 4/6 garnets that are characterized by relatively lower Eu concentrations in the areas corresponding to the andradite cores and higher Eu concentrations for the majority of areas corresponding to the grossular-rich rims (Figure 3.3). Most maps also show that Eu concentrations drop again in a small section along the outermost part of the grossular-rich rims. Europium is the other REE (besides Ce) that can take on more than solely trivalent (3^+) oxidation states under terrestrial magmatic conditions; it can also occur as Eu^{2+} (Berry et al. 2013). With that in mind, the increase in Eu concentrations at the onset of grossular-rich rim growth likely reflects an increase in REE concentration of the fluid at this point in the evolution of the system (Eu^{2+} less compatible in garnet).

Eu*: The Eu-anomaly (Eu* = Eu/[0.5*(Sm+Gd)]) was also mapped for the largest garnet C1 (Figure 3.3). There is a very clear (~1 order of magnitude) drop in the magnitude of the Eu-anomaly at the onset of grossular-rich rim growth. If reducing conditions persisted at the point of grossular-rich rim formation, the nature of Eu in solution would inevitably evolve to a state where Eu^{2+}/Eu^{3+} was raised, and the concentration of Eu relative to the monovalent REE that was incorporated in garnet could decrease since Eu^{2+} is less compatible in garnet.
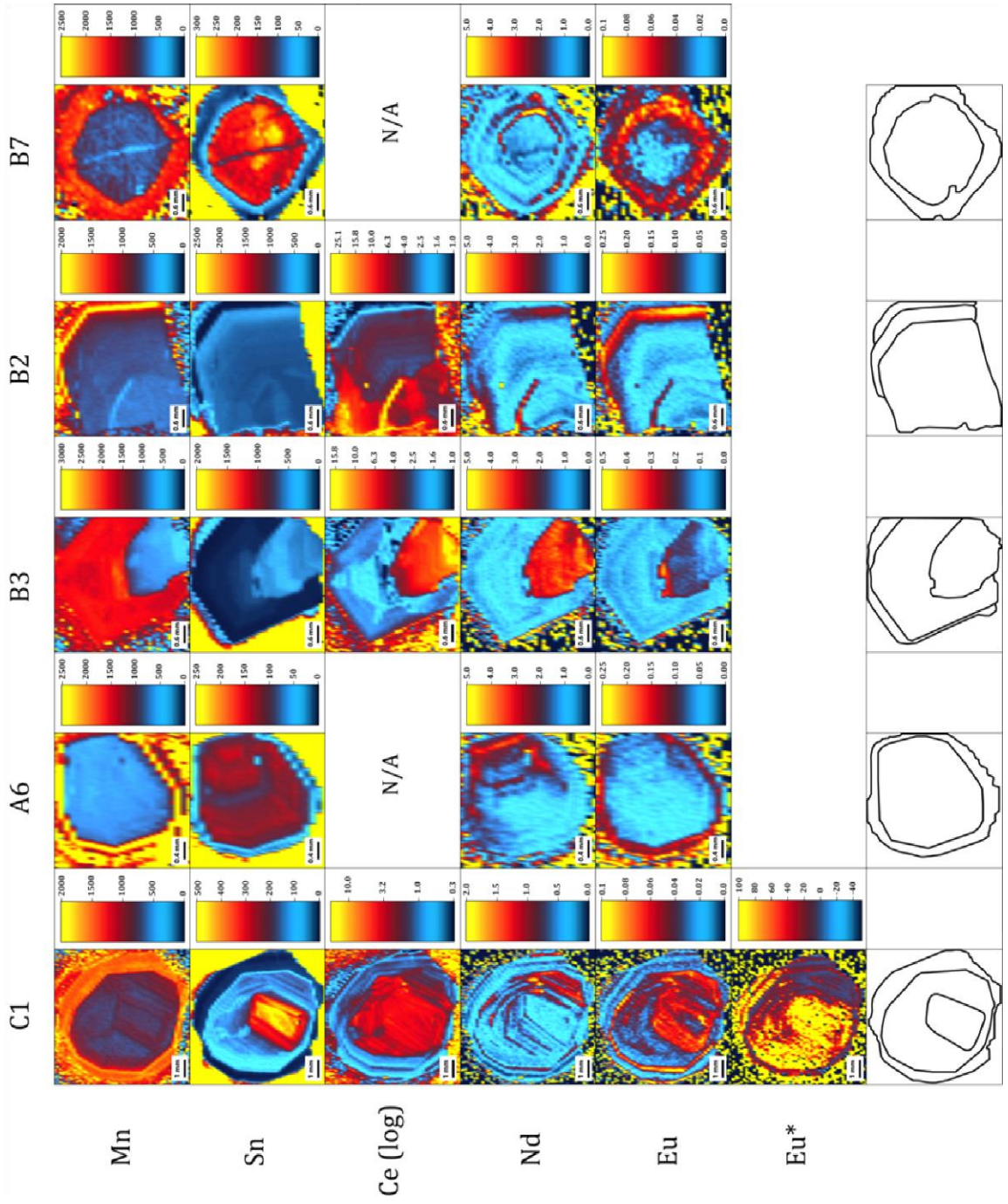
Figure 3.3: Laser ablation trace element maps for Mn, Sn, Ce, Nd, and Eu from 5 garnets (C1, A6, B3, B2, B7) analyzed in this study. The Eu anomaly (Eu* = Eu/[0.5*(Sm+Gd)]) was also mapped on the largest garnet (C1). N/A = not available. All concentration values [Mn, Sn, Ce (log), Nd, Eu] are reported in ppm. See digital appendix for supplementary data.

Marked differences in trace element concentrations between andradite cores and grossular-rich rims are illustrated in Figure 3.4 a. All garnet concentrations are normalized to bulk continental crust using values from Rudnick and Gao (2003) since the initial Sudbury melt had a bulk composition similar to continental crust (Ames et al. 2002; Dare et al. 2012). Grossular-rich rims are enriched in Ni, Cu, Pt, Pd, Ag, Au, and Pb relative to andradite cores within all garnets analyzed. The rare earth elements (REE) show considerable overlap between the two compositional domains in garnet. However, La and Ce tend to be more enriched in the cores whereas Sm tends to be more enriched in the rims. The remaining REE plotted (Nd, Eu, Yb, Lu) are (for the most part) more similar in their concentrations between the andradite cores and grossular-rich rims. Differences in REE concentrations between the cores and rims of the garnets analyzed in this study could also highlight the differential incorporation of REE in garnet as a function of its major element composition and not just due to fluctuations in REE concentrations of the garnet-forming fluid. Recent studies have shown that grossular-rich garnet tends to incorporate heavy REE (HREE) to a greater extent than andradite-rich garnet (Gaspar et al. 2008; Dziggel et al. 2014). The REE (La, Ce, Nd, Sm, Eu, Yb, Lu) concentrations in garnet are also displayed relative to REE concentrations in garnets from other mineralized and barren environments from around the world (Figure 3.4 b, Figure 3.5).
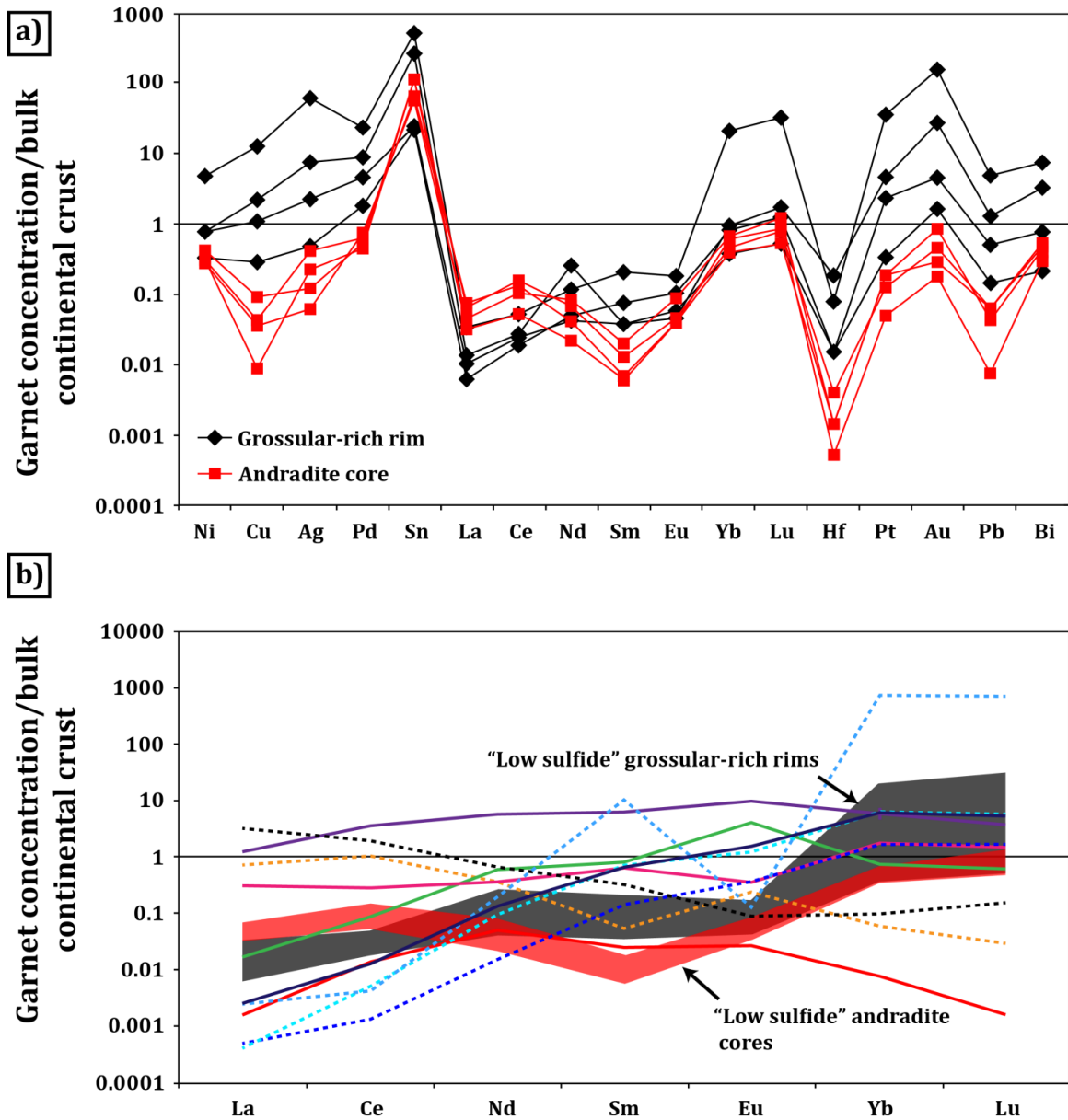
Figure 3.4: Trace element variation in garnet associated with "low sulfide" mineralization. See digital appendix for supplementary data. a) Variation in selected trace element concentrations from andradite cores and grossular-rich rims on 4 garnets. All analyses are normalized to bulk continental crust using values from Rudnick and Gao (2003). b) Variation in selected rare earth element concentrations from the 4 garnets in (a); as well as garnets from several different geological environments (see legend Figure 3.5). All analyses are normalized to bulk continental crust using values from Rudnick and Gao (2003).

Mineralization-associated garnets

Sudbury footwall

- ■ "Low sulfide" grossular-rich rims ($Adr_{54}Grs_{33}Alm_{14}$)
- ■ "Low sulfide" andradite cores ($Adr_{83}Alm_{14}Grs_2$)

Skarns

- — Reduced Au skarn ($Adr_{48}Grs_{48}Alm_3$), Crown Jewel Au deposit, Washington, USA (Gaspar et al. 2008)
- — Zn-Cu-Pb skarn ($Adr_{74}Grs_{23}$), Redcap Deposit, Chillagoe District, Australia (Lehrmann 2012)
- — Xieertala Fe-Zn skarn deposit ($Adr_{88}Grs_4Alm_4Sps_3Prp_1$), Great Hinggan Range, China (Zhai et al. 2014)

Porphyries

- — Central Zone Alkalic Cu-Au Porphyry Deposit ($Adr_{75}Grs_{17}$), British Columbia, Canada (Micko 2005)

SEDEX-type

- — Broken Hill Pb-Zn-Ag Deposit ($Sps_{43}Alm_{26}Grs_{26}Prp_5$), Australia (Spry et al. 2007)

Garnets in barren environments

Contact metamorphic

- --- Beinn an Dubhaich granite aureole ($Adr_{94}Grs_5Prp_1$), Isle of Skye, Scotland (Smith et al. 2004)

Barren skarns

- --- Calc-silicate skarn ($Adr_{99.8}$), Namgar Mine, Erongo Mountains, Damaraland, Namibia (Bocchio et al. 2010)

Primary igneous

- --- Granitic pegmatite ($Sps_{62}Alm_{29}Prp_2$), Evje-Iveland pegmatite field, Norway (Müller et al. 2012)
- --- Andesite (Alm_{61-69}), Northern Pannonian Basin, Hungary/Slovakia (Harangai et al. 2001)
- --- Garnet lherzolite ($Prp_{74}Alm_{14}Grs_{12}$), Vitim volcanic province, Lake Baikal, Siberia (Ionov 2004)

Figure 3.5: Legend for Figure 3.4.

3.3.3 Fluid inclusion characteristics of calcite and garnet

Classification of fluid inclusion origin and classification of inclusion types was based on petrographic observations at room temperature using criteria from Wilkinson (2001) and Goldstein (2003). Fluid inclusions are grouped into fluid inclusion assemblages ("FIA") on the basis of microthermometric behavior, phase ratios, and the occurrence of groups of inclusions along single and readily identifiable growth features (e.g., growth zones, healed fractures, etc.). Classifying fluid inclusion assemblages in this manner helps to differentiate those inclusions that may have experienced necking down or other post-entrapment phenomena from those inclusions that have been unaffected since the time of entrapment. All reliable fluid inclusion data were obtained from calcite-hosted inclusions. However, the fluid inclusion petrographic characteristics of garnet-hosted fluid inclusions are discussed briefly in this section. Salinity and density values for each inclusion were calculated using the fluid inclusion program *SoWat* and are listed in Table 3.4.

The majority of fluid inclusions analyzed comprised primary two phase liquid-vapor inclusions that are ubiquitous in all calcite crystals that were observed within the vein. These inclusions have consistent L-V ratios of ~80:20 and range in size from ~2 to 18 µm (Figure 3.6 b-g.). As whole assemblages, their characteristic habits include clusters, planar, or curved-planar. These primary L-V inclusions are divided into FIA # 1, FIA # 2A, B, C, FIA # 3, FIA # 4, FIA # 5, and FIA # 7 (Figure 3.6 a.), respectively.
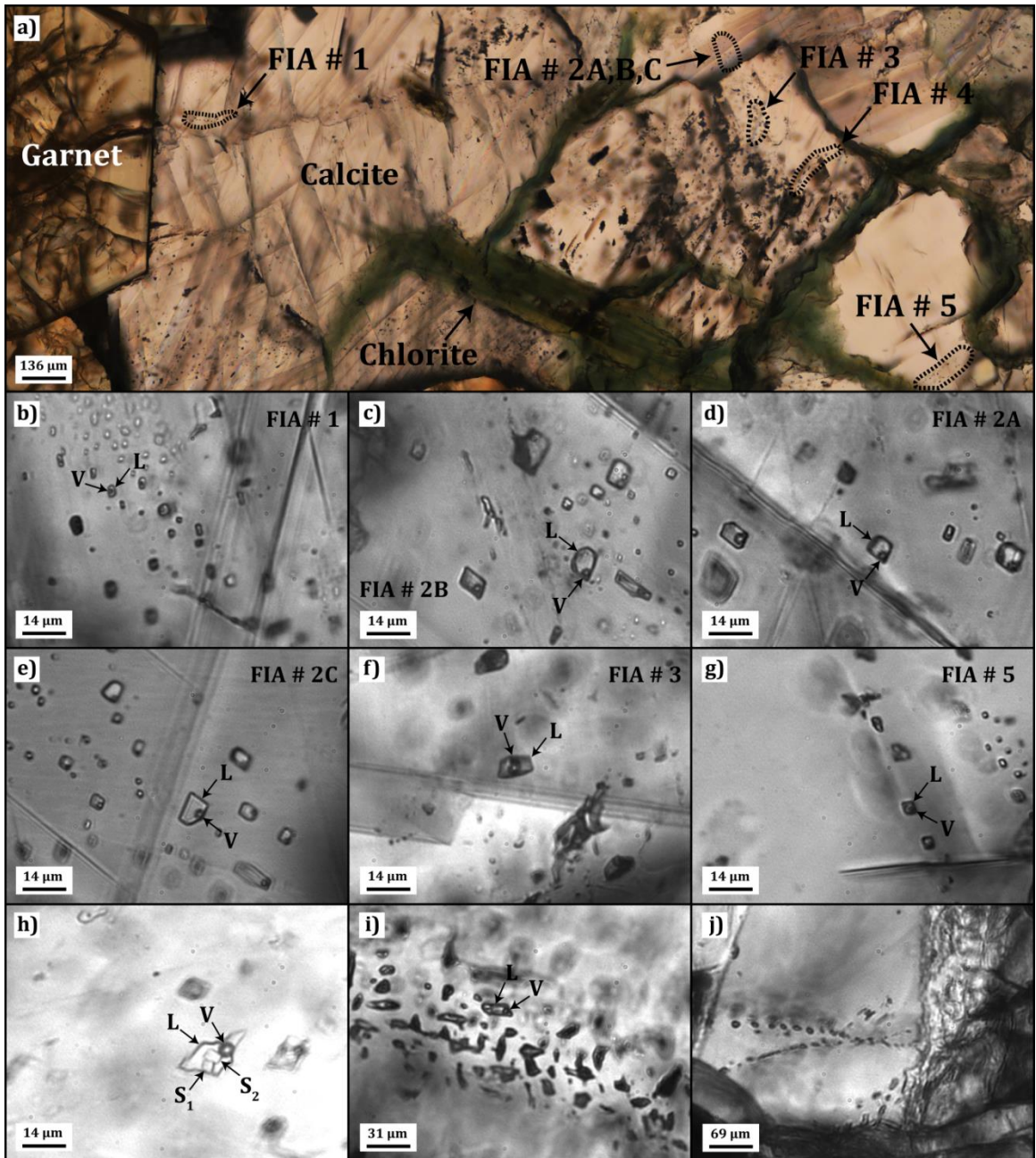
Figure 3.6 (previous page): General fluid inclusion characteristics of hydrothermal garnet-bearing "low sulfide" mineralization. a) Relative location of 5 fluid inclusion assemblages (FIA) referred to in this section. b) Trail of calcite-hosted primary L-V inclusions at FIA # 1. c) Cluster of calcite-hosted primary L-V inclusions at FIA # 2b. d) Trail of calcite-hosted primary L-V inclusions at FIA #2a. e) Trail of calcite-hosted primary L-V inclusions at FIA # 2c. f) Calcite-hosted primary L-V inclusion at FIA # 3. g) Cluster of calcite-hosted primary L-V inclusions at FIA # 5. h) Calcite-hosted L-V-S inclusion of undetermined origin. Measurements were not taken on this inclusion and the daughter minerals (S_1 and S_2) are not known. This inclusion was present outside of the field of view presented in (a). i) Trail of garnet core-hosted primary L-V inclusions. Measurements could not be made adequately. They were located outside of the field of view presented in (a). j) Two trails of garnet rim-hosted secondary inclusions. Measurements could not be made adequately. They were located outside of the field of view presented in (a).

FIA # 1 is a trail of curved-planar L-V inclusions located adjacent to a garnet crystal face. Homogenization temperatures (T_h) from V → L range from 126.2 to 132.9°C and last ice melting temperatures (T_m^{ice}) span -26.4 to -24.4°C. Calculated output salinities for this assemblage range from 25.18 to 26.44 wt% eq. NaCl and these salinity values represent the highest salinities measured for any assemblages referred to herein. Densities range from 1.124 – 1.137 g/cm^3.

FIA # 2 constitutes a relatively large cluster of L-V inclusions that are further subdivided into FIA # 2A, FIA # 2B, and FIA # 2C on the basis of their collective orientations. FIA # 2A consists of a collection of curved-planar inclusions that homogenize to 100% liquid at temperatures between 123.8 to 137.2°C and contain final ice melting temperatures ranging from -9.6 to -2.8°C. Salinities range from 4.65 to 13.51 wt% eq. NaCl and calculated densities range between 0.967 and 1.037 g/cm^3. FIA # 2B occurs as a cluster of inclusions with T_h from 126.8 to 161.2°C and T_m^{ice} from -6.4 to -1.2°C. Calculated salinities and densities for this assemblage range from 2.07 to 9.73 wt% eq. NaCl and from 0.950 to 1.006 g/cm^3, respectively. FIA # 2C comprises a cluster of inclusions with T_h from 116.7 to 167.5°C and T_m^{ice} from -18.0 to -6.2°C. Salinities range from 9.47 to 20.97 wt% eq. NaCl and densities range from 0.985 to 1.100 g/cm^3. FIA # 3, FIA # 4, and FIA # 5 occur as clusters and curved-planar to planar inclusion assemblages that are compositionally similar to one another and to those inclusions described in FIA # 2. In a few instances, T_h had to be estimated based on vapor bubble size and rate of shrinkage to avoid inclusion decrepitation during heating. Homogenization temperatures (V → L) for these 3

inclusion assemblages range from 98.9 to 210.0°C and T_m^{ice} values span between -5.8 and -4.1°C. Calculated output salinities for these assemblages range from 6.59 to 8.95 wt% eq. NaCl and salinities range from 0.909 to 1.009 g/cm^3.

FIA # 7 is a cluster of L-V inclusions that occurred outside of the field of view in Figure 3.6 a. Based on salinity considerations, these inclusions represent a different generation of inclusions than those discussed previously. Homogenization temperatures (T_h) from V → L range from 90.1 to 147.5°C and last ice melting temperatures (T_m^{ice}) span -21.2 to -19.4. Calculated output salinities for this assemblage range from 21.96 to 23.18 wt% eq. NaCl and densities range from 1.091 – 1.133 g/cm^3. Box and whisker diagrams (T_h, salinity) for the fluid inclusion assemblages discussed to this point are presented in Figure 3.7 a, b. Figure 3.7 c presents the field of isochores represented by all fluid inclusions analyzed in this study (including both populations: 23.65 wt% eq. NaCl and 8.26 wt% eq. NaCl). An isochore measured on calcite-hosted fluid inclusions (Molnár et al. 2001b) from a North Range footwall calcite-quartz-epidote-actinolite vein is plotted as a point of comparison and is in good agreement (parallel; slightly higher temperature) with the range of calcite-hosted fluid inclusion isochores measured in this study.

Two phase L-V inclusions were observed in the cores and rims of garnet but these inclusions were too small to obtain accurate and reliable data. The inclusions within the cores followed planar arrays and appeared primary (Figure 3.6 i) whereas the inclusions within the rims followed planar arrays perpendicular to garnet growth zones and were unambiguously secondary (Figure 3.6 j). A three

Table 3.4: Fluid inclusion measurements on 6 separate fluid inclusion assemblages in calcite.

Assemblage	T_h	$T_{m(ice)}$	S (wt% eq. NaCl)	ρ (g/cm^3)	Assemblage	T_h	$T_{m(ice)}$	S (wt% eq. NaCl)	ρ (g/cm^3)
FIA # 1	131.5	-24.36	25.18	1.124	FIA # 4	133.6	-5.1	8.00	0.989
	126.2	-26.1	26.25	1.137		130.9	-5.6	8.68	0.996
	132.9	-26.4	26.44	1.134		132.1	-5.3	8.28	0.992
FIA # 2A	137.2	-4.4	7.02	0.979		129.7	-4.5	7.17	0.986
	126.2	-4.7	7.45	0.990		122.6	-4.4	7.02	0.990
	123.8	-9.6	13.51	1.037		125.7	-4.6	7.31	0.990
	131.0	-2.8	4.65	0.967		114.8	-4.6	7.31	0.998
FIA # 2B	126.8	-6.4	9.73	1.006	FIA # 5	210*	-5.8	8.95	0.925
	128.6	-1.2	2.07	0.950		210*	-5.7	8.81	0.924
	129.5	-1.8	3.06	0.957		122.3	-5.8	8.95	1.004
	138.1	-5.4	8.41	0.988		210*	-4.3	6.88	0.909
	161.2	-4.2	6.74	0.956		210*	-4.5	7.17	0.911
FIA # 2C	135.6	-6.2	9.47	0.998		210*	-4.6	7.31	0.912
	167.5	-7.7	11.34	0.985		129.5	-5.6	8.68	0.997
	123.6	-11.8	15.76	1.054		210*	-5.4	8.41	0.921
	138.8	-7.3	10.86	1.005		124.5	-4.3	6.88	0.988
	116.7	-18	20.97	1.100		190.2	-4.5	7.17	0.932
FIA # 3	134.1	-4.9	7.73	0.986		195.1	-4.1	6.59	0.922
	134.9	-4.9	7.73	0.986	FIA # 7	121.8	-19.8	22.24	1.106
	99.8	-4.7	7.45	1.009		107.9	-19.7	22.17	1.115
	134.9	-4.6	7.31	0.982		90.1	-20.7	22.85	1.132
	98.9	-4.5	7.17	1.008		147.5*	-20.3	22.58	1.091
	103.5	-4.9	7.73	1.009		93.3	-21.2	23.18	1.133
	153.3	-4.7	7.45	0.968		98.1	-19.4	21.96	1.120
	165.5	-4.6	7.31	0.956					

Salinity and density values were calculated using the program *SoWat*. * = avoided inclusion decrepitation during heating by taking these temperatures as estimates based on vapor bubble size and rate of shrinkage
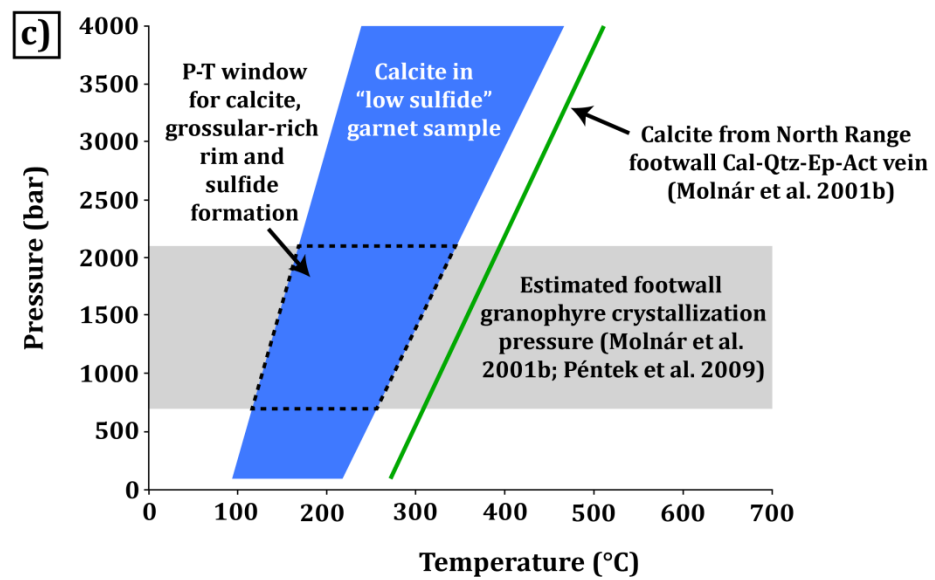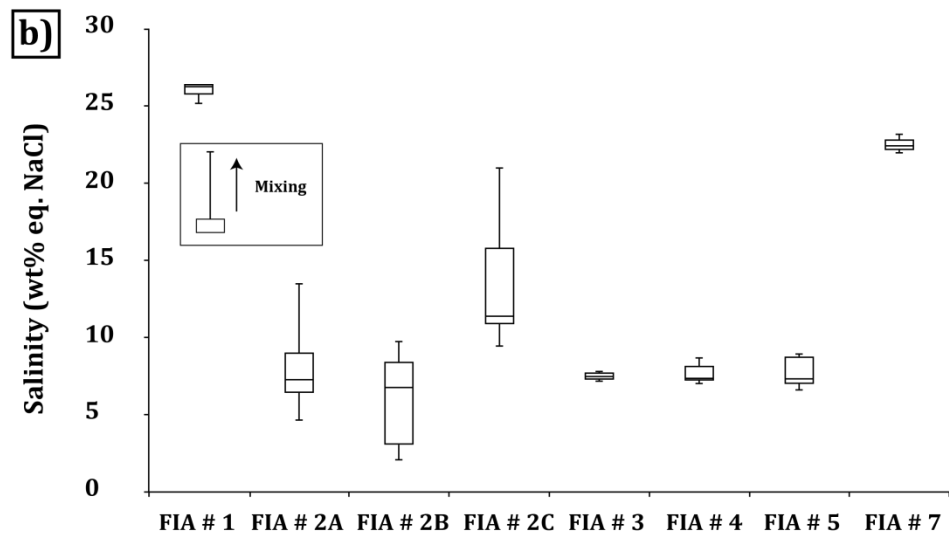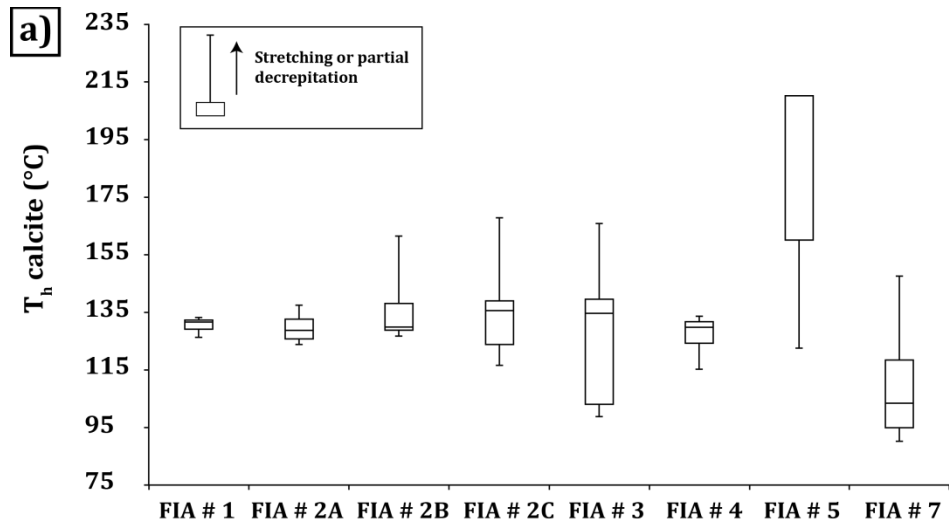
Figure 3.7 (previous page): Fluid inclusion characteristics of calcite associated with "low sulfide" mineralization. a) Range in homogenization (vapor bubble disappearance) temperatures for each fluid inclusion assemblage. b) Range in calculated salinities for each fluid inclusion assemblage. c) Projected isochore field outlining all isochores calculated for each population of primary calcite-hosted fluid inclusion assemblages described in this study (FIA#1, FIA#2A, FIA#2B, FIA#2C, FIA#3, FIA#4, FIA#5, FIA#7). An additional isochore (green) calculated from primary calcite-hosted inclusions within a North Range footwall Cal-Qtz-Ep-Act vein (Molnár et al. 2001b) is plotted and is nearly parallel to the higher temperature segment of the isochore field outlined in this study. The grey field outlines the range of estimated footwall granophyre crystallization temperatures as deduced by Al-in-hornblende barometry (Molnár et al. 2001b; Péntek et al. 2009).

phase L-V-S inclusion was also observed hosted in calcite outside of the field of view depicted in Figure 3.6 a. Two cube-shaped solids (S_1 and S_2), likely NaCl or $CaCl_2$, were present in this inclusion (Figure 3.6 h). It has a cusp-shape on one end and it appears that it may have pinched-off or necked-down at some point post-entrapment; therefore, no measurements were made on this L-V-S inclusion. This post-entrapment modification may explain the presence of solid phases.

3.3.4 Oxygen isotope composition of calcite and garnet

Secondary ion mass spectrometry (SIMS) analyses were performed on calcite and in the two compositionally-different growth zones within garnets (andradite cores, grossular-rich rims). Calcite analyses were calibrated using Jop-Cal and garnet analyses were calibrated using UWG-2. Since the composition of UWG-2 ($Alm_{45}Prp_{40}Grs_{14}Sps_1$) differs from both the cores and rims analyzed in this study, the introduction of additional instrumental bias due to "matrix effects" must be considered and absolute values relayed in this study should be taken within their additional error due to compositional discrepancies between standards and unknowns. Page et al. (2010) analyzed garnets of strikingly similar composition to the andradite cores and grossular-rich rims analyzed in this study (92LEW7: $Adr_{89}Grs_6Alm_4Prp_1$; 92LEW10: $Adr_{50}Grs_{42}Alm_4CaTi_2Prp_2$) by calibrating them to the UWG-2 standard, and reported additional errors from matrix effects that resulted in $\delta^{18}O$ values which were 6.69‰ and 5.64‰ heavier than the accepted values for their unknowns using compositionally-similar standards. Therefore, $\delta^{18}O$ values for garnet could be higher than those reported below. However, if differences between

$\delta^{18}O$ values for core and rim analyses are bigger than the respective errors on the cores and rims, then inferences can be made about the geological processes that produced the $\delta^{18}O$ shifts.

A total of 19 (9 core/10 rim) individual spot analyses were carried out along a traverse in the largest (>5 mm diameter) garnet that was analyzed in this study (Figure 3.8 a). Output $\delta^{18}O$ values were fairly uniform within the cores and more variable within the rims. The 9 core analyses have average $\delta^{18}O$ values of 10.9 ± 1.2‰ that range from 9.7 to 12.6‰ and the 10 rim analyses have average $\delta^{18}O$ values of 5.1 ± 1.2‰ that range from -0.5 to 9.2‰. When considering the additional +5.64‰ instrumental bias that could exist for rim analyses, the average $\delta^{18}O$ rim value would be ~10.7‰ (still lighter than the average core values without taking into account additional compositional errors on the cores). Owing to the fact that the additional instrumental bias on the cores (6.69‰) is higher than the rims due to the larger andradite component in the cores, it appears that the rim is recording a shift towards lighter $\delta^{18}O$ values.

Spot analyses on both cores and rims were undertaken on 3 additional garnets (Figure 3.8 b). The 8 core analyses among these 3 garnets have $\delta^{18}O$ values of 8.9 ± 1.2‰ that range from 6.0 to 11.7‰ whereas the 8 rim analyses have average $\delta^{18}O$ values of 4.2 ± 1.2‰ that range from -0.6 to 9.6‰. It is possible that the heavy (9.6‰) value measured on the rim was actually a core analysis as deciphering core from rim on some segments of the smaller garnets could be difficult. Taking into account the magnitude of the shifts toward heavier oxygen

isotope compositions expected for both the cores and the rims on these 3 garnets, it appears that they also record a shift towards lighter $\delta^{18}O$ values within their rims.

Ten analyses of calcite were taken and they displayed some variation but no significant outliers were present (Figure 3.8 c). The 10 calcite analyses have average $\delta^{18}O$ values of 5.1 ± 1.2‰ that range from 2.9 to 7.4‰. These values are closely matched to the average $\delta^{18}O$ values for the 18 grossular-rich rim analyses (4.7‰). Calculated fluid compositions using O'Neil et al. (1969) from these analyses (Table 3.5) of -4.22‰ (200°C) and 1.79‰ (250°C) are taken to represent the true $\delta^{18}O$ signature of the mineralizing fluid because matrix effects are not an issue in calcite (less major element compositional variability) to the extent that they are in garnet.

3.4 Discussion

3.4.1 Mineralogical and chemical constraints on the redox evolution of "low sulfide" high-PGE mineralization

As discussed in Chapter 2, "low sulfide" mineralization is constrained to the SIC footwall (commonly but not exclusively spatially associated with sharp-walled veins) and is characterized by blebs, disseminations, and stringers of sulfide minerals (bornite, chalcopyrite, millerite) that are intergrown with hydrothermal silicates and carbonates and have high PGE grades (Pt, Pd). Low sulfide samples have been divided mineralogically into 3 subgroups that relate to their respective abundances of Ca-silicates/carbonates: calcite-free (lacks calcite, garnet), calcite-
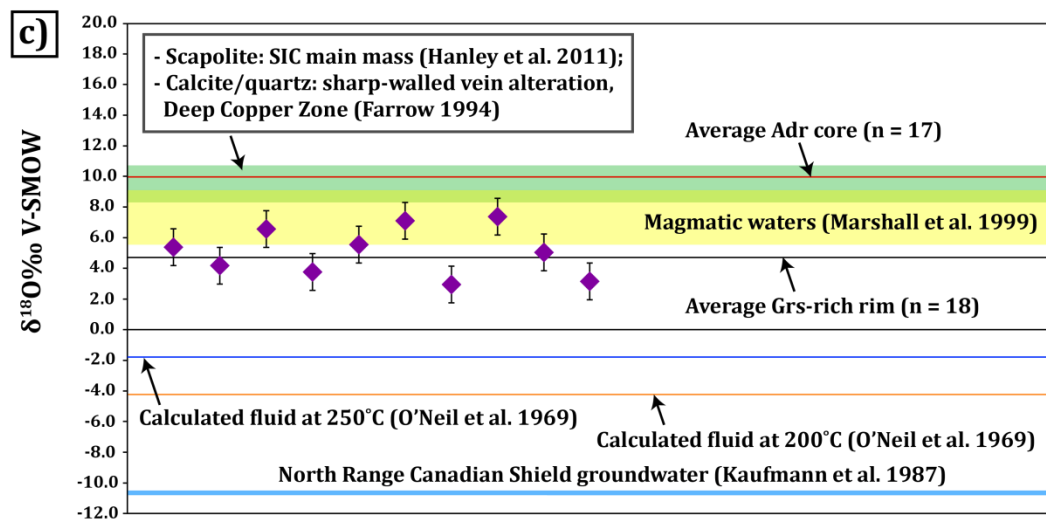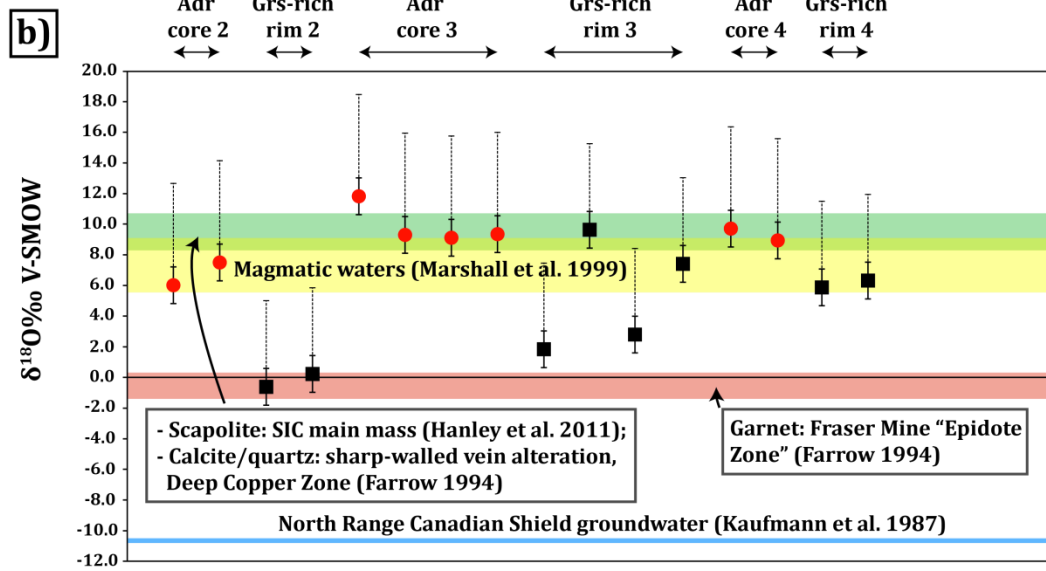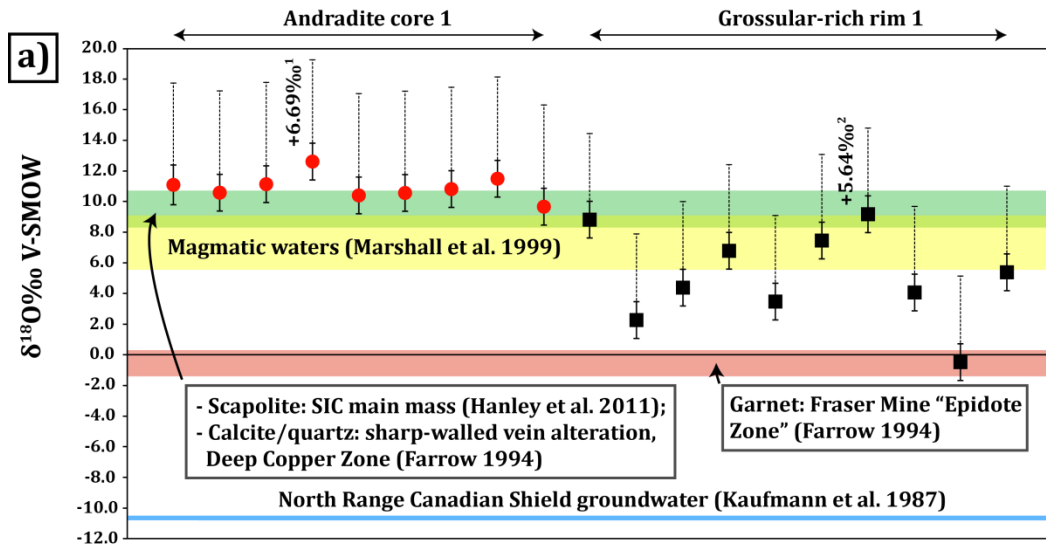
a) Andradite core 1 — Grossular-rich rim 1

+6.69‰[1]

+5.64‰[2]

Magmatic waters (Marshall et al. 1999)

- Scapolite: SIC main mass (Hanley et al. 2011);
- Calcite/quartz: sharp-walled vein alteration, Deep Copper Zone (Farrow 1994)

Garnet: Fraser Mine "Epidote Zone" (Farrow 1994)

North Range Canadian Shield groundwater (Kaufmann et al. 1987)

δ¹⁸O‰ V-SMOW

b) Adr core 2 — Grs-rich rim 2 — Adr core 3 — Grs-rich rim 3 — Adr core 4 — Grs-rich rim 4

Magmatic waters (Marshall et al. 1999)

- Scapolite: SIC main mass (Hanley et al. 2011);
- Calcite/quartz: sharp-walled vein alteration, Deep Copper Zone (Farrow 1994)

Garnet: Fraser Mine "Epidote Zone" (Farrow 1994)

North Range Canadian Shield groundwater (Kaufmann et al. 1987)

δ¹⁸O‰ V-SMOW

c)
- Scapolite: SIC main mass (Hanley et al. 2011);
- Calcite/quartz: sharp-walled vein alteration, Deep Copper Zone (Farrow 1994)

Average Adr core (n = 17)

Magmatic waters (Marshall et al. 1999)

Average Grs-rich rim (n = 18)

Calculated fluid at 250°C (O'Neil et al. 1969)

Calculated fluid at 200°C (O'Neil et al. 1969)

North Range Canadian Shield groundwater (Kaufmann et al. 1987)

δ¹⁸O‰ V-SMOW

141

Figure 3.8 (previous page): $\delta^{18}O$ in garnet/calcite from hydrothermal garnet-bearing "low sulfide" mineralization. See digital appendix for supplementary data. a) $\delta^{18}O$ V-SMOW‰ results for core/rim spot analyses across an individual garnet. Standard deviation reported at 1 σ. Analyses were calibrated using UWG-2. Additional positive error bars (superscripts 1, 2) take into account inherent instrumental bias in garnet relative to UWG-2 which varies as a function of garnet composition. The average core composition from 15 separate garnets analyzed in this study is $Adr_{83.35}Alm_{13.81}Grs_{2.48}Prp_{0.35}Sps_{0.01}$, which most closely matches garnet standard 92LEW7 ($Adr_{89}Grs_{6}Alm_{4}Prp_{1}$). Page et al. 2010 reported an average instrumental bias of +6.69‰ for 92LEW7 when calibrating analyses to UWG-2. The average rim composition from 15 separate garnets analyzed in this study is $Adr_{53.54}Grs_{32.60}Alm_{13.78}Sps_{0.09}$, which most closely matches garnet standard 92LEW10 ($Adr_{50}Grs_{42}Alm_{4}CaTi_{2}Prp_{2}$). Page et al. 2010 reported an average instrumental bias of +5.64‰ for 92LEW10 when calibrating analyses to UWG-2. Fields for magmatic waters (Marshall et al. 1999), North Range Canadian Shield groundwater (Kaufmann et al. 1987), SIC scapolite/sharp-walled vein-associated calcite and quartz (Farrow, 1994; Hanley et al. 2011), and garnet from alteration assemblages (see text) at the Fraser Mine "Epidote Zone" (Farrow 1994) are also depicted. b) $\delta^{18}O$ V-SMOW‰ results for core/rim spot analyses across 3 more garnets. Standard deviation reported at 1 σ. c) $\delta^{18}O$ V-SMOW‰ results for 10 spot analyses of calcite. Standard deviation reported at 1 σ. Analyses were calibrated using Jop-Cal. Lines for average cores and rims from the garnet analyses are superimposed on this figure. The calcite has an oxygen isotope signature similar to the garnets rims. Average $\delta^{18}O$ V-SMOW for the calcite-forming fluid were calculated at 200°C and 250°C using O'Neil et al. (1969) and are superimposed on the figure.

Table 3.5: Calculated fluid isotopic compositions using calcite and equation from O'Neil et al. (1969).

Sample	$\delta^{18}O_{\text{V-SMOW}}$ calcite	T (°C)	$\delta^{18}O_{\text{V-SMOW}}$ fluid (O'Neil et al. 1969)
Cal-Smp-1	5.31	200	-3.72
		250	-1.47
Cal-Smp-2	4.15	200	-4.87
		250	-2.62
Cal-Smp-3	6.48	200	-2.56
		250	-0.30
Cal-Smp-4	3.77	200	-5.25
		250	-3.00
Cal-Smp-5	5.49	200	-3.55
		250	-1.30
Cal-Smp-6	7.10	200	-1.95
		250	0.31
Cal-Smp-7	2.88	200	-6.13
		250	-3.88
Cal-Smp-8	7.35	200	-1.70
		250	0.56
Cal-Smp-9	5.02	200	-4.01
		250	-1.76
Cal-Smp-10	3.11	200	-5.91
		250	-3.66
Average	4.84	200	-4.22
		250	-1.79

bearing (lacks garnet), and garnet-bearing to aid in comparisons and help identify mechanisms for the evolution of low sulfide systems at the deposit scale.

Garnet in low sulfide-associated "garnet-bearing" alteration is zoned from andradite cores ($Adr_{83.35}Alm_{13.81}Grs_{2.48}Prp_{0.35}Sps_{0.01}$; n = 169) to grossular-rich ($Adr_{53.54}Grs_{32.60}$ $Alm_{13.78}Sps_{0.09}$; n = 25) rims. Bornite, chalcopyrite, and millerite occur as primary blebs and disseminations within calcite-quartz matrix and grossular-rich rims on garnet crystals. Sulfides also persist as primary inclusions within grossular-rich "patches" that are present within the andradite cores. Any other sulfides in the andradite cores that are not associated with grossular-rich patches are clearly secondary (infilling cracks, cavities, etc.). The presence of massive calcite (containing primary sulfide minerals) enclosing entire garnet crystals combined with the observation of a grossular-rich rim-hosted assemblage of calcite in equilibrium with chalcopyrite in an individual garnet crystal (Figure 3.2 f) suggest a temporal relationship between calcite, sulfide, and grossular-rich rim formation. The transition from andradite cores to grossular-rich rims coeval with the precipitation of sulfide minerals has implications on the redox state of the fluid system. Garnet incorporates trivalent cations into its crystal structure whereas BMS incorporate divalent cations. An increase in the grossular content of garnet along the rim indicates that Al^{3+} began occupying the site originally filled by Fe^{3+} in the andradite cores. Combine this with the sudden occurrence of sulfides, it appears that the Fe^{3+}/Fe^{2+} ratio was decreased and Fe^{2+} partitioned into the sulfides. This change in the oxidation state of iron (contemporaneous with rim formation and

sulfide precipitation) towards more ferrous availability implies reduction. In work on the thermal stability of epidote as a function of fO_2 and Fe content, Holdaway (1972) demonstrated that (for garnet-epidote equilibria Figure 3.2 c, e) as the oxygen fugacity is lowered, the epidote becomes more Al-rich and the garnet becomes richer in the grossular component.

The concentration gradient of certain trace elements (elements that take on >1 oxidation state in geological environments) across garnets also tracks the redox evolution of this fluid. The enrichment of Sn (2^+, 4^+) and Ce (3^+, 4^+) and depletion of Mn (2^+, 3^+) and Eu (2^+, 3^+) in the cores all imply progressively reducing fluid behavior transitioning from the cores to the rims. Reduction is also evidenced from the decrease of the Eu-anomaly at the onset of grossular-rich rim growth. All available evidence (including the stabilization of sulfbismuthites, Ch. 2) suggests that low sulfide high-PGE mineralization occurred in response to the influx of a reducing fluid in the footwall.

3.4.2 Tracking the evolution of "low sulfide" high-PGE mineralization through the SIC footwall

The two populations of fluid inclusions presented in this low sulfide sample (23.65 wt% eq. NaCl; 8.26 wt% eq. NaCl) both contain lower salinities than fluid inclusions that Molnár and Watkinson (2001a) reported in primary quartz-hosted inclusions associated with sharp-walled veins at the McCreedy East deposit (34.9 – 48.1 wt% eq. NaCl). Since there are clearly different (salinity) populations of primary calcite-hosted fluid inclusions in this study, the salinity of the fluid that

precipitated calcite must have increased or decreased during the course of its traverse through the footwall. It is therefore inferred that some mechanism caused notable salinity changes in the mineralizing fluid. Interaction with salt-charged ground water would be one possible mechanism to achieve this salinity variation.

True $\delta^{18}O$ values of -4.22‰ (200°C) and -1.79‰ (250°C) for the mineralizing fluid at the time of sulfide precipitation are calculated from the average of the 10 fairly tightly clustered calcite analyses: 5.1 ± 1.2‰. However, it is the shift towards lighter $\delta^{18}O$ from garnet cores to rims that lends more significant information regarding the genesis of low sulfide-type mineralization. The heavier rims are situated in the field of "magmatic waters" as outlined in Marshall et al. (1999). With the SIC seemingly representing the most likely source of metals in the immediate vicinity of low sulfide mineralization, it is probable that the low sulfide fluid was derived from a magmatic reservoir. It is worth noting that Farrow (1994) reported 4 garnets associated with alteration at the oxidized Ni-rich Epidote Zone of average composition $Adr_{64}Grs_{36}$ and further geochemical work could address whether these garnets formed from the same "low sulfide" fluid. Exsolved fluid from the SIC or from North Range footwall granophyre appear to be the most obvious candidates for the original low sulfide mineralization fluid source. It seems unlikely that the fluid source for low sulfide mineralization was Cl-rich fluid exsolved from the sharp-walled veins for four reasons: (1) cross-cutting relationships in the footwall (Farrow et al. 2005), (2) low sulfide mineralization is not a characteristic byproduct of sharp-walled veins whereas Cl-rich alteration haloes appear to be

(Hanley and Mungall, 2003), (3) Farrow (1994) reported $\delta^{18}O$ values in quartz/calcite from sharp-walled vein alteration at the Strathcona Mine (Deep Copper Zone) ranging from 8.6 to 10.7 ‰; whereas calcite $\delta^{18}O$ values in low sulfide mineralization from this study are much lighter (5.1 ‰), (4) This study suggests the redox state of the mineralizing system would have to flip (from oxidizing to reducing). Once this fluid exsolved from a magmatic body and permeated openings in the SIC footwall, it must have interacted with an entirely different geochemical reservoir to cause changes to its oxygen isotope signature and this new reservoir must have been characterized by lighter $\delta^{18}O$ values in order to account for the shifts that were observed in garnet in this study. Most commonly reported geochemical reservoirs are similar to or heavier than the range of $\delta^{18}O$ values described in this study (e.g., chondritic meteorites, MORB, andesites/rhyolites, detrital sediments, argillic sediments, limestone, etc.) and many of them do not fit into the context of the lithologies present in the Sudbury region. Meteoric water spans a large range of negative $\delta^{18}O$ values and can exhibit $\delta^{18}O$ values light enough to achieve the oxygen isotope shift measured in this study. North Range groundwater is loaded in $CaCl_2$, has a well-defined oxygen isotope composition that ranges from -10.8 to -10.5‰ (Kaufmann et al. 1987), and represents the most plausible explanation for the observed $\delta^{18}O$ shifts. Progressive dilution of the original magmatically-derived fluid (garnet cores: 10.0‰) could lower $\delta^{18}O$ to values of 4.7‰ and 5.1‰ measured in the garnet rims and calcite, respectively.

Hanley et al. (2005) reported quartz-hosted methane-dominant hydrocarbon fluid inclusions in Au-Pt-rich quartz-sulfide-epidote alteration veins spatially

associated with footwall mineralization at the Fraser Mine. More recently, Kerr (2013) demonstrated (from various mineralized footwall samples along the North Range) the existence of elevated hydrocarbon abundances in high-PGE quartz-sulfide-epidote alteration (akin to low sulfide mineralization) using gas chromatography. These studies suggest that the mobilization of ore metals in low sulfide-type mineralization was associated with hydrocarbon-rich aqueous fluids. A series of interdependent reactions can document progressive reduction accompanying the precipitation of bornite (by lowering fO_2) and the mixing of groundwater ($CaCl_2$) and hydrocarbon-rich (CH_4) fluids to precipitate calcite. The following reactions describe this process and illustrate a simplified mechanism that could account for some of the characteristics of low sulfide mineralization in the footwall (Landtwing et al. 2005):

$$30CuCl_2^- + 6FeCl_2 + 21H_2S(aq) + 3SO_2(aq) = 6Cu_5FeS_4(s) + 30Cl^- + 42HCl + 3O_2 \quad (1)$$
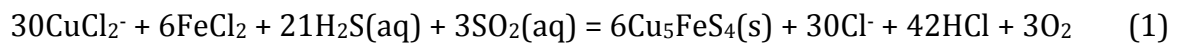
This bornite-producing reaction (1) is highly sensitive to the concentration of H_2S which forms by the disproportionation of SO_2 upon cooling (Landtwing et al. 2005):

$$4SO_2 + 4H_2O = H_2S + 3H_2SO_4 \quad (2)$$

Mixing groundwater with a hydrocarbon-rich fluid can consume oxygen (lowering fO_2), driving reaction (1) to the right and forming more bornite (similar reactions will produce the remaining sulfides: chalcopyrite and millerite) and precipitating calcite:

$$CaCl_2(aq) + CH_4 + 2O_2 = CaCO_3(s) + 2HCl\ (aq) + H_2O \quad (3)$$
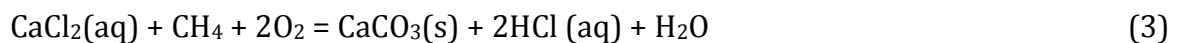
The crystallization of carbonate, sulfides, and other Ca-rich silicates in response to progressive cooling and groundwater dilution would enclose previously-precipitated precious metal minerals that give the low sulfide ore its "high-PGE" status. Addition of $CaCl_2$ groundwater to the system would also increase the bulk salinity of the mineralizing fluid and suggests that the temporal salinity change referred to at the beginning of this section would be in a positive direction (salinity increase with the evolution of the fluid). The variation in alteration mineralogy of low sulfide mineralization may reflect differing degrees of groundwater interaction within the SIC footwall. "Garnet-bearing" alteration represents an end member of the three types of low sulfide alteration resulting from fluids that have seen the most interaction with groundwater and have achieved calcium activities high enough to precipitate hydrothermal Ca-phases including garnet and >80% calcite. It is not surprising that this type of alteration was located at the deepest (and furthest away from the SIC contact) position in the SIC footwall of any sample that was collected in this study. The fluid responsible for the formation of this highly evolved assemblage likely unloaded PGE (Pt, Pd) earlier in its evolution as their complexing assemblages became less soluble upon cooling, resulting in lower bulk rock Pt & Pd grades compared to "calcite-free" and "calcite-bearing" low sulfide alteration assemblages (Chapter 2). The anomalously high Au grades in "garnet-bearing" alteration suggests Au deposition was decoupled with precipitation of the platinum group minerals. "Calcite-free" low sulfide alteration represents the other end of the low sulfide system; it has seen the least interaction

with groundwater. "Calcite-bearing" low sulfide alteration spans a continuum between the aforementioned end members.

3.5 Conclusions

"Low sulfide" mineralization at Level 5080 of the Coleman 153 ore body is characterized by a very calcium-rich alteration assemblage that contains calcite, garnet, epidote, and calcic amphiboles. The garnets have two compositionally-different growth zones: andradite cores and grossular-rich rims. Primary bornite, chalcopyrite, and millerite are located in massive calcite as well as in grossular-rich rims on garnet. The observed sulfide-gangue textures indicate that sulfides precipitated contemporaneous to the formation of both calcite and the grossular-rich rims on garnet. Discrete, heavy metal-bearing phases in this sample consist of Bi-bearing millerite ($\leq$8 atomic % Bi), cassiterite, electrum, hessite, native zinc, tenorite, and an unknown Ni-Mo-Bi mineral. The oxides (cassiterite, tenorite) are all hosted in rutile. The remaining phases (electrum, hessite, native zinc, unknown Ni-Mo-Bi mineral) are hosted in epidote, calcite, and/or the sulfide minerals. Platinum group minerals are noticeably absent in this vein and this is reflected by lower bulk rock Pt+Pd grades compared to other occurrences of low sulfide mineralization. However, Au grades are very high.

Trace element variation across zoned garnets confirms the existence of two compositionally-different growth zones. Elements that take on more than one oxidation state (Sn, Ce, Mn, Eu) and mapped Eu-anomalies indicate that the rims along garnets (and correspondingly calcite and the sulfides) formed in association

with the influx of a reducing fluid in the footwall. Fluid inclusions in calcite are two phase L-V and comprise two different populations on the basis of their respective salinities: (1) 23.65 wt% eq. NaCl and (2) 8.26 wt% eq. NaCl. Homogenization temperatures derived from both populations have an average of 140.2°C and range from 90.1 - 210.0°C.

Secondary ion mass spectrometry analyses (SIMS) of calcite record an average $\delta^{18}O$ value of 5.1 ± 1.2‰; with corresponding calculated values of -4.22‰ (200°C) and -1.79‰ (250°C) for the mineralizing fluid at the time of sulfide precipitation. Heavy (10.0‰) $\delta^{18}O$ values for garnet cores indicate that the initial fluid was derived from an isotopically heavy oxygen isotope reservoir. With current knowledge of the geology at Sudbury, the most likely source of that fluid is the SIC itself or some variation of footwall granophyre. It is unlikely that the fluid source for low sulfide mineralization is Cl-rich fluid exsolved from the sharp-walled veins. Relative $\delta^{18}O$ shifts towards lighter values from the cores to the rims in garnets indicate progressive interaction with and dilution by ($CaCl_2$-rich) North Range groundwater.

Low sulfide (high-PGE) footwall mineralization is sourced from a hydrocarbon-enriched aqueous fluid that was loaded in ore metals derived from an unidentified source. This hydrothermal fluid entered the footwall using some of the same structural pathways as the sharp-walled veins. Precious metal minerals (exhibiting limited solid solution Ch. 2) crystallized early in the paragenetic history of low sulfide mineralization and many of them would remain in solution until the

stabilization of sulfides and associated gangue phases. Continual reduction of the fluid over its evolution (as evidenced through sulfide/gangue relationships, trace element zoning in garnet, garnet-epidote equilibria considerations, stabilization of sulfbismuthites Ch. 2) by groundwater dilution resulted in the precipitation of sulfides and the formation of increasing amounts of Ca-mineral phases in equilibrium with the sulfides. The calcium-rich alteration assemblage (calcite, garnet, epidote, calcic amphiboles) in the low sulfide package described in this chapter represents an apparent end member to the low sulfide continuum. It has seen the most interaction with $CaCl_2$ groundwater, lost most of its PGE load, and kept Au in solution to ultimately produce Au grades that are much higher than those typical of other low sulfide occurrences.

Cross-cutting relationships around Sudbury suggest that the fluid responsible for low sulfide mineralization entered the footwall prior to mobilization of the Cu-rich residue responsible for crystallization of the sharp-walled vein stockwork systems. The spatial association between high sulfide sharp-walled veins and low sulfide high-PGE mineralization is not exclusive, and it has no bearing on the genesis of either respective mineralization style except for the fact that the fluids responsible for each mineralization style took advantage of the same meteorite impact-induced openings in the footwall. "Hybrid" mineralization highlights the fact that each mineralization style used the same shoots upon entrance into the footwall and not that the two styles are in any way genetically-related.

3.6 References

Ames DE, Golightly JP, Lightfoot PC, Gibson HL (2002) Vitric compositions in the Onaping Formation and their relationship to the Sudbury Igneous Complex, Sudbury structure. Economic Geology 97:1541-1562

Berry AJ, Burnham AD, Halse HR, Cibin G, Mosselmans JFW (2013) The oxidation states of cerium and europium in silicate melts as a function of oxygen fugacity, composition and temperature (abs). Goldschmidt 2013 Conference, August 25-30, 2013, Florence, Italy

Bocchio R, Adamo I, Diella V (2010) The profile of trace elements, including the REE, in gem-quality green andradite from classic localities. The Canadian Mineralogist 48:1205-1216

Dare SAS, Barnes SJ, Beaudoin G (2012) Variation in trace element content of magnetite crystallized from a fractionating sulfide liquid, Sudbury, Canada: Implications for provenance discrimination. Geochimica et Cosmochimica Acta 88:27-50

Donohue CL, Essene EJ (2000) An oxygen barometer with the assemblage garnet-epidote. Earth and Planetary Science Letters 181:459-472

Einaudi MT, Meinert LD, Newberry RJ (1981) Skarn deposits. Economic Geology 75:317-391

Farrow CEG (1994) Geology, alteration, and the role of fluids in Cu-Ni-PGE mineralization of the footwall rocks to the Sudbury Igneous Complex, Levack and Morgan Townships, Sudbury District, Ontario. Unpublished Ph.D. thesis, Carleton University, Ottawa, Canada, 373 p.

Farrow CEG, Everest JO, King DM, Jolette C (2005) Sudbury Cu(-Ni)-PGE systems: Refining the classification using McCreedy West Mine and Podolsky project case studies. In: Mungall JE (ed) Exploration for deposits of platinum-group elements. MAC Short Course Series 35:163-180

Gaspar M, Knaack C, Meinert LD, Moretti R (2008) REE in skarn systems: A LA-ICPMS study of garnets from the Crown Jewel gold depost. Geochimica et Cosmochimica Acta 72:185-205

Gibson AM, Lightfoot PC, Evans TC (2010) Contrasting styles of low sulphide high precious metal mineralisation in the 148 and 109 FW zones: North and South Ranges of the Sudbury Igneous Complex, Ontario, Canada. In: Jugo PJ, Lesher CM, Mungall JE (eds) Abstracts, 11th International Platinum Symposium, 2010, Sudbury, Ontario, Canada. OGS Misc. Release Data 269

Goldstein RH (2003) Petrographic analysis of fluid inclusions. In: Samson I, Marshall D, Anderson A (ed) Fluid Inclusions: Analysis and Interpretation. Mineralogical Association of Canada, Short Course Series 32:9-54

Hanley JJ, Mungall JE (2003) Chlorine enrichment and hydrous alteration of the Sudbury Breccia hosting footwall Cu-Ni-PGE mineralization at the Fraser Mine, Sudbury, Ontario, Canada. The Canadian Mineralogist 41:857-881

Hanley JJ, Mungall JE, Pettke T, Spooner ETC, Bray CJ (2005) Ore metal redistribution by hydrocarbon-brine and hydrocarbon-halide melt phases, North Range footwall of the Sudbury Igneous Complex, Ontario, Canada. Mineralium Deposita 40:237-256

Hanley JJ, Ames D, Barnes J, Sharp Z, Guillong M (2011) Interaction of magmatic fluids and silicate melt residues with saline groundwater in the footwall of the Sudbury Igneous Complex, Ontario, Canada: New evidence from bulk rock geochemistry, fluid inclusions and stable isotopes. Chemical Geology 281:1-25

Harangai SZ, Downes H, Kósa L, Szabó CS, Thirlwall MF, Mason PRD, Mattey D (2001) Almandine garnet in calc-alkaline volcanic rocks of the Northern Pannonian Basin (Eastern-Central Europe): Geochemistry, petrogenesis and geodynamic implications. Journal of Petrology 42:1813-1843

Holdaway MJ (1972) Thermal stability of Al-Fe epidote as a function of fO_2 and Fe content. Contributions to Mineralogy and Petrology 37:307-340

Holliger P, Cathelineau M (1988) In situ U-Pb age determination by secondary ion mass spectrometry. Chemical Geology 70 (no 1-2):173

Ionov D (2004) Chemical variations in peridotite xenoliths from Vitim, Siberia: Inferences for REE and Hf behavior in the garnet-facies upper mantle. Journal of Petrology 45:343-367

Jamtveit B, Ragnarsdottir KV, Wood BJ (1995) On the origin of zoned grossular-andradite garnets in hydrothermal systems. European Journal of Mineralogy 7:1399-1410

Kaufmann R, Frape S, Fritz P, Bentley H (1987) Chlorine stable isotope composition of Canadian Shield brines. In: Fritz P, Frape SK (eds) Saline water and gases in crystalline rocks. Geological Association of Canada Special Paper 33:89-93

Kerr MJ (2013) The application of gas chromatography in characterizing bulk fluid inclusion hydrocarbons in the footwall of the Sudbury Igneous Complex and

other magmatic, hydrothermal and surficial ore-forming environments. Unpublished M.Sc. thesis, Saint Mary's University, Halifax, Canada, 241 p.

Landtwing MR, Pettke T, Halter WE, Heinrich CA, Redmond PB, Einaudi MT, Kunze K (2005) Copper deposition during quartz dissolution by cooling magmatic-hydrothermal fluids: The Bingham porphyry. Earth and Planetary Science Letters 235:229-243

Lehrmann B (2012) Polymetallic mineralisation in the Chillagoe district of north-east Queensland: Insights into base metal rich intrusion-related gold systems. Unpublished Ph.D. thesis, James Cook University, Queensland, Australia, 337 p.

Li C, Naldrett AJ, Coats CJA, Johannessen P (1992) Platinum, palladium, gold and copper-rich stringers at the Strathcona Mine, Sudbury: Their enrichment by fractionation of a sulfide liquid. Economic Geology 87:1584-1598

Marshall D, Watkinson D, Farrow C, Molnár F, Fouillac AM (1999) Multiple fluid generations in the Sudbury igneous complex: fluid inclusion, Ar, O, H, Rb and Sr evidence. Chemical Geology 154:1-19

Micko J (2010) The geology and genesis of the Central Zone Alkalic Copper-Gold Porphyry Deposit, Galore Creek District, northwestern British Columbia, Canada. Unpublished Ph.D. thesis, The University of British Columbia, Vancouver, Canada, 387 p.

Molnár F, Watkinson DH (2001a) Fluid-inclusion data for vein-type Cu-Ni-PGE footwall ores, Sudbury Igneous Complex and their use in establishing an exploration model for hydrothermal PGE-enrichment around mafic-ultramafic intrusions. Exploration and Mining Geology 10:125-141

Molnár F, Watkinson DH, Jones PC (2001b) Multiple hydrothermal processes in footwall units of the North Range, Sudbury Igneous Complex, Canada, and implications for the genesis of vein-type Cu-Ni-PGE deposits. Economic Geology 96:1645-1670

Mulholland IR (1984) Malayaite and tin-bearing garnet from a skarn at Gumble, NSW, Australia. Mineralogical Magazine 48:27-30

Müller A, Kearsley A, Spratt J, Seltmann R (2012) Petrogenetic implications of magmatic garnet in granitic pegmatites from southern Norway. The Canadian Mineralogist 50:1095-1115

Naldrett AJ, Asif M, Schandl E, Searcy T (1999) Platinum-group elements in the Sudbury ores: Significance with respect to the origin of different ore zones and to the exploration for footwall orebodies. Economic Geology 94:185-210

Nelles EW, Lesher CM, Lafrance B (2010) Mineralogy and textures of Cu–PPGE–Au-rich mineralization in the Morrison (Levack footwall) Deposit, Sudbury, Ontario (abs). SEG 2010 Conference, 2010, Keystone, USA

O'Neil JR, Clayton RN, Mayeda TK (1969) Oxygen isotope fractionation in divalent metal carbonates. Journal of Chemical Physics 51:5547–5558

Page FZ, Kita NT, Valley JW (2010) Ion microprobe analysis of oxygen isotopes in garnets of complex chemistry. Chemical Geology 270:9-19

Péntek A, Molnár F, Watkinson DH, Jones PC (2008) Footwall-type Cu-Ni-PGE mineralization in the Broken Hammer area, Wisner township, North Range, Sudbury structure. Economic Geology 103:1005-1028

Péntek A, Molnár F, Watkinson DH, Jones PC, Mogessie A (2009) Partial melting and melt segregation in footwall units within the contact aureole of the Sudbury Igneous Complex (North and East Ranges, Sudbury structure), with implications for their relationship to footwall Cu-Ni-PGE mineralization. International Geology Review 51:1938-2839

Péntek A, Molnár F, Tuba G, Watkinson DH, Jones PC (2013) The significance of partial melting processes in hydrothermal low sulfide Cu-Ni-PGE mineralization within the footwall of the Sudbury Igneous Complex, Ontario, Canada. Economic Geology 108:59-78

Riciputi LR, Paterson BA, Ripperdan RL (1998) Measurement of light stable isotope ratios by SIMS: Matrix effects for oxygen, carbon, and sulfur isotopes in minerals. International Journal of Mass Spectrometry 178:81-112

Rudnick RL, Gao S (2003) Composition of the continental crust. In: Rudnick RL (ed) The Crust. In: Holland HD, Turekian KK (eds) Treatise on Geochemistry. Elsevier, Oxford 3:1-64

Smith MP, Henderson P, Jeffries TER, Long J, Williams CT (2004) The rare earth elements and uranium in garnets from the Beinn an Dubhaich aureole, Skye, Scotland, UK: Constraints on processes in a dynamic hydrothermal system. Journal of Petrology 45:457-484

Spry PG, Heimann A, Messerly JD, Houk RS (2007) Discrimination of metamorphic and metasomatic processes at the Broken Hill Pb-Zn-Ag Deposit, Australia:

Rare earth element signatures of garnet-rich rocks. Economic Geology 102:471-494

Tuba G, Molnár F, Watkinson DH, Jones PC, Mogessie A (2010) Hydrothermal vein and alteration assemblages associated with low-sulfide footwall Cu-Ni-PGE mineralization and regional hydrothermal processes, North and East Ranges, Sudbury structure, Canada. SEG Special Publication 15:573-598

Tuba G, Molnár F, Ames DE, Péntek A, Watkinson DH, Jones PC (2013) Multi-stage hydrothermal processes involved in "low-sulfide" Cu(-Ni)-PGE mineralization in the footwall of the Sudbury Igneous Complex (Canada): Amy Lake PGE zone, East Range. Mineralium Deposita DOI 10.1007/s00126-013-0468-1

Valley JW, Kitchen N, Kohn MJ, Niendorf CR, Spicuzza MJ (1995) UWG-2, a garnet standard for oxygen isotope ratios: Strategies for high precision and accuracy with laser heating. Geochimica et Cosmochimica Acta 59:5223-5231

White CJ (2012) Low-sulfide PGE-Cu-Ni mineralization from five prospects within the footwall of the Sudbury Igneous Complex, Ontario, Canada. Unpublished Ph.D. thesis, University of Toronto, Toronto, Ontario, Canada, 318 p.

Wilkinson JJ (2001) Fluid inclusions in hydrothermal ore deposits. Lithos 55:229-272

Zhai DG, Liu JJ, Zhang HY, Wang JP, Su L, Yang XA, Wu SH (2014) Origin of oscillatory zoned garnets from the Xieertala Fe-Zn skarn deposit, northern China: In situ LA-ICP-MS evidence. Lithos 190-191:279-291

Chapter 4: Future work

4.0 Suggestions for future work

The conclusions of this thesis can spark focused mineralogical and geochemical studies that would easily confirm or refute their validity. Decoupling "high sulfide" and "low sulfide" mineralization (as concluded in this thesis) into separate geochemical systems is not a practice that all Sudbury researchers have undertaken in their respective studies on these two mineralizing systems. The following is a list of potential studies that would lend stronger evidence as to whether these mineralization styles are genetically-related or independent of one another:

- Providing better constraints on fO_2 variation along sharp-walled veins. This can be achieved in many ways. Documenting the extent of Se-replacement for S in sulfides (especially galena) with position in the footwall would certainly be beneficial. Mineralogical mapping of minerals that exhibit Se solid solution (e.g., geffoyite, kurilite, etc.) along the veins and documenting the presence of primary selenides (e.g., naumannite, clausthalite, etc.) would go hand-in-hand with the galena study. Overall increases in these factors with progressive traverses deeper into the footwall would suggest progressive oxidation of the Cu-rich residue responsible for sharp-walled vein formation. No selenides were observed in low sulfide mineralization in this study.

- More information on fO_2 variation along sharp-walled veins would be gleaned from variation in the concentration and chemistry of primary oxides

with position in the footwall. Magnetite and cassiterite are the most abundant candidates but other oxides exist as primary inclusions in the veins as well (e.g., bismite, paratellurite, zincite, etc.).

- Focused mineralogical work from "hybrid" footwall environments. Can minerals from the sulfbismuthite group be shown to only occur as primary inclusions in the low sulfide segments of the hybrid sample? These minerals are associated with reducing environments and were only shown to exist as primary inclusions in low sulfide samples in this study (with only one exception where parkerite was intergrown with an end member PGM in a vein sample – xenocryst from previously formed low sulfide assemblage?).

- Since the source of metals from low sulfide mineralization is uncertain, a Lu-Hf age from coeval hydrothermal garnet would confirm that low sulfide mineralization was in fact SIC-related.

- Sulfur isotope studies on low sulfide mineralization would be beneficial. While the general consensus is that the fluids which formed low sulfide mineralization were sourced from a magmatic body related to the SIC, other possibilities exist. The meteorite impact which created the SIC system could have tapped a deeper level in the earth that was characterized by heavy oxygen isotope signatures.

- Epidote comprises part of the low sulfide alteration assemblage for each respective subgroup (calcite-free, calcite-bearing, garnet-bearing). Rb-Sr studies of epidote from each subgroup could help confirm whether groundwater dilution is raising calcium activities and producing the

increasingly Ca-rich alteration assemblages associated with low sulfide mineralization. Do garnet-bearing assemblages have $^{87}Sr/^{86}Sr$ ratios indicative of the most dilution by meteoric water? Do calcite-free assemblages have $^{87}Sr/^{86}Sr$ ratios indicative of the least dilution?

This list is certainly not exhaustive and many completely different studies would address the issue at hand. However, the primary conclusion and take-away message from this research is that high sulfide and low sulfide mineralization should be taken as entirely independent mineralizing systems (unless sufficient evidence suggests otherwise) and the evidence derived from this thesis entirely supports this message.